

## INFORMATION TO USERS

This manuscript has been reproduced from the microfilm master. UMI films the text directly from the original or copy submitted. Thus, some thesis and dissertation copies are in typewriter face, while others may be from any type of computer printer.

**The quality of this reproduction is dependent upon the quality of the copy submitted.** Broken or indistinct print, colored or poor quality illustrations and photographs, print bleedthrough, substandard margins, and improper alignment can adversely affect reproduction.

In the unlikely event that the author did not send UMI a complete manuscript and there are missing pages, these will be noted. Also, if unauthorized copyright material had to be removed, a note will indicate the deletion.

Oversize materials (e.g., maps, drawings, charts) are reproduced by sectioning the original, beginning at the upper left-hand corner and continuing from left to right in equal sections with small overlaps. Each original is also photographed in one exposure and is included in reduced form at the back of the book.

Photographs included in the original manuscript have been reproduced xerographically in this copy. Higher quality 6" x 9" black and white photographic prints are available for any photographs or illustrations appearing in this copy for an additional charge. Contact UMI directly to order.

# UMI

A Bell & Howell Information Company  
300 North Zeeb Road, Ann Arbor MI 48106-1346 USA  
313/761-4700 800/521-0600



**THE UNIVERSITY OF OKLAHOMA**

**GRADUATE COLLEGE**

**MODELING OF THE AEROSOL-CLOUD  
INTERACTIONS IN  
MARINE STRATOCUMULUS**

**A Dissertation**

**SUBMITTED TO THE GRADUATE FACULTY**

**in partial fulfillment of the requirements for the**

**degree of**

**Doctor of Philosophy**

By

QINGFU LIU

Norman, Oklahoma

1997

**UMI Number: 9812256**

---

**UMI Microform 9812256  
Copyright 1998, by UMI Company. All rights reserved.**

**This microform edition is protected against unauthorized  
copying under Title 17, United States Code.**

---

**UMI**  
300 North Zeeb Road  
Ann Arbor, MI 48103

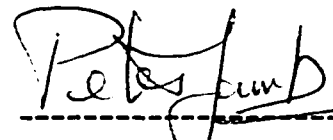
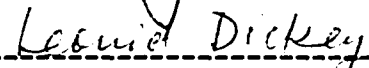
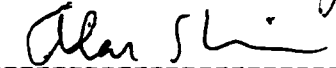
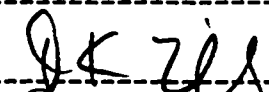
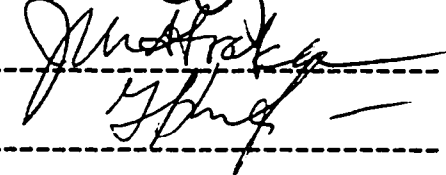
© Copyright by Qingfu Liu 1997

All Rights Reserved

MODELING OF THE AEROSOL-CLOUD  
INTERACTIONS IN  
MARINE STRATOCUMULUS

A Dissertation APPROVED FOR  
THE SCHOOL OF METEOROLOGY

BY

  
-----  
  
-----  
  
-----  
  
-----  
  
-----

## ACKNOWLEDGMENTS

First of all, I would like to thank Dr. Yefim L. Kogan, my research advisor, for his insightful and patient guidance in the last several years and for reviewing and editing this thesis. Without his help, this research would not have been possible. I would also like to thank Dr. Douglas K. Lilly, my former major advisor, who brought me back to Norman. Without him, this research would also not have been possible. Thanks also go to my other committee members, Drs. Peter Lamb, Jerry Straka, Alan Shapiro and Leonid Dickey for their encouragement and time.

Discussions with professor Chongjian Qiu have been very helpful at the early stage of my research. I would also like to thank Dr. Vince Wong for reading and editing part of my dissertation. Thanks also go to Drs. Zhi Wang, Marat Khairoutdinov, Jidong Gao and many others for their friendship and help during my years at OU as a graduate student.

Finally, I would like to express my deep appreciation to my beloved wife Min Zou for being very patient and supportive and taking good care of my two young daughters Sarah and Grace in the years of study.

This research was supported by the DOE Atmospheric Radiation Measurement (ARM) Project 144880-A91, the DOD-ONR Grants N00014-96-1-1112, N00014-96-0687, the NOAA's Climate and Global Change Program Grants NA37RJ0203, NA67RJ0150, and the NSF Grant ATM88-09862 to CAPS. Computations were performed on the DEC Alfa workstation funded by the NASA Earth Science and Application Division, Radiation Dynamic and Hydrology Branch, through Task 460-23-54-20, and CIMMS Hitachi supercomputer.

## TABLE OF CONTENTS

|   | <b>Page</b> |
|---|-------------|
| <b>Acknowledgments</b> -----  | iv          |
| <b>Table of contents</b> -----  | v           |
| <b>List of tables</b> -----   | vii         |
| <b>List of figures</b> -----  | viii        |
| <b>Abstract</b> -----   | xi          |
| <br><b>Chapter</b>  |             |
| <b>1. Introduction</b> -----  | 1           |
| 1.1 The climatic importance of direct and indirect effects of aerosols --   | 2           |
| 1.2 Review of Aerosol-Cloud Interactions -----  | 7           |
| 1.2.1 The effects of aerosols on cloud microphysics<br>and cloud radiative properties -----                                     | 7           |
| 1.2.2 Cloud processing of aerosols -----  | 11          |
| 1.3 My research objective -----   | 17          |
| <b>2. Description of the CIMMS LES model</b> -----  | 20          |
| 2.1 Dynamic framework -----   | 21          |
| 2.2 Microphysics and radiative process -----  | 24          |
| 2.3 Numerical scheme -----  | 27          |
| <b>3. Variational optimization method for the calculation of cloud<br/>drop growth in an Eulerian drop-size framework</b> ----- | 29          |
| 3.1 Introduction -----  | 29          |
| 3.2 Formulation of the method -----   | 31          |
| 3.3 Description of the Lagrangian air parcel model -----  | 36          |



|  |            |
|--|------------|
| 3.4 Verification of the method in a Lagrangian model -----   | 37         |
| 3.5 Modification of the VO method for precipitating clouds -----   | 42         |
| 3.6 Conclusions -----  | 50         |
| <b>4. A study of aerosol effects on cloud microphysics and cloud<br/>radiative properties through "ship track" simulations -----</b> | <b>53</b>  |
| 4.1 Introduction -----   | 53         |
| 4.2 Effects of the boundary layer structure on the ship<br>track formation -----   | 55         |
| 4.3 Microphysical and radiative properties of the ship track -----   | 76         |
| 4.4 Conclusions -----  | 92         |
| <b>5. Study of aerosol processing in stratocumulus clouds -----</b>  | <b>94</b>  |
| 5.1 Two parameter cloud drop spectrum model -----  | 95         |
| 5.2 Coalescence calculation and model accuracy test -----  | 96         |
| 5.3 3-D simulation experiment of aerosol processing -----  | 99         |
| 5.4 Conclusions -----  | 118        |
| <b>6. Summary and conclusions -----</b>  | <b>120</b> |
| <b>REFERENCES -----</b>  | <b>125</b> |
| <b>APPENDIX A -----</b>  | <b>132</b> |
| <b>APPENDIX B -----</b>  | <b>134</b> |

# LIST OF TABLES

| <b>Table</b>  | <b>Page</b> |
|---|-------------|
| 1.1 Global area-averaged cloud forcing by type of cloud ----- | 5           |
| 3.1 Classification of the cloud drop spectra -----            | 49          |
| 3.2 Averaged standard deviation -----                         | 50          |

## LIST OF FIGURES

| Figure  | Page |
|---|------|
| 1.1 The annual mean global energy balance<br>for the earth-atmosphere system -----  | 3    |
| 1.2 Diagram showing the five cloud types -----                                      | 4    |
| 1.3 Cloud albedo susceptibility as a function of drop concentration -----           | 10   |
| 1.4 Washout coefficient as a function of particle size -----                        | 14   |
| 3.1 Initial cloud drop spectrum -----   | 38   |
| 3.2 Results of the Lagrangian parcel model test 1 -----                             | 40   |
| 3.3 Results of the Lagrangian parcel model test 2 -----                             | 41   |
| 3.4 The conceptual model illustrating the decomposition procedure -----             | 44   |
| 3.5 Results of the Lagrangian parcel model test 3 -----                             | 45   |
| 3.6 Results of the Lagrangian parcel model test 4 -----                             | 47   |
| 3.7 Results of the Lagrangian parcel model test 3 -----                             | 48   |
| 4.1 Vertical profiles of the thermodynamic variables in A334 -----                  | 56   |
| 4.2 Vertical profiles of the thermodynamic variables in A348 -----                  | 57   |
| 4.3 Time evolution of horizontally averaged parameters<br>in simulation A334 -----  | 59   |
| 4.4 Time evolution of horizontally averaged parameters<br>in simulation A348 -----  | 60   |
| 4.5 Horizontal cross sections in simulation A348 -----                              | 63   |
| 4.6 Vertical cross sections in simulation A348 -----                                | 65   |
| 4.7 Time evolution of horizontally averaged parameters<br>in simulation A348B ----- | 69   |

|   |    |
|---|----|
| 4.8 Vertical cross section in simulation A348B -----  | 70 |
| 4.9 Time evolution of horizontally averaged parameters<br>in simulation A348N -----   | 72 |
| 4.10 Time evolution of horizontally averaged parameters<br>in simulation A348B1 -----   | 74 |
| 4.11 Total amount of the passive scalar accumulated above 0.5 km<br>for the simulations A348, A348B, A348N and A348B1 -----   | 75 |
| 4.12 Satellite image at 0000 UTC on June 9, 1994 -----  | 77 |
| 4.13 Time evolution of horizontally averaged parameters<br>in simulation A334-2D -----  | 78 |
| 4.14 Time evolution of the ship track width in A334 -----   | 80 |
| 4.15 Cloud drop concentration and vertical averaged parameters<br>of the cloud layer in simulation A334P -----  | 82 |
| 4.16 Cloud drop concentration, LWC and effective radius in simulation<br>A334P and its associated control run -----   | 83 |
| 4.17 Cloud drop concentration and vertical averaged parameters<br>of the cloud layer in simulation A334C -----  | 84 |
| 4.18 Cloud drop spectrum and vertical averaged parameters<br>in simulation A334C -----  | 86 |
| 4.19 Cloud drop concentration and vertical averaged parameters<br>of the cloud layer in simulation A334C -----  | 88 |
| 4.20 Cloud drop concentration, total LWC and 2D-C LWC<br>in simulation A348P -----  | 89 |
| 4.21 Vertically averaged cloud drops and the sum of CCN and<br>cloud drops, as well as the vertical integration of $w^2$ in<br>simulations of A334C and A334P ----- | 91 |

|  |       |     |
|--|-------|-----|
| 5.1 Initial 2-D cloud drop spectrum  | ----- | 98  |
| 5.2 2-D cloud drop spectrum after 2 hours coalescence simulation   | ----- | 100 |
| 5.3 Results of 2-D spectrum model tests  | ----- | 101 |
| 5.4 Horizontally averaged vertical profiles of the 3-D experiments   | ----- | 103 |
| 5.5 Time evolution of the CCN number loss  | ----- | 104 |
| 5.6 Activated CCN spectra at 5 hours and 8 hours   | ----- | 105 |
| 5.7 Evolution of the salt mass content   | ----- | 107 |
| 5.8 Accumulated CCN spectrum at the ocean surface at 5 and 8 hours   | ----- | 108 |
| 5.9 Horizontally averaged LWC distribution and mean drop<br>radius as functions of CCN size                        | ----- | 109 |
| 5.10 Horizontally averaged LWC distribution as functions of<br>cloud drop size                                     | ----- | 111 |
| 5.11 Activated CCN and interstitial aerosol distribution at 5 hours  | ----- | 112 |
| 5.12 The average aerosol spectra in the boundary layer at 5 and 8<br>hours if the cloud were completely evaporated | ----- | 113 |
| 5.13 Scattering coefficient of a single particle per unit volume<br>as a function of the particle diameter         | ----- | 115 |
| 5.14 Visibility increase due to cloud processing of aerosols   | ----- | 116 |
| 5.15 Total number of activated CCN as a function of supersaturation  | ----- | 117 |

## Abstract

This dissertation is primarily focus on the study of aerosol-cloud interactions. First, the CIMMS Large Eddy Simulation (LES) model is used to study the effects of aerosol on cloud microstructure and cloud radiative properties by modeling the ship track effects. Second, a new enhanced version of the CIMMS explicit microphysical model is developed. The model allows us to track aerosol particles during their interactions with cloud and is used to simulate cloud processing of aerosols. An important part of the research was the development of a new variational optimization (VO) method which significantly limits the artificial broadening of cloud drop spectrum in the condensation calculations. The method requires specification of only one variable in each bin size for condensation and evaporation calculations in an Eulerian drop-size framework. The results show that the variational method not only conserves the integral parameters of the spectrum, such as drop number, mean radius, liquid water content and the effective radius, but also provides very accurate calculation of the spectrum itself.

Using the CIMMS LES model with the VO method for condensation calculation, the aerosol effects on cloud microphysics and cloud radiative properties through the simulation of ship track formation have been studied . The CIMMS LES model has been run using both bulk and explicit microphysics to study ship track formation under various boundary layer conditions. Using a bulk thermodynamic formulation, I contrast the rates of effluent transport through a well-mixed boundary layer and

through a decoupled layer. I also simulate the effects of heat injected by the ship engine exhaust on the transport of ship effluents into the cloud layer, finding a significant effect. Using an explicit microphysical model, I carry out simulations in clean and relatively polluted air. I find that a ship track forms easily in a well-mixed convective boundary layer in an environment with low cloud condensation nuclei, but its formation may be suppressed by the stable transition layer in the decoupled case. I also find that a ship track survives longer in a clean boundary layer than in a polluted environment. In the clean environment, drizzle is clearly suppressed. In the relatively polluted environment, drizzle suppression is small, particularly in the decoupled boundary layer. The drop spectra inside the ship track are relatively narrow and are composed mostly of small drops, whereas the drop spectra outside the ship track show primarily bimodal distributions. The calculated albedo shows a substantial increase inside the ship track. The liquid water content inside the ship track may, however, be lower or higher than the outside, depending on specific characteristics of the boundary layer, such as mixed layer depth, stability of the transition layer, and the concentration of cloud condensation nuclei.

In order to study the cloud processing of aerosols, a two-parameter drop spectrum that depends on both the drop mass and the solute mass has been introduced into the CIMMS LES model. The aerosol processing due to condensation, cloud droplet collision-coalescence and drizzle fallout have been studied through model simulation. The results show that continental (polluted) air can be modified to marine air within approximately 2 days through reduction of the aerosol number concentration. Coalescence is responsible for nearly all of the cloud condensation nuclei (CCN) number reduction. The coalescence process mostly affects the small and medium size CCN particles (from 0.05 to 0.8 micron) and results in a net reduction of the number of CCN particles which would activate at a given

supersaturation. The reduction of the CCN activation rate at a given supersaturation is most important to the cloud microstructure, drizzle formation and the cloud radiative properties. The removal of CCN mass of the fine size particles (from 0.05  $\mu\text{m}$  to 0.5  $\mu\text{m}$  in radius) contributes the most to the visibility increase. The visual range is increased by a factor of 4.3 in a six hour model simulation. Drizzle fallout removes negligible number of CCN particles, but substantially removes the aerosol mass. Large size CCN particles created by drop coalescence in addition to the existing large CCN particles are efficiently removed by drizzle fallout.



## Chapter

# 1

## Introduction

Atmospheric aerosols and marine stratocumulus clouds have been the focus of a significant interest in recent years, mainly due to the important role they play in the Earth's radiative energy balance. Atmospheric aerosols affect the earth's radiative balance both directly through the upward scatter of solar radiation and indirectly as cloud condensation nuclei (CCN). The global mean radiative forcing due to the direct effect of anthropogenic sulfate aerosol particles is comparable in magnitude (approximately  $-1.0$  to  $-2.0$   $\text{Wm}^{-2}$ ) but opposite in sign to the forcing due to anthropogenic  $\text{CO}_2$  and the other greenhouse gases (Charlson, et al. 1992, Penner et al. 1994). Clouds have a net cooling effect on Earth-Atmosphere system. On global average the net forcing is about  $20$   $\text{W m}^{-2}$ , and low level clouds (mainly marine stratiform clouds) contribute the most to this forcing. Those marine stratiform clouds

have a pronounced climate effect because of their large global area coverage, high reflectivity compared to the sea surface, and near-absence of greenhouse effects. It has been estimated that the global cooling that would result from a 4% increase in the area covered by marine stratocumulus would offset the expected warming from a doubling of atmospheric CO<sub>2</sub> concentrations (Randall et al. 1984).

In the following sections of this chapter, first, I briefly discuss the climatic importance of direct and indirect effects of aerosols, which explains why many researchers are interested in the study of aerosols and stratocumulus clouds. Second, I give a detailed review of the current understandings of aerosol-cloud-radiative interactions. Third, I discuss my research objective.

## **1.1 The climatic importance of direct and indirect effects of aerosols**

Together with the molecular scattering from gases, aerosols and clouds determine what fraction of the solar radiation incident at the top of the atmosphere reaches the Earth's surface, and what fraction of the longwave radiation from the Earth escapes to space. Fig. 1.1 shows the annual mean global energy balance for the earth-atmosphere system (Wallace and Hobbs, 1977). Of the 100 units of incident solar radiation (representing yearly average solar radiation flux  $345 \text{ W m}^{-2}$  on top of the atmosphere), 30 units are reflected back to space: 20 from clouds and aerosols, 6 from cloud-free air, and 4 from the Earth's surface. A total of 19 units are absorbed during passage through the atmosphere: 16 in cloud-free air and 3 in clouds. The cloud absorption of solar radiation may be lower according to the most recent data in the Atmospheric Radiation Measurement (ARM) Enhanced Shortwave Absorption Experiment (ARESE) (Minnis et. al., 1997). The remaining 51 units are absorbed at the earth's surface. The earth disposes of this energy by a combination of infrared

radiation and sensible and latent heat flux. Of the 70 units of outgoing infrared radiation from the earth-atmosphere system, 6 units from the Earth's surface, 38 units from cloud-free atmosphere, and 26 units from clouds.

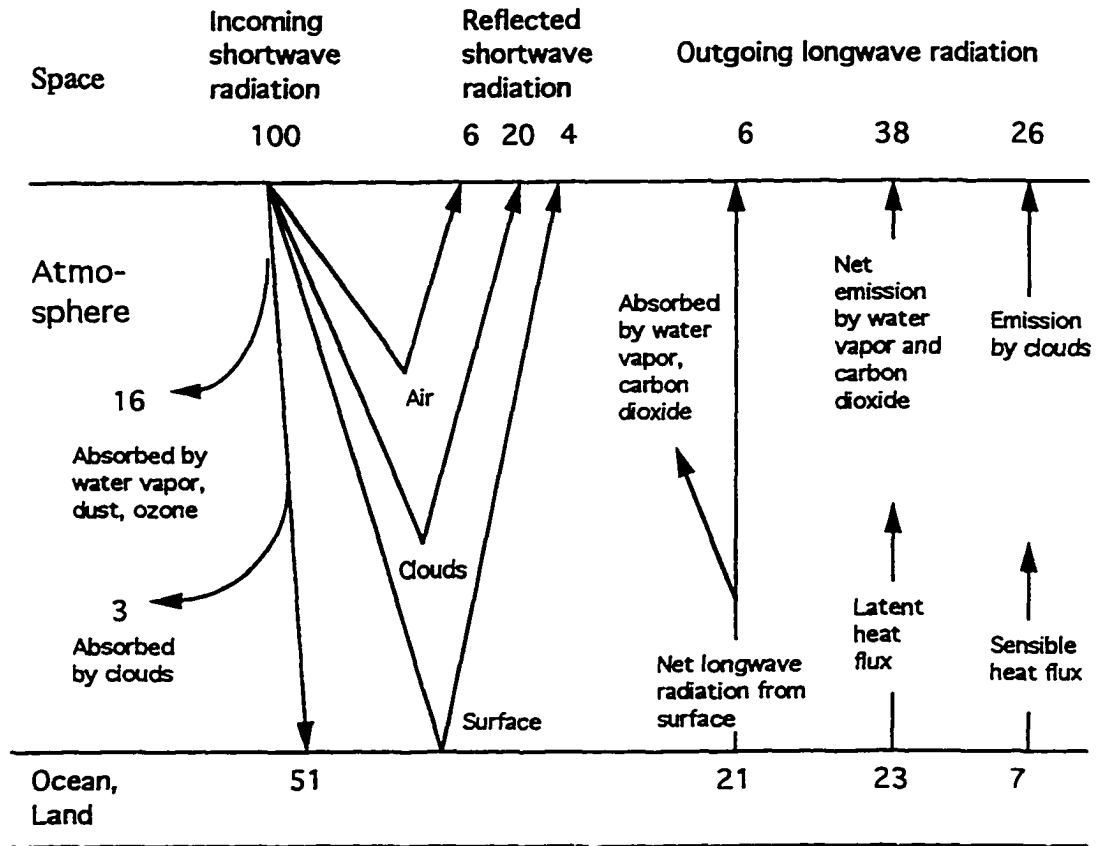


Figure 1.1. The annual mean global energy balance for the earth-atmosphere system (Data from Wallace and Hobbs, 1977)

Clouds have a net radiation cooling effect on earth-atmosphere system. Clouds reduce the global average absorbed solar radiation by about  $50 \text{ W m}^{-2}$ . The longwave cloud forcing (greenhouse effect) is about  $30 \text{ W m}^{-2}$ . Therefore the global average net cloud forcing is about  $20 \text{ W m}^{-2}$ . Hartmann et al. (1992) used ERBE (Earth Radiation Budget Experiment) data in conjunction with cloud descriptions from ISCCP (International Satellite Cloud Climatology Project) data to estimate the

importance of various cloud types in the energy balance of the earth-atmosphere system. They divided the clouds into five cloud types based on the cloud top pressure and the visible optical depth (Fig. 1.2). Table 1.1 is the summary of their results ( $C_i$  is the fractional coverage by one of the five cloud types, OLR represents the outgoing longwave radiation). Several features we would like to emphasize here:

a) low clouds have the largest area coverage and the largest net radiation forcing.

b) high-thin and mid-thin clouds have a net positive effect on earth's radiation budget.

c) High-thick clouds have the largest "greenhouse" effects despite their small fractional coverage. However, the large OLR forcing of these clouds is offset by the very powerful albedo forcing of these clouds, so that their contribution to the net cloud forcing is only a little more than a third of that for low clouds.

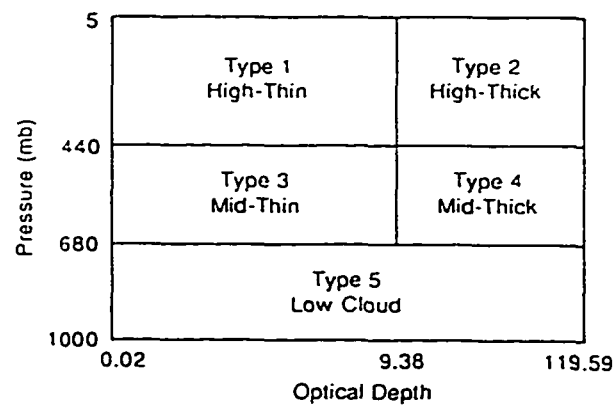


Figure 1.2. Diagram showing the five cloud types. The clouds are divided into high, middle, and low, according to the pressure at cloud top, and into thin ( $\tau < 9.38$ ) and thick ( $\tau \geq 9.38$ ) according to the visible optical depth  $\tau$ . (From Hartmann et al., 1992)

Table 1.1

Global Area-Averaged Cloud Forcing by Type of Cloud

| Season:<br>Parameters <sup>a</sup> | Type 1<br>high, thin |      | Type 2<br>high, thick |       | Type 3<br>mid, thin |      | Type 4<br>mid, thick |       | Type 5<br>low |       | Sum   |
|------------------------------------|----------------------|------|-----------------------|-------|---------------------|------|----------------------|-------|---------------|-------|-------|
|                                    | JJA                  | DJF  | JJA                   | DJF   | JJA                 | DJF  | JJA                  | DJF   | JJA           | DJF   | Ave.  |
|                                    | $C_i$                | 10.2 | 10.0                  | 8.5   | 8.8                 | 10.7 | 10.7                 | 6.5   | 8.2           | 27.2  | 25.9  |
| OLR                                | 6.5                  | 6.3  | 8.4                   | 8.8   | 4.8                 | 4.9  | 2.4                  | 2.4   | 3.5           | 3.5   | 25.8  |
| Albedo                             | 1.2                  | 1.1  | 4.1                   | 4.2   | 1.1                 | 1.0  | 2.7                  | 3.0   | 5.8           | 5.6   | 14.9  |
| Net                                | 2.4                  | 2.3  | -6.4                  | -7.5  | 1.4                 | 0.8  | -6.6                 | -8.5  | -15.1         | -18.2 | -27.6 |
| $\Delta$ OLR                       | 63.7                 | 63.0 | 98.8                  | 100.0 | 44.9                | 45.8 | 36.9                 | 29.3  | 12.9          | 13.5  | 40.8  |
| $\Delta$ Albedo                    | 11.8                 | 11.0 | 48.2                  | 47.7  | 10.3                | 9.3  | 41.5                 | 36.6  | 21.3          | 21.6  | 23.5  |
| $\Delta$ Net                       | 23.5                 | 23.0 | -75.3                 | -85.2 | 13.1                | 7.5  | -102.                | -104. | -55.5         | -70.3 | -43.6 |

<sup>a</sup>OLR and net radiation are given in  $W m^{-2}$  and albedo and cloud fractional coverage ( $C_i$ ) are given in percent. OLR, Albedo, and Net indicate the global-average forcing of the radiation balance by the cloud type of interest.  $\Delta$ OLR,  $\Delta$ Albedo, and  $\Delta$ Net indicate the average contrast between the cloud type and a clear scene and are obtained by dividing the global average cloud forcing by the global average cloud amount. The last column is the sum over all cloud types and the average of the JJA and DJF season. The regions poleward of about  $60^\circ$  in the winter hemisphere are not included in the area average.

The low clouds are predominately marine stratus and stratocumulus clouds. These clouds have a relatively high albedo compared to the sea surface, and near-absence of greenhouse effects. They are observed to occur in very persistent sheets covering large areas of the eastern parts of subtropical ocean basins, where the boundary layer is capped by a strong inversion produced by large scale subsidence. The vertical mixing that supplies moisture to these clouds is primarily driven by cloud top radiative cooling. It has been estimated that the radiative cooling from a 4% increase in the area covered by marine stratocumulus cloud would offset the expected warming from a doubling of CO<sub>2</sub> concentration (Randall et al., 1984).

The direct shortwave radiation forcing of aerosols is relatively small ( $\sim 7 \text{ W m}^{-2}$ ), and anthropogenic sulfate aerosol imposes a major perturbation to this forcing. It is estimated that current climate forcing due to anthropogenic sulfate is  $\sim 1.0$  to  $2.0 \text{ W m}^{-2}$ . This shortwave forcing is roughly equal to a 1-2% change in the area of cloud coverage. However, it is comparable in magnitude but opposite in sign to the positive longwave forcing ( $2.5 \text{ W m}^{-2}$ ) of increased greenhouse gas emissions since the pre-industrial era (Charlson et al., 1992; Harshvardhan, 1993; Penner et al., 1994). Thus, the aerosol forcing is likely to offset the global greenhouse warming to a substantial degree. Compared to greenhouse gases, aerosol particles are relatively short-lived in the atmosphere, resulting in spatial and temporal nonuniformity. Therefore, differences in geographical and seasonal distributions of these forcing preclude any simple compensation. Due to the large uncertainties in the magnitude and geographical distribution of aerosol forcing, the influence of anthropogenic aerosols on climate is still under intensive investigation.

In spite of their climatic significance, aerosol particles and clouds, particularly low level clouds, are poorly treated in climate models, mainly due to the insufficient

knowledge of the processes that are responsible for their spatial and temporal variability. Consequently, model results show a pronounced sensitivity to the way clouds are treated in the models (Sundqvist, 1993). The most recent IPCC report (1996) again emphasizes that clouds are one of the largest uncertainties in the radiation balance of the Earth's atmosphere and their description needs significant improvement for climate change prediction.

## **1.2 Review of Aerosol-Cloud Interactions**

Atmospheric aerosols have a significant influence on cloud microphysical structure and their radiative properties. Twomey (1974) pointed out that cloud condensation nuclei (CCN) can affect cloud albedo, while Albrecht (1989) suggested that they can also regulate the lifetime of a cloud.

Not only are the stratocumulus cloud layers affected by the ambient aerosols, but, in turn, they can also substantially affect the ambient aerosol distributions. The scavenging of aerosol particles by clouds and their removal from the atmosphere by precipitation are important sinks for atmospheric aerosols. In the following subsections I will review in detail the current understandings of the aerosol-cloud interactions.

### **1.2.1 The effects of aerosols on cloud microphysics and cloud radiative properties**

Aerosols have an significant influence on cloud microphysical processes, drizzle formation and cloud radiative properties. Variations in CCN concentrations can affect cloud lifetime and its liquid water content (LWC). Albrecht (1989) argued that increased CCN concentrations, which decrease cloud drop sizes and inhibit precipitation development, can increase the cloud optical depth (thus increase cloud

albedo) and the fractional coverage of marine stratiform clouds because drizzle can regulate the LWC and the lifetime of clouds. He showed that the LWC of marine stratocumulus clouds in a relatively clear environment were substantially less than adiabatic values, while similarly appearing clouds that developed in a relatively polluted air had, in general, LWC close to adiabatic values. He attributed this difference to less cloud water depletion by drizzle in clouds with higher droplet count.

Baker and Charlson (1990) suggested that marine stratiform cloud layers are bistable with respect to CCN counts. In their model, they identified two stable states:  $\sim 10 \text{ cm}^{-3}$  for very clean marine air and  $\sim 1000 \text{ cm}^{-3}$  for high CCN concentration. However, Ackerman et al. (1992) using a more sophisticated model found that the marine atmosphere does not exhibit such an instability. They attributed the instability postulated by Baker and Charlson to their oversimplified treatment of cloud microphysical processes, particularly the production of drizzle. The model of Ackerman et al. produced a smooth transition between the low and high particle concentration states predicted by Baker and Charlson. At a relatively low CCN count clouds, Ackerman et al. (1993) found that clouds themselves may reduce particle concentrations to such an extent that the stratocumulus clouds dissipate and the boundary layer collapses.

The reflectivity of the marine stratiform clouds are very sensitive to their microphysical structure. The concentration and size distribution of cloud drops strongly depend on the aerosol spectrum. Twomey (1974) suggested that increased numbers of CCN can enhance cloud albedo because they increase the droplet surface area for a fixed mass of cloud water. The cloud albedo susceptibility  $dA/dN$ , where  $A$  is cloud albedo and  $N$  is drop concentration, gives the indirect radiative forcing of



aerosols. Based on a radiative model, Twomey (1991) predicted susceptibility to be an inverse function of drop concentration. Kogan et al. (1996) evaluated the cloud albedo susceptibility based on the CIMMS large eddy simulation (LES) model. Fig. 1.3 shows the susceptibility  $dA/dN$  derived from CIMMS LES model data together with the susceptibility estimated from aircraft observations (Taylor and McHaffe, 1994). The model results and observations agree rather well and demonstrate that low droplet count clouds are much more susceptible to changes in drop concentration than those with high drop counts. They give a curve fit as  $dA/dN=0.044 \times N^{-0.86}$ .

One of the most convincing pieces of evidence for the aerosol indirect effect is the appearance of the "ship tracks" in satellite images, which are observed as visually thickened and brightened parts of otherwise translucent cloud layers (Radke et al., 1988). "Ship tracks" may last for hundreds of kilometers and many hours. As suggested by Fig. 1.3 the ship tracks preferably form in a relatively clear environment where cloud albedo susceptibility is high. Observations (e.g. King et al. 1993; Johnson et al. 1995) show that aerosols, as well as cloud drop concentration are significantly increased inside the ship tracks. The effective radius, as well as drizzle production are considerably reduced. The ship tracks are generally believed to be the result of a large increase in CCN concentration in a region relatively devoid of them, thereby producing a more reflective and perhaps more durable cloud of many small droplets. The relationship between the concentration of cloud condensation nuclei and brightness is apparently nonlinear, as there is some evidence that intersecting condensation trails are no brighter than either trail alone (Porch et al., 1989).

Even though the potential effects of aerosol on cloud structures and radiative properties are well demonstrated by "ship tracks" in clouds, the regional and global

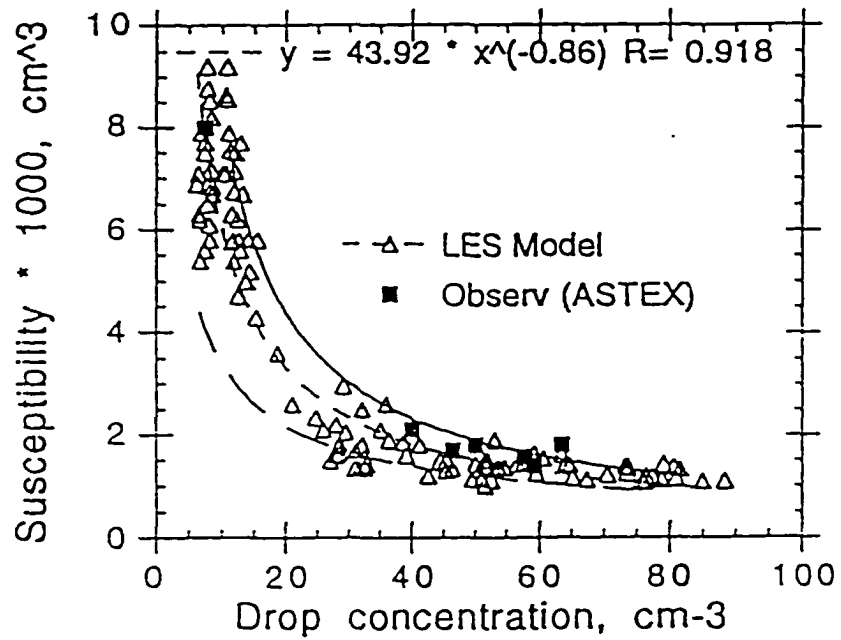


Figure 1.3. Cloud albedo susceptibility as a function of drop concentration. Triangles show the data obtained from the CIMMS LES cloud model, squares represents estimates from the ASTEX field observations. (Courtesy of Z. Kogan)

effects of aerosol on cloud radiative properties remain uncertain. Both observational and theoretical studies are needed to establish a broad data base and a firm understanding of the relevant physical and chemical processes, so that the complicated aerosol-cloud interactions may be parameterized with a good accuracy and can be easily incorporated into local, regional and global numerical models.

### **1.2.2 Cloud processing of aerosols**

The scavenging of aerosols by clouds and their removal from the atmosphere by precipitation are important sinks for atmosphere aerosols. It is estimated that, on the global scale, precipitation removes about 80% of the mass of aerosols from the atmosphere and gravitational settling (dry fallout) account for the rest (Wallace and Hobbs, 1977). Before aerosols are removed by precipitation, their parameters are substantially modified due to cloud processing. According to Pruppacher and Klett (1978), the cloud material, on a global scale, goes through about ten condensation-evaporation cycles before cloud eventually precipitates. The effect of the repeated cycling of cloudy air is the decrease of small aerosol particles and the increase of aerosol mass at sizes larger than 0.1 micron. The cloud recycling also produces a minimum at a size determined by maximum supersaturation in cloud. The increased mass of larger particles is the result not only of coalescence of cloud drops, but also Brownian scavenging of interstitial aerosol, as well as gas-to-particle conversion inside cloud drops. Measurements made by Hoppel et al. (1986) following an air mass advecting from the east coast of the U.S. out over the Atlantic provide evidence that cloud processing of aerosol may be responsible for the frequently observed double peak aerosol size distributions.

In-cloud scavenging of aerosol particles is one of the major mechanisms for the removal of atmospheric aerosols. Particles with sizes in the accumulation-mode

range (0.1-1  $\mu\text{m}$  radius) and larger are nucleated and become CCN under relatively small supersaturations (around 0.1%). Aerosols ingested into a cloud that do not serve as CCN will form cloud interstitial aerosol (CIA). Both CCN and CIA should change as cloud ages. The CIA should slowly diminish in number due to coagulation with cloud particles. Numerical simulations of convective clouds over the Atlantic Ocean by Flossman and Pruppacher (1988) and Flossman (1991) showed that in-cloud scavenging of aerosol was mainly controlled by nucleation scavenging. Flossman (1991) estimated that about 90% of the total aerosol mass is scavenged by nucleation. The Brownian motion and impaction remove very little aerosol mass inside the cloud, however, it may significantly affect the number concentration of the interstitial aerosols.

Cloud processing of aerosols has been studied by Hudson and Frisbie (1991) and Hudson (1993) using extensive airborne measurements of CCN spectra and concentrations of total particles during FIRE and Hawaiian Rainband Project (HaRP) experiments. The FIRE observations carried out over the 4-day period showed the decrease in the boundary layer aerosol concentration consistent with the in-cloud scavenging process. Hudson and Frisbie (1991) emphasize the importance of the "coalescence scavenging". It reduces the CCN concentration according to the number of cloud droplet captures, as well as transforms the CCN size distribution. The more active nuclei (corresponding to lower critical supersaturations) are not only preferentially used to form cloud droplets, but also increase in size due to the recycling following coalescence and evaporation of cloud droplets. The efficiency of the in-cloud scavenging processes can be estimated from the measured reduction of CCN concentration in the boundary layer below the inversion, and by comparing the CCN activation spectra in a cloud-free air with those in the air within and around the clouds. Observations by Hudson (1993) confirm that concentrations of CCN are

often lower within the boundary layer and they are also composed of larger particles with lower median critical supersaturation. Under conditions with few, or without clouds, the spectra below and above the temperature inversion are similar.

The wet removal of aerosol particles is important below the cloud base where they are captured by falling precipitation. Precipitation can remove the aerosol through gravitational coagulation, phoretic effects, and Brownian motion (see, e.g., Pruppacher and Klett, 1978). The relative role of these processes strongly depends on the aerosol particle size. The scavenging collection efficiency due to coagulation with rain particles is particularly efficient in the coarse (giant) aerosol size range, and the collision efficiencies decrease rather sharply with the decreasing size of the aerosol particle. The Brownian and phoretic forces, however, dominate for small particles. Theoretical and numerical modeling studies predict a minimum in the scavenging collection efficiency near the 0.5 micron aerosol radius. Greenfield (1957) first considered Brownian motion, turbulent diffusion and inertial impaction. He found that overall scavenging coefficient exhibited a strong broad minimum for aerosol particles between about 0.1 and 1.0  $\mu\text{m}$  radius. In the literature this minimum is therefore often referred to as the "Greenfield Gap". It is the result of Brownian diffusion dominating particle capture for aerosols with radius less than 0.1  $\mu\text{m}$ , and of inertial impaction dominating capture for aerosols with radius larger than 1.0  $\mu\text{m}$ . Slinn and Hales (1971), who included contributions from Brownian diffusion, inertial capture, as well as phoretic effects, have obtained similar results. However, they show that the scavenging effects due to phoretic processes tend to fill in the gap quite significantly even though the gap remains distinct (Fig. 1.4). It has been pointed out by McDonald (1964) that the atmosphere does provide a mechanism to bridge the "Greenfield Gap" in that the aerosol particles of radii between 0.1  $\mu\text{m}$  and 1.0  $\mu\text{m}$  most readily serve as CCN and IN (ice nuclei). As such they may be

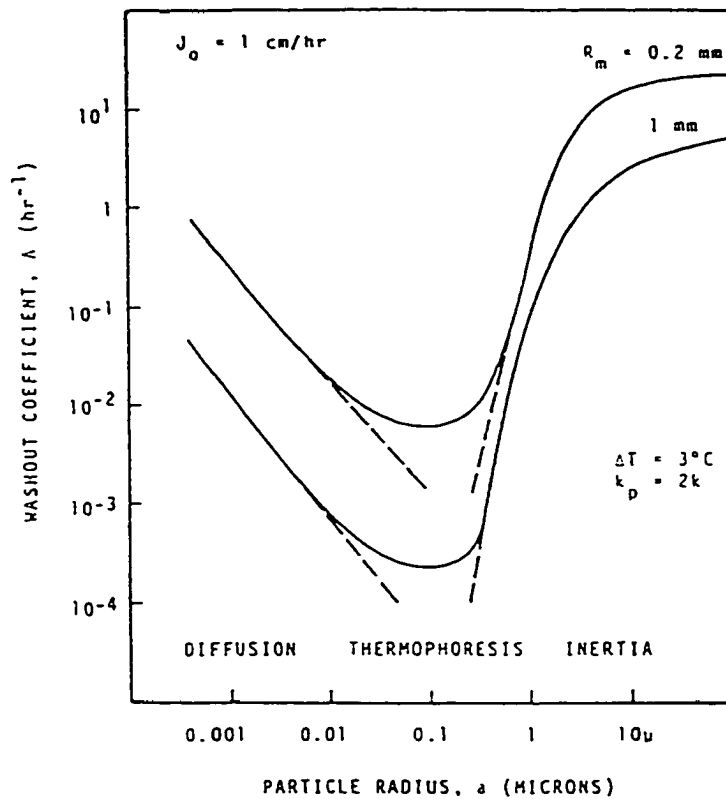


Figure 1.4. Washout coefficient as a function of particle size illustrating the regimes of the various scavenging mechanisms. (From Slinn and Hales, 1971).

removed from the atmosphere if cloud formation is followed by precipitation. It has to be noted that, although the effect of impaction scavenging within the cloud is quite negligible compared to nucleation scavenging (Flossman et al, 1985; Flossman and Pruppacher, 1988), its role in the sub-cloud scavenging is much more pronounced. Finally, it is worth noting that most of the modeling studies on the relative role of various cloud scavenging processes have been performed using models with rather simplified dynamics. Flossman et al (1985) emphasize the limitations and shortcomings of the "air-parcel-models" and the importance of coupling the scavenging model with a realistic dynamics model.

In addition to modifying existing aerosols, some recent research indicates that clouds can be involved in nucleation of new aerosols. Radke and Hobbs (1969), Saxena et al (1970), Hegg et al (1991) observed that, at a given supersaturation, CCN processed by clouds often have higher concentrations than those in the ambient air. Hegg et al. (1990) and Radke and Hobbs (1991) also presented data that is strongly suggestive of new aerosol formation in the vicinity of, or within, clouds. This aerosol production was attributed to the homogeneous bimolecular nucleation of sulfuric acid droplets from H<sub>2</sub>O-H<sub>2</sub>SO<sub>4</sub> vapor system. This theory is similar to that for the homogeneous nucleation of water droplets from water vapor, except that two molecules are involved in the condensation (sulfuric acid and water molecules). The theory allows for competition between new aerosol formation and condensation onto existing aerosol. Under polluted conditions, where the production of H<sub>2</sub>SO<sub>4</sub> vapor is large, there is generally a great deal of preexisting aerosol surface on which the vapor can condense. For cleaner conditions, where the surface area of the existing aerosol is less, precursor gas concentrations (SO<sub>2</sub>) may be too low for sufficiently rapid production of the acid vapor to achieve the supersaturations necessary for new aerosol production. Thus, the nucleation of new aerosol may occur only under rather

special atmospheric conditions, in which the surface area of existing aerosol is low, and SO<sub>2</sub> concentrations are moderate. As discussed by Hegg (1990), the new particles produced by homogeneous nucleation are quite small, and the time for growth of such particles to the CCN size of about 0.04 micron by means of condensation of acid vapor can be as large as 3-4 days. As the critical supersaturations needed for activation of particles in the nuclei-mode range are quite large, Hegg concludes that such particles have to be first processed by cumuliiform clouds where they can grow to sizes large enough to serve as CCN at much lower supersaturations typical for marine stratiform clouds.

Heterogeneous chemical reactions in clouds is another important mechanism of aerosol production in the atmosphere. Radke and Hobbs (1969) observed that the enhancement in CCN activity due to the oxidation of SO<sub>2</sub> leading to sulfate formation in cloud droplets. After cloud droplet evaporates it leaves behind a residue formed from the material of the original CCN and material formed as a result of aqueous chemical reactions. Thus, the gas-to-particles conversion mechanism changes the aerosol size distribution and increases the mass of atmospheric aerosol. It, however, does not affect the number of aerosol particles, as, according to current understanding, the role of aerosol splintering during cloud droplet evaporation is quite insignificant. Kreidenweis et al. (1996) estimated that at low to moderate LWCs (< 0.2 g m<sup>-3</sup>), aqueous chemistry plays a dominate role in modifying the mean particle size, whereas the impact of collision-coalescence is comparable to, or even greater than, that of chemistry for cloud with LWC 0.5 g m<sup>-3</sup>. Chemical reactions may occur strongly at the early stages of cloud formation, until reagents are consumed, whereas the effectiveness of collision-coalescence is expected to increase with time as drop number concentrations are depleted.



The incorporation of trace gases and aerosols into cloud and precipitation particles also has important effects on chemical composition of clouds and precipitation. Hegg (1983) combined field measurements and model results to estimate the sulfate content of precipitation particles from warm convective clouds formed in a polluted air. He found that the contributions to sulfate content of the precipitation were ~25% from nucleation scavenging, ~30% from below-cloud impact scavenging, and ~45% from in-cloud chemical reactions. Due to the importance of acid precipitation to the environment, agriculture, transportation, construction etc, a lot of research has been done on this subject in recent years. It is beyond the scope of this paper to review those works.

### **1.3 My research objective**

My major objective is to study the aerosol-cloud interactions using the CIMMS LES model. Although the effects of aerosols on clouds are reasonably understood, many unanswered questions remain for the cloud processing of aerosols. My research is primarily focus on the following topics:

*1) improvement in the calculation of cloud drop growth by condensation/evaporation in an Eulerian drop-size framework.*

The existing methods for calculation of the cloud condensation/evaporation process in an Eulerian drop-size framework are very dispersive. The numerical dispersion, to a certain degree unavoidable in any Eulerian formulation, if excessive, can result in broadening of the cloud drop spectrum and acceleration of the collection process, thus leading to an earlier development of precipitation. In a similar manner, it may accelerate the evaporation of cloud drops in the descending branches of cloud circulation.

In the old version of the CIMMS LES model, I found the cloud drop spectrum is artificially broadened in the condensation procedure. To limit the numerical dispersion and to improve the accuracy of the condensation calculations, I set the goal to develop a variational optimization method that requires specification of only one variable in each bin size for condensation and evaporation calculations in an Eulerian drop-size framework. In Chapter 3, I will describe the derivation of the VO method and show that the variational method not only conserves the integral parameters of the spectrum, such as drop number, mean radius, liquid water content and the effective radius, but also provides very accurate calculation of the spectrum itself.

*2) Aerosol effects on cloud microstructure and cloud radiative properties through ship track simulation.*

The effects of aerosol on cloud microstructure and cloud radiative properties is studied through simulation of ship track. The study of the ship track formation consists of two parts: first I will evaluate the rate of early dispersion of a passive scalar from a surface source under two different stratocumulus layer conditions: one representing a well-mixed and the other decoupled boundary layer. I will also evaluate the buoyancy and stability effects on the ship track formation in the decoupled marine boundary layer. Second, I will use the explicit CIMMS LES model which includes the new variational optimization (VO) method to study the aerosol effects on cloud microstructure and cloud radiative properties. Specifically, I will contrast the cloud drop spectra, drizzle water path and cloud albedo inside and outside the ship track. The results are presented in Chapter 4.

*3) Cloud processing of aerosols due to condensation, coalescence, and drizzle fallout.*

The goal of this study is to evaluate the effects of cloud processing on the aerosol spectrum transformation and the consequent changes in microphysical and radiative properties such as the aerosol number and salt mass removal rates, CCN activation rate and atmospheric visibility. The understanding of the aerosol spectrum changes due to cloud processing is essential for the development of parameterization of the CCN budget in mesoscale models.

I have developed a new version of the CIMMS LES model that includes a two-parameter spectrum that depends on both the drop mass and the solute mass. Such formulation is now computationally feasible and is needed for an accurate treatment of the aerosol recycling process. The aerosol processing due to nucleation, cloud droplet collision-coalescence and drizzle scavenging will be studied in an eight hour long 3-D simulation experiment.

The organization of this thesis is as follows: Chapter 1 has reviewed the aerosol-cloud interactions. Chapter 2 describes the CIMMS LES model. The variational optimization method is presented in Chapter 3, followed by the simulations of the ship track in Chapter 4. Chapter 5 describes the two parameter spectrum model and the simulation results, and Chapter 6 gives the summary and major conclusions.

## **Chapter**

# **2**

## **Description of the CIMMS LES Model**

The CIMMS LES cloud model can be run using two different dynamic platforms. The original version of the model employed the spectral code of Moeng (1984) for calculation of the tendencies for momentum and thermodynamic variables. The spectral method allows the most accurate calculation of the momentum equations, however, the lack of positive definiteness makes it less fit for advection of microphysical variables. Therefore, the spectral method for the momentum equations was combined with the Smolarkiewicz and Grabowsky (1990) positive definite finite-difference scheme for calculation of the dynamical tendencies of microphysical variables. As constraints imposed by the continuity equation were satisfied using the

spectral formulation, the velocity field remained divergent in the finite-difference representation, resulting in errors in advection of the microphysical fields. The problem was solved in the new version of the model by employing the same finite-difference representation for all model variables (Khairoutdinov and Kogan, 1996).

## 2.1 Dynamic framework

The governing equations for the resolved-scale velocities can be written as,

$$\frac{\partial \bar{u}_i}{\partial t} = -\frac{\partial}{\partial x_j} (\bar{u}_i \bar{u}_j + \delta_{ij} C_p \theta_0 \overline{\pi^*} + \tau_{ij}) + \delta_{i3} g \frac{\overline{\theta_v^*}}{\theta_0} + \varepsilon_{ij3} f (\bar{u}_j - u_{gj}) \quad (2.1)$$

$$\frac{\partial \bar{u}_i}{\partial x_i} = 0 \quad (2.2)$$

where  $\bar{u}_i$  ( $i=1, 2, 3$ ) are the resolved-scale velocity components;  $\delta_{ij}$  is the Kronecker delta symbol;  $u_{gj}$  ( $j=1, 2$ ) is the geostrophic velocity components,  $\pi$  is the Exner function and is defined as  $\pi = (p/p_0)^{R/C_p}$ ;  $\tau_{ij}$  ( $i, j=1, 2, 3$ ) are the subgrid scale Reynolds stresses;  $f$  is the Coriolis parameter;  $\theta_v$  is the virtual potential temperature defined as  $\theta_v = \theta_l + (L/C_p)q_l$ ;  $g$  is the gravity acceleration,  $p_0$  and  $\theta_0$  are the reference pressure and virtual potential temperature, respectively. Variables with stars are deviations from their horizontal mean.

The thermodynamic state is described in terms of the liquid water static energy  $h_l = C_p T(1 + 0.61q_v - q_l) + gz - Lq_l$  and the total water mixing ratio  $q_t = q_v + q_l$ , where  $T$  is the absolute temperature,  $q_v$  is the water vapor mixing ratio,  $q_l$  is the liquid water content,  $C_p$  is the specific heat of the air at constant pressure and  $L$  is the latent heat of condensation. Both  $h_l$  and  $q_t$  are conserved following an air parcel in moist-adiabatic processes. The governing equations for the liquid water potential temperature  $\theta_l = h_l / C_p$  and the total water mixing ratio  $q_t$  are

$$\frac{\partial \bar{\theta}_l}{\partial t} = -\frac{\partial}{\partial x_j} (\bar{\theta}_l \bar{u}_j + \tau_{j\theta}) + \left(\frac{\partial \bar{\theta}_l}{\partial t}\right)_{rad} + \frac{L}{C_p} \frac{\partial Q_p}{\partial z} - w_s \frac{\partial \bar{\theta}_l}{\partial z} \quad (2.3)$$

$$\frac{\partial \bar{q}_t}{\partial t} = -\frac{\partial}{\partial x_j} (\bar{q}_t \bar{u}_j + \tau_{jq}) - \frac{\partial Q_p}{\partial z} - w_s \frac{\partial \bar{q}_t}{\partial z} \quad (2.4)$$

where  $Q_p$  is the precipitation flux;  $\tau_{j\theta}$  and  $\tau_{jq}$  are the subgrid scale (SGS) fluxes of  $\theta_l$  and  $q_t$ , respectively;  $w_s$  is the large scale vertical velocity. The second term on the right-hand side of (2.3) represents heating/cooling due to shortwave/longwave radiation. The terms with  $Q_p$  account for the vertical divergence of precipitation flux. The last term in (2.3) and (2.4) represents the effect of large scale vertical advection which is calculated as  $w_s = -div \cdot z$ , where  $div$  is a constant large scale divergence specified as an external parameter.

The Reynolds stresses and the SGS fluxes are assumed to be proportional to the local gradients of the resolved scale quantities (Lilly, 1962),

$$\tau_{ij} = \overline{u_i u_j} = -k_m \left( \frac{\partial \bar{u}_i}{\partial x_j} + \frac{\partial \bar{u}_j}{\partial x_i} \right) + \frac{2}{3} \delta_{ij} e \quad (2.5)$$

$$\tau_{\phi j} = \overline{u_j \phi} = -K_h \left( \frac{\partial \bar{\phi}}{\partial x_j} \right) \quad (2.6)$$

where  $\phi$  represents thermodynamic variables,  $e$  is the SGS turbulent kinetic energy (TKE) and is defined as  $e \equiv 0.5(\overline{u_i u_i} - \bar{u}_i \bar{u}_i)$ ,  $K_m$  and  $K_h$  are the eddy viscosity and eddy conductivity coefficients, respectively. The coefficients are determined by one and a half order SGS closure proposed by Lilly (1967) and further developed and applied in LES by Deardorff (1980). The closure is based on the prognostic equation for the SGS turbulent kinetic energy,

$$\frac{\partial e}{\partial t} = -\frac{\partial}{\partial x_j} (\bar{u}_j e) - \overline{u_i u_j} \frac{\partial \bar{u}_i}{\partial x_j} + \frac{g}{\theta_0} \overline{w \theta_v} - \frac{\partial}{\partial x_j} [\overline{u_j (e + p' / \rho_0)}] - \epsilon \quad (2.7)$$

where  $\varepsilon$  is the dissipation rate, and  $\overline{w\theta'_v} = A\overline{w\theta'_t} + B\overline{\theta w'_t}$ . A and B slightly depends on temperature and total water content (Deardorff, 1980). The subgrid fluxes in the last two terms of Eq. (7) were parameterized as,

$$\overline{u'_j(e' + p' / \rho_0)} = -2k_m \frac{\partial \bar{e}}{\partial x_j}$$

$$\varepsilon = C_\varepsilon e^{3/2} / l$$

Where  $l$  is the sub-grid length scale,  $C_\varepsilon$  is a non-dimensional constant.

The coefficients  $K_m$  and  $K_h$  are calculated as

$$k_m = C_k l \sqrt{e}$$

$$k_h = (1 + 2l / \Delta) k_m$$

The SGS length  $l$  depends on the stratification and is computed following Deardorff. Let  $\Delta = (\Delta x \Delta y \Delta z)^{1/3}$  be a characteristic grid size, then  $l = \Delta$  if the atmosphere is neutral or unstable, and  $l = \max(0.1\Delta, \min(\Delta, 0.76\sqrt{e/N}))$  if the atmosphere is stable (where  $N$  is the Brunt-Väisälä frequency). Although  $C_k$  and  $C_\varepsilon$  can be estimated from the inertial subrange theory (Lilly, 1967), they are set to  $C_k = 0.1$ , and  $C_\varepsilon = (0.19 + 0.51l / \Delta)$  following Deardorff.

The boundary conditions are essentially the same as that of Moeng (1984) except that we impose a Galilean transformation at the sea-surface. The top and bottom boundaries are rigid ( $w=0$ ), which implies that all resolved scale vertical fluxes vanish there, and the vertical transport of momentum and scalar quantities is done solely by the SGS fluxes. The SGS fluxes at the surface are computed using the

formulae similar to the bulk aerodynamic method (for detail, see Khairoutdinov and Kogan, 1996).

At the upper boundary, the vertical gradients of the scalar quantities are fixed as the initial values, and the SGS momentum flux is set to be zero. To minimize the reflection of the vertically propagating gravity waves from the upper boundary, an absorbing layer with Rayleigh-type damping is introduced in the upper part of the domain.

## 2.2 Microphysical and radiative processes

Two different formulations of microphysical processes are implemented in the model. The first is a bulk approach in which five moments of the drop spectra (cloud and drizzle drop number concentration, cloud and drizzle liquid water content, and the mean cloud drop radius) are predicted in the model. The bulk parameterization is described in detail by Khairoutdinov (1997). Another one is the explicit microphysical approach (Kogan et al., 1995), in which the explicit microphysical processes of nucleation, condensation, evaporation, coalescence and fallout are described based on two distribution functions: one for aerosol (19 categories from 0.0076 to 7.6 micron) and the other for cloud drops (25 categories on a logarithmic scale from 1 to 256 microns). The aerosol mass distribution function  $g(x,y,z,n,t)$  is defined such that  $g(x,y,z,n,t)dn$  is the number of aerosol per unit volume at the point  $x, y, z$  in the mass range between  $n$  and  $n+dn$ . The governing equation for  $g(x,y,z,n,t)$  ( $g_j$  in the discrete form,  $j$  being the aerosol size category) is:

$$\frac{\partial g_j}{\partial t} + \frac{\partial}{\partial x_k} (\bar{u}_k g_j) = -R_j + E_j + \frac{\partial}{\partial x_k} (K_h \frac{\partial g_j}{\partial x_k}) \quad (2.8)$$



The changes of aerosol concentration are the results of nucleation ( $R_j$ ), cloud drop evaporation ( $E_j$ ) and turbulent diffusion.

The nucleation term ( $R_j$ ) is calculated based on the aerosol spectrum and the supersaturation at each grid point. The aerosols in a specific size interval are activated as soon as the supersaturation ( $\bar{S}$ ) exceeds the critical value determined by the Kohler equation,

$$\bar{S} - \frac{a}{r} + \frac{b}{r^3} = 0 \quad (2.9)$$

where the term  $a/r$  expresses the increase in saturation ratio over a droplet as compared to a plane surface. The term  $b/r^3$  represents the reduction in vapor pressure due to the presence of a dissolved substance. Numerically,

$$a \approx \frac{3.3 \cdot 10^{-5}}{T} \text{ (cm)} \quad b \approx \frac{4.3iM_s}{m_s} \text{ (cm}^3\text{)}$$

where  $T$  is temperature,  $i$  is the number of ions into which each molecule of salt dissociates ( $i=2$  for sodium chloride and ammonium sulfate).  $M_s$  and  $m_s$  are the mass and molecular weight of the dissolved substance, respectively.

The evaporation term ( $E_j$ ) represents the regeneration of aerosols due to the evaporation of cloud drops. It is computed based on the growth equation of the cloud drops. The cloud drops in a specific size interval are evaporated as soon as the drop radius becomes smaller than the corresponding critical wet radius.

The diffusive growth/evaporation of the cloud droplets is calculated as,

$$\frac{dm}{dt} = \frac{4\pi r f_v}{F_K + F_D} \left( \bar{S} - \frac{a}{r} + \frac{b}{r^3} \right) \quad (2.10)$$

where  $F_K$  and  $F_D$  represent the effects of heat conductivity and the vapor diffusivity, respectively.  $f_v$  is the ventilation factor.

The drop mass distribution function is defined such that  $f(x,y,z,m,t)dm$  is the number of drops at point  $x,y,z$  with mass in the range between  $m$  and  $m+dm$ . The equation for the cloud drop spectrum  $f(x,y,z,m,t)$  ( $f_i$  in the discrete form,  $i$  being the drop size category) is:

$$\frac{\partial f_i}{\partial t} + \frac{\partial}{\partial x_k}(\bar{u}_k f_i) = R_i + D_i + C_i + S_i + \frac{\partial}{\partial x_k}(K_h \frac{\partial f_i}{\partial x_k}) \quad (2.11)$$

The changes in cloud drop concentration  $f_i$  are the results of nucleation ( $R_i$ ), diffusive growth/evaporation ( $D_i$ ), collection ( $C_i$ ), sedimentation ( $S_i$ ) and turbulent diffusion. The equations for the aerosol and cloud droplet distribution functions allow prediction of aerosol and drop spectra starting activation to drizzle formation.

The collection term ( $C_i$ ) is written as,

$$C_i = \frac{1}{2} \int_0^{m_i} W(m_i - m', m') f(m_i - m') f(m') dm' - \int_0^{\infty} W(m_i, m') f(m_i) f(m') dm' \quad (2.12)$$

where  $W(m, m')$  is the collection kernel and is given by,

$$W(m, m') = \pi(r + r')^2 |V(m) - V(m')| E(m, m')$$

and  $E(m, m')$  is the collision efficiency.

The first term on the right-hand side in equation (2.11) is the rate of formation of drops of mass  $m_i$  by coalescence of drops with masses smaller than  $m_i$ . The second term is the rate of removal by combinations of drops mass  $m_i$  with other drops.

The sedimentation term ( $S_i$ ) represents the local accumulation of drops of mass  $m_i$  at a grid point as a result of their fall speed. It is given by

$$S_i = \frac{\partial}{\partial z}(V_i f_i) \quad (2.13)$$

where  $V_i$  is the terminal velocity of a drop of mass  $m_i$ .

The numerical formulation of microphysics (Kogan et al., 1995) was recently refined by implementation of a new variational optimization method for remapping the drop spectra during condensation/evaporation calculations. The method (described in Chapter 3) conserves four moments of the drop size distribution function and significantly minimizes the numerical diffusion of the drop spectra without sacrificing the computational efficiency of the code.

The longwave and shortwave radiation fluxes and the associated heating and cooling rates are calculated using the broad band radiative transfer code developed by Wyant et al. (1997). Tests performed by C. Bretherton show that the solar heating rates calculated by the broad band code agree with the 24 bands Slingo and Shrecker (1982) code with an error less than 5%.

### 2.3 Numerical scheme

The finite-difference discretization is based on the staggered Arakawa C-grid, which means that the velocity components are defined at the sides, and the scalar quantities including the pressure are defined at the center of each grid mesh. The

advective transport of momentum is computed using a flux-conserving advection scheme (Tremback et al., 1987) with an option to select the order of spatial accuracy from the second to the fifth. The advection of scalar variables (including TKE, thermodynamic variables and microphysical variables) is calculated using the three dimensional positive definite and nonoscillatory version of the Smolarkiewicz and Grabowsky (1990) advection scheme. The time integration for the momentum equation is performed using the third-order Adams-Bashforth scheme.

## **Chapter**

# **3**

## **Variational Optimization Method for Calculation of Cloud Drop Growth in an Eulerian Drop-Size Framework**

### **3.1 Introduction**

The current generation of cloud microphysical models that combine three-dimensional dynamics and an explicit formulation of microphysics, requires an Eulerian drop-size framework in which drop sizes are fixed. The evolution of the spectra is described by varying the number concentration and/or mass within each size category. As a result of the drop growth processes, such as

condensation/evaporation, coagulation, etc., new size categories will form that need to be remapped to the Eulerian fixed bin sizes at the end of each time step. It is during the remapping procedure that the added mass in the case of condensation (or number concentration in the case of coagulation) is usually spread over the entire bin size interval, resulting in numerical dispersion of the spectra. The numerical dispersion, to a certain degree unavoidable in any Eulerian formulation, if excessive, can result in broadening of the cloud drop spectrum and acceleration of the collection process, thus leading to an earlier development of precipitation. In a similar manner, it may accelerate the evaporation of cloud drops in the descending branches of cloud circulation.

The development of numerical methods for accurate calculation of cloud drop growth in an Eulerian drop-size framework has been the subject of many studies (see, e.g., Kovetz and Olund 1969; Bleck 1970; Egan and Mahoney 1972; Berry and Reinhardt 1974; Young 1974; Ochs and Yao 1978, Tzivion *et. al.* 1987). A simple and computationally efficient method that conserves both the mass and number concentration has been proposed by Kovetz and Olund (1969) (hereafter referred to as KO). In essence, the KO method represents the first-order upwind advection algorithm and results in large numerical diffusion. However, due to its simplicity, the method has been applied both to condensational and coagulation growth calculations. In coagulation calculation, as shown by Ochs (1978), the large numerical dispersion of the method results in artificial production of precipitation. As we will show later in this paper, the KO method gives also quite inaccurate solutions for droplet condensational growth under conditions typical for stratocumulus cloud layers.

A much more accurate method has been developed by Egan and Mahoney (1972) (referred hereafter as EM). This method conserves the zero (drop concentration), first (liquid water content) and second (radar reflectivity) moments of a drop mass distribution. Later, Ochs and Yao (1978) extended the technique to a non-uniform exponential mass coordinate and applied it for collection and breakup, as well as for condensation calculations. Young (1974) proposed a numerical method using separate number and mass conservation equations, thus allowing sub-bin resolution. Both EM and Young's methods provide much more accurate solutions than single moment schemes and have been successfully used in models with simplified dynamic frameworks. It has to be noted, however, that the use of higher moments of the distribution function increases the number of microphysical variables that need to be retained in the EM method by a factor of three and, in the Young's method, by a factor of two. In multidimensional models, the computational burden of these methods is quite significant.

Liu *et. al.* (1995) described a variational optimization (VO) method that requires specification of only one variable in each bin size. The method significantly limits the numerical dispersion and can be formulated to conserve arbitrary number of moments of the drop size distribution. It is also computationally inexpensive and can be easily incorporated in multidimensional cloud models. In the present paper we provide the detailed description of the method and describe modifications of the algorithm for the case of precipitating clouds. The accuracy of the method is tested using more than 15,000 cloud drop spectra generated by the three-dimensional large eddy simulation (LES) cloud model with explicit microphysics (Kogan et al, 1995).

### **3.2 Formulation of the method**

The variational methods, first applied in meteorology by Sasaki (1958), have become powerful tools in optimization, numerical analysis and data assimilation (see, e.g., Lewis, 1972; Stephens, 1970; Ritchie, 1975). In this paper, we apply a variational method for remapping the drop size distribution function during calculations of condensational growth in an Eulerian drop-size framework. In the latter the evolution of a drop spectrum is represented by the changing concentration of drops within the fixed size bins. The variational method controls the numerical dispersion by imposing the moment-conserving constraints. In the following discussion, we denote the drop radius in each stationary bin as  $r_i$  ( $i=1, 2, \dots, K$ ) assuming for convenience  $r_1 < r_2 < \dots < r_K$ . Let us consider a distribution of which the cloud droplet number is  $N_i^*$  in bin  $i$ . As condensation occurs, the drop radius in  $i$ -th category grows from  $r_i$  to  $r_i^*$ . Our goal is to find the new drop numbers in each stationary bin.

We start with the first guess of a spectrum which is obtained by the KO method. The first guess conserves the total number of cloud drops and the total liquid water content.

Now, we define the cost function in the form

$$J = \frac{1}{2} \sum_{i=1}^K w_i (N_i - \tilde{N}_i)^2 \quad (3.1)$$

subject to the strong constraints

$$\sum_{i=1}^K N_i = C \quad (3.2)$$

$$\sum_{i=1}^K N_i r_i = R \quad (3.3)$$



$$\sum_{i=1}^K N_i r_i^2 = S \quad (3.4)$$

$$\sum_{i=1}^K N_i r_i^3 = Q \quad (3.5)$$

where  $w_i$  are the weights ( $w_i > 0$ ) defined later in this section.  $\tilde{N}_i$  is the cloud drop number in category  $i$  of the first guess, and  $N_i$  is the sought after new cloud drop number concentration. The new spectrum  $(r_i, N_i)$  conserves the zero, first, second and third moments of the distribution  $(r_i^*, N_i^*)$  which represent the total droplet number, mean droplet radius, total droplet surface area and the total liquid water content (hence, the effective radius is also conserved). The zero ( $C$ ), first ( $R$ ), second ( $S$ ) and the third moments ( $Q$ ) of the distribution  $(r_i^*, N_i^*)$  are defined as,

$$C = \sum_{i=1}^K N_i^* \quad R = \sum_{i=1}^K N_i^* r_i^*$$

$$S = \sum_{i=1}^K N_i^* (r_i^*)^2 \quad Q = \sum_{i=1}^K N_i^* (r_i^*)^3$$

By requiring the minimum of the cost function through the use of Lagrangian function  $L$  and Lagrangian multipliers  $\lambda_1, \lambda_2, \lambda_3$  and  $\lambda_4$

$$L = \frac{1}{2} \sum_{i=1}^K w_i (N_i - \tilde{N}_i)^2 + \lambda_1 \left( \sum_{i=1}^K N_i - C \right)$$

$$+ \lambda_2 \left( \sum_{i=1}^K N_i r_i - R \right) + \lambda_3 \left( \sum_{i=1}^K N_i r_i^2 - S \right) + \lambda_4 \left( \sum_{i=1}^K N_i r_i^3 - Q \right)$$

one can obtain:

$$w_i (N_i - \tilde{N}_i) + \lambda_1 + \lambda_2 r_i + \lambda_3 r_i^2 + \lambda_4 r_i^3 = 0 \quad (3.6)$$

Solving for  $N_i$  from equation (3.6),

$$N_i = \tilde{N}_i - \frac{1}{w_i}(\lambda_1 + \lambda_2 r_i + \lambda_3 r_i^2 + \lambda_4 r_i^3) \quad (3.7)$$

and substituting equation (3.7) into equations (3.2), (3.3), (3.4) and (3.5), we obtain four equations for four unknowns  $\lambda_1, \lambda_2, \lambda_3$  and  $\lambda_4$  which give:

$$\begin{aligned} \lambda_1 &= \frac{\Delta_1}{\Delta}, & \lambda_2 &= \frac{\Delta_2}{\Delta}, \\ \lambda_3 &= \frac{\Delta_3}{\Delta}, & \lambda_4 &= \frac{\Delta_4}{\Delta} \end{aligned} \quad (3.8)$$

where

$$\Delta = \begin{vmatrix} a_1 & b_1 & c_1 & d_1 \\ a_2 & b_2 & c_2 & d_2 \\ a_3 & b_3 & c_3 & d_3 \\ a_4 & b_4 & c_4 & d_4 \end{vmatrix} > 0$$

$$\Delta_1 = \begin{vmatrix} \Delta C & b_1 & c_1 & d_1 \\ \Delta R & b_2 & c_2 & d_2 \\ \Delta S & b_3 & c_3 & d_3 \\ \Delta Q & b_4 & c_4 & d_4 \end{vmatrix}, \quad \Delta_2 = \begin{vmatrix} a_1 & \Delta C & c_1 & d_1 \\ a_2 & \Delta R & c_2 & d_2 \\ a_3 & \Delta S & c_3 & d_3 \\ a_4 & \Delta Q & c_4 & d_4 \end{vmatrix}$$

$$\Delta_3 = \begin{vmatrix} a_1 & b_1 & \Delta C & d_1 \\ a_2 & b_2 & \Delta R & d_2 \\ a_3 & b_3 & \Delta S & d_3 \\ a_4 & b_4 & \Delta Q & d_4 \end{vmatrix}, \quad \Delta_4 = \begin{vmatrix} a_1 & b_1 & c_1 & \Delta C \\ a_2 & b_2 & c_2 & \Delta R \\ a_3 & b_3 & c_3 & \Delta S \\ a_4 & b_4 & c_4 & \Delta Q \end{vmatrix}$$

and

$$a_1 = \sum_{i=1}^K \frac{1}{w_i}, \quad b_1 = \sum_{i=1}^K \frac{r_i}{w_i}, \quad c_1 = \sum_{i=1}^K \frac{r_i^2}{w_i}, \quad d_1 = \sum_{i=1}^K \frac{r_i^3}{w_i}$$

$$a_2 = b_1, \quad b_2 = c_1, \quad c_2 = d_1, \quad d_2 = \sum_{i=1}^K \frac{r_i^4}{w_i}$$

$$a_3 = c_1, \quad b_3 = d_1, \quad c_3 = d_2, \quad d_3 = \sum_{i=1}^K \frac{r_i^5}{w_i}$$

$$a_4 = d_1, \quad b_4 = d_2, \quad c_4 = d_3, \quad d_4 = \sum_{i=1}^K \frac{r_i^6}{w_i}$$

$$\Delta C = \sum_{i=1}^K \tilde{N}_i - C, \quad \Delta R = \sum_{i=1}^K \tilde{N}_i r_i - R$$

$$\Delta S = \sum_{i=1}^K \tilde{N}_i r_i^2 - S, \quad \Delta Q = \sum_{i=1}^K \tilde{N}_i r_i^3 - Q$$

In a very few cases, the determinant  $\Delta$  may become very small ( $< 10^{-7} \sim 10^{-8}$ ), e.g. when the spectrum is very narrow (say cloud drops only spread over less than four bins). In this case, we simply use the KO method without the variational adjustment (see Appendix A). Otherwise, we can solve for  $\lambda_1, \lambda_2, \lambda_3$  and  $\lambda_4$ , and then calculate the adjusted cloud droplet number for each bin  $i$  using equation (3.7).

Variational optimization technique does not impose constraints on the determination of weights ( $w_i$ ) in the cost function. In most variational optimization problems the weights are chosen empirically based on the specifics of the problem. Liu *et al.* (1995) give the weights as  $w_i = \tilde{N}_i^{-\gamma}$ , where  $\gamma=1.0$ . A series of numerical tests using a Lagrangian air parcel model which provides an exact solution of the condensation problem showed that this weight function works very well in the case of non-precipitating clouds. However, in the case of precipitating stratocumulus or convective clouds where the cloud drop size range covers hundreds and even thousands microns, much better results are obtained by the weights in the form  $w_i = \tilde{N}_i / (1 + (r_i / \beta)^3)$ , where  $\beta=10 \mu\text{m}$ . Our tests showed that this weight function works equally well in the case of non-precipitating clouds.

### 3.3 Description of the Lagrangian air parcel model

The Lagrangian air parcel model used in our tests follows that of Kornfeld (1970). We consider an air parcel which contains dry air, water vapor and cloud drops, and is rising adiabatically. The heat balance equation during the moist-adiabatic process (see Byers, 1965) is,

$$-LdG_v - sG_w dT = (G_a + G_v)[C_p dT - R_v T d \ln(p)]$$

Here  $L$  is the latent heat of vaporization, and  $s$  is the specific heat of water.  $G_a$ ,  $G_v$  and  $G_w$  are the mass of dry air, water vapor and liquid water in the air parcel, respectively.  $T$  and  $p$  are the temperature and pressure of the air parcel, respectively.  $C_p$  is the specific heat of dry air at constant pressure. The specific gas constant for moist air,  $R_v$ , is given by

$$R_v = (1 + 0.608w)R_a$$

where  $R_a$  is the specific gas constant for dry air,  $w = G_v/G_a$  is the water vapor mixing ratio.

Combing the heat balance equation, the equation of state for the moist air,  $p = \rho R_d T_v$ , and the vertical equation of motion,  $dp/dz = -\rho(g + du/dt)$ , one obtains,

$$\frac{dT}{dt} = \frac{-(G_a + G_v)(g + du/dt)u - L(dG_v/dt)}{(G_a + G_v)C_p + sG_w} \quad (3.9)$$

$$\frac{dp}{dt} = \frac{-p(g + du/dt)u}{R_v T} \quad (3.10)$$

where  $u = dz/dt$  is the vertical velocity of the air parcel.

Since  $G_v + G_w$  is conserved during the moist adiabatic process, we have

$$-\frac{dG_v}{dt} = \frac{dG_w}{dt} = \sum_i N_i \frac{dm_i}{dt} \quad (3.11)$$

where  $dm_i / dt$  is the condensational diffusion growth rate for a cloud drop with the mass  $m_i$  in bin  $i$ , which after neglecting both the curvature and the salt factor can be written as (Houze, 1993),

$$\frac{dm_i}{dt} = \frac{4\pi r_i f_v \tilde{S}}{F_K + F_D} \quad (3.12)$$

Here  $F_K$  and  $F_D$  represent the effects of heat conductivity and the vapor diffusivity, respectively,  $f_v$  is the ventilation factor,  $\tilde{S}$  is the supersaturation which is defined as  $\tilde{S} \equiv e / e_s(T) - 1$ , where  $e$  is the ambient vapor pressure and can be calculated as  $e = pw / (0.622 + w)$ ,  $e_s(T)$  is the saturation vapor pressure given as (Murray, 1967),

$$e_s(T) = 6.1078 \exp\left[\frac{17.2694(T - 273.16)}{T - 35.86}\right]$$

The set of equations (3.9)-(3.12) can be solved very accurately numerically in a Lagrangian drop-size framework and provides the benchmark (exact) solution of the condensation process. The solutions of the KO, EM and VO schemes are obtained by remapping the drop spectrum to the Eulerian drop size framework at every time step, therefore they are subject to numerical diffusion errors.

### 3.4 Verification of the method in a Lagrangian model

We first show results of the test of the VO method in a Lagrangian air parcel model. A Gamma-type distribution is specified initially (Berry, 1967) with the liquid water content of  $0.2 \text{ g m}^{-3}$  and drop concentration of  $50 \text{ cm}^{-3}$  (Fig. 3.1). The stationary bin sizes are defined as  $r_i = r_1 \exp[(i-1) / I_0]$ , ( $i=1, 2, \dots, 25$ ) with

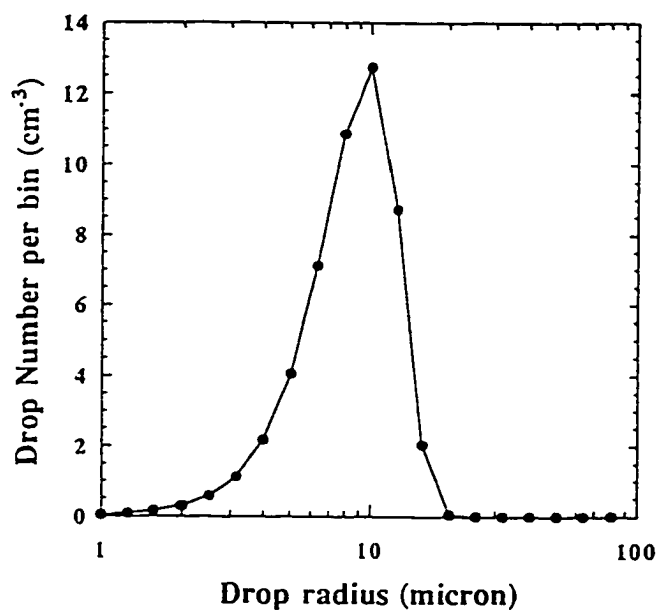


Figure 3.1. Initial cloud drop spectrum used in the first two sets of experiments to verify the variational optimization method. The spectrum is assumed to be a Gamma distribution with liquid water content  $0.2 \text{ g/m}^3$  and cloud drop concentration  $50 \text{ cm}^{-3}$ .

$I_0 = 3 / \ln 2$ . The bin sizes cover the range from  $r_l = 1 \mu\text{m}$  to  $256 \mu\text{m}$  and are the same as in the CIMMS LES cloud model (Kogan et al. 1995).

The accuracy of the VO method was evaluated in two sets of experiments, in which only condensation and evaporation processes were considered. In the first test, the air parcel ascended with a constant vertical velocity of 1.0 m/s. The drop spectra were computed using three different methods: Kovetz and Olund (1969), Egan and Mahoney (1972), and the present variational optimization method. All three methods employ an Eulerian drop size framework. The initial supersaturation is set to be 0.2%. Figs. 3.2a and 2b show the resulting size distribution of drop number and mass at the 200 m height. The exact solution obtained in a Lagrangian model is plotted as the solid line. As evident from Figs. 3.2a, 2b and 2f, the KO method has a significant numerical dispersion, while the EM scheme has a relatively small numerical dispersion error. Since all three schemes conserve drop number and mass, the liquid water content (Fig. 3.2c) is determined rather accurately in all three methods. The other moments of the distribution function, such as the mean and effective radius, standard deviation, are more accurately calculated by the EM and VO schemes. The VO method produces the smallest error not only in the prediction of the integral parameters of the spectrum, such as liquid water content, mean radius, effective radius and the relative standard deviation of the spectrum (Figs. 3.2c-2f), but also for the spectrum itself (Figs. 3.2a and 2b).

In the second set of experiments, the performance of various methods was evaluated both for condensation and evaporation processes. For this purpose we follow an air parcel in both ascending and descending branches of its trajectory by specifying the vertical velocity variation according to the formula:

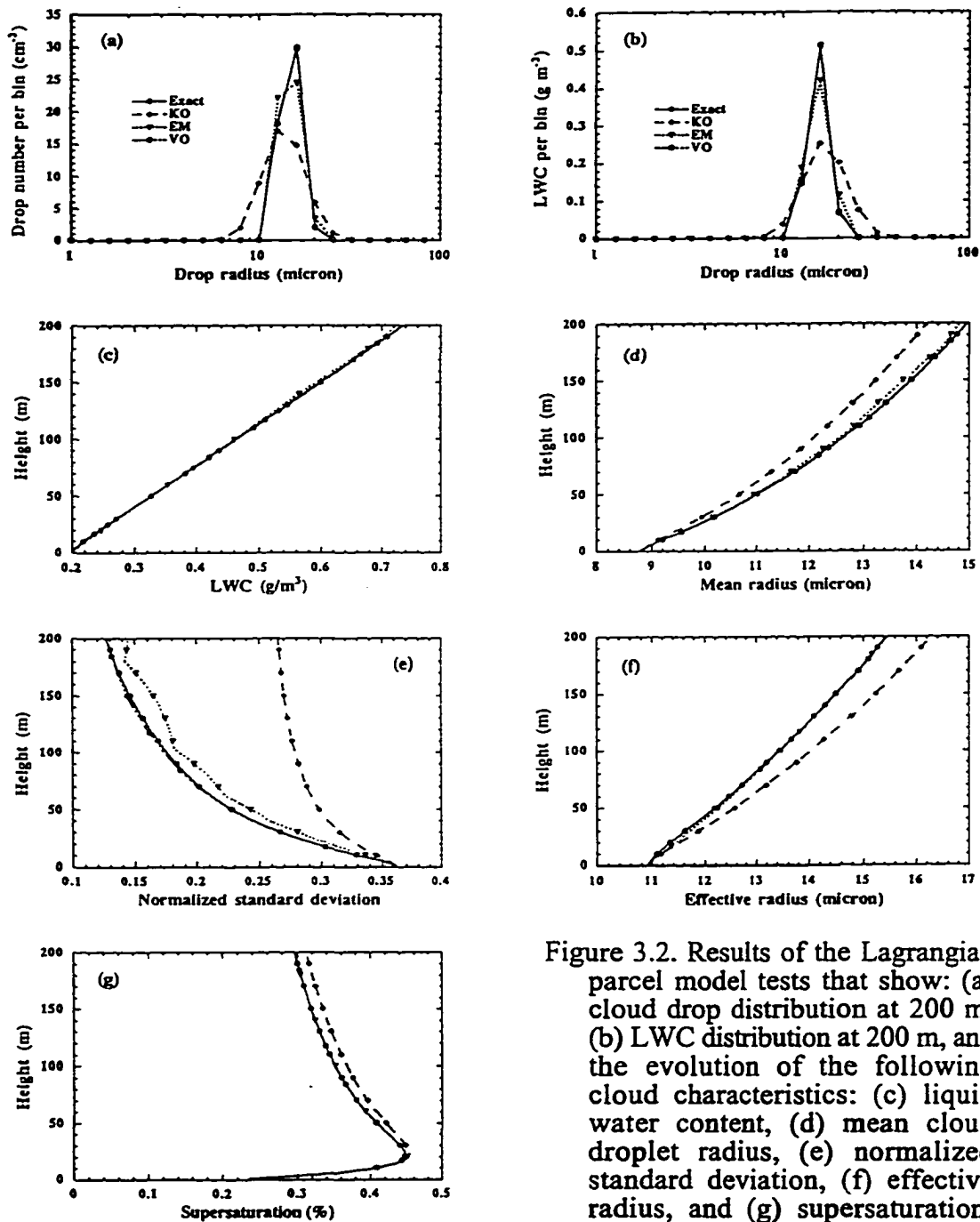


Figure 3.2. Results of the Lagrangian parcel model tests that show: (a) cloud drop distribution at 200 m, (b) LWC distribution at 200 m, and the evolution of the following cloud characteristics: (c) liquid water content, (d) mean cloud droplet radius, (e) normalized standard deviation, (f) effective radius, and (g) supersaturation. Solid lines represent the exact

solution given by the Lagrangian drop size framework, others from the Eulerian drop size framework. Long dashed lines with diamonds show the results of the KO method, dotted lines with triangles represent the results of the EM method, dot-dashed lines with circles show the results of the variational method (VO). The vertical velocity is 1 m/s and the time step is 1.0 second.



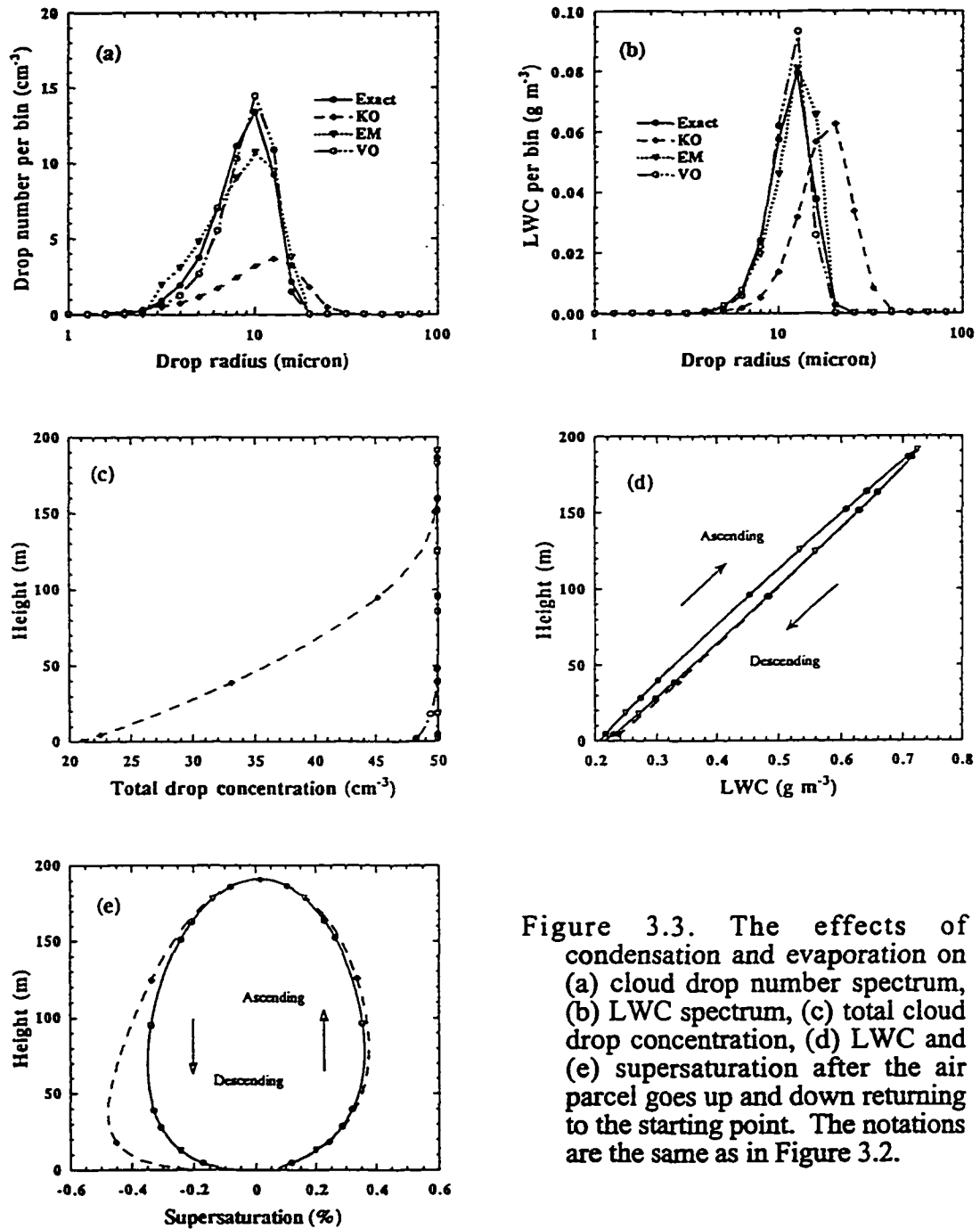


Figure 3.3. The effects of condensation and evaporation on (a) cloud drop number spectrum, (b) LWC spectrum, (c) total cloud drop concentration, (d) LWC and (e) supersaturation after the air parcel goes up and down returning to the starting point. The notations are the same as in Figure 3.2.

$$u = u_1 + u_2 \sin(\omega t) \quad (3.13)$$

with  $u_1=0$ .,  $u_2=1$  m/s and  $\omega = 2\pi/600$  s<sup>-1</sup>. The integration is made for 600 seconds during which time the air parcel first moves upward reaching the height of about 191 meters, and then moves downward to the same starting point, thus completing a cycle. Figs. 3.3a and 3b show the size distribution of drop concentration and LWC in the air parcel at the end of the cycle. The results are remarkably good for both the EM and VO schemes which both preserve well the spectrum shape. The EM scheme does exhibit a moderate dispersion, while the VO method has a small phase error. The KO method shows a very significant dispersion (largest in both diffusion and phase error). Due to the strong dispersion, the KO method results in evaporation of a significant number of cloud drops (58%). Only a small fraction (less than 4%) of cloud drops evaporates in the VO scheme (Fig. 3.3c).

### **3.5 Modification of the VO method for precipitating clouds**

The VO method has been implemented in the CIMMS LES model with explicit microphysics (Kogan et al. 1995). The three-dimensional experiments showed that the method works very well in simulations of non-precipitating stratocumulus clouds. Since coalescence is weak in these clouds, the cloud drop spectra are mostly unimodal and occupy a rather limited size range from 1 to 50 microns in radius. The situation is more complex in the case of precipitating clouds where bimodal drop size distributions are quite common. In this case, the constraints to conserve four moments of the drop distribution imposed by the VO method may lead to artificial reduction in the drop concentration at the tails of the spectrum. The right "large droplet" tail of the spectrum is especially important as it determines the onset of coagulation and rain/drizzle formation rates.

The problem can be effectively solved and the concentration of drops at the spectrum tails preserved by applying the VO method to the central part of the drop spectrum and to each of its tails separately. The decomposition of the spectrum into three sub-spectra produces the smallest error when the sub-spectra are smooth and do not have sharp discontinuities. This can be achieved by using Gamma distribution function in the decomposition procedure described in Appendix B and illustrated conceptually in Fig. 3.4.

The VO method modified for precipitation clouds was tested in a two different sets of experiments. The first set used two typical spectra produced as a result of the coalescence process and characterized by the long large-drop tail and double peaks in the LWC distribution. The spectra were obtained using Berry and Reinhardt (1974) coalescence model that was initialized with a Gamma type drop distribution with LWC of  $1.0 \text{ g m}^{-3}$  and cloud drop concentration of  $50 \text{ cm}^{-3}$ . The coalescence model was run for 316 and 476 seconds, respectively, to obtain the spectra 1 and 2 shown in Figs. 3.5a, b. Figs. 3.5a, b also show the decomposition of the two spectra into 3 parts. The spectra 1 and 2 shown in Figs 3.5 a, b were then used as the input spectra for the Lagrangian condensation parcel model and run for another 500 time steps with a constant vertical velocity of 1.0 m/s. As in the experiments described in section 3, the exact solution of the Lagrangian condensation model is then compared to the solution given by the VO method in the Eulerian framework. The present experiments, however, use spectra 1 and 2 that have a significant drizzle mode compared to initial spectrum shown in Fig. 3.1. The results of the experiments are shown in Figs. 3.5c and d (note the difference in scales in Fig 3.5 due to the increase in LWC as a result of condensation). The modified VO method that uses the decomposition procedure provides more accurate solution than the old version of the VO method, especially for the large drop tail of the spectra. The

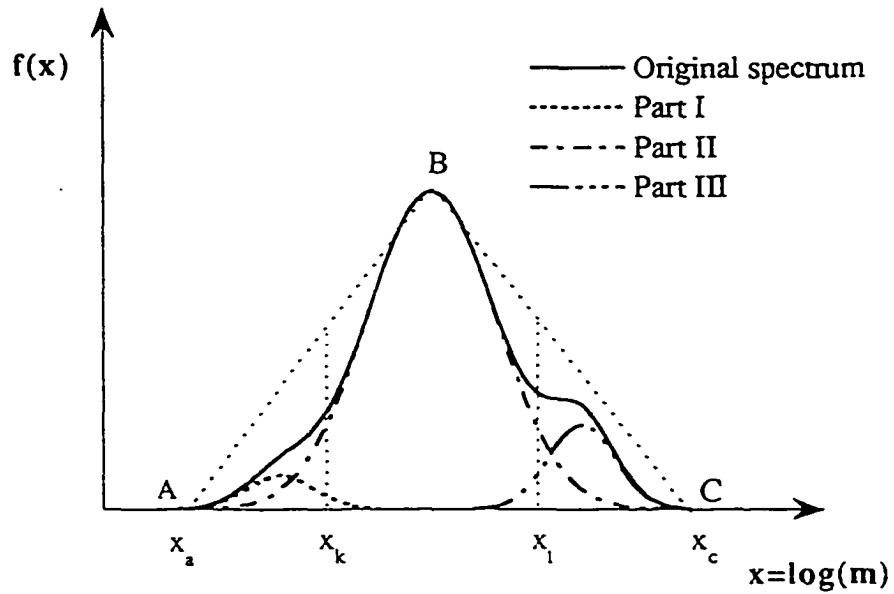


Figure 3.4. The conceptual model illustrating the decomposition procedure described in Appendix B. Here  $f(x)$  denotes the LWC per bin, and  $x$  is the logarithm of cloud drop mass  $m$ .

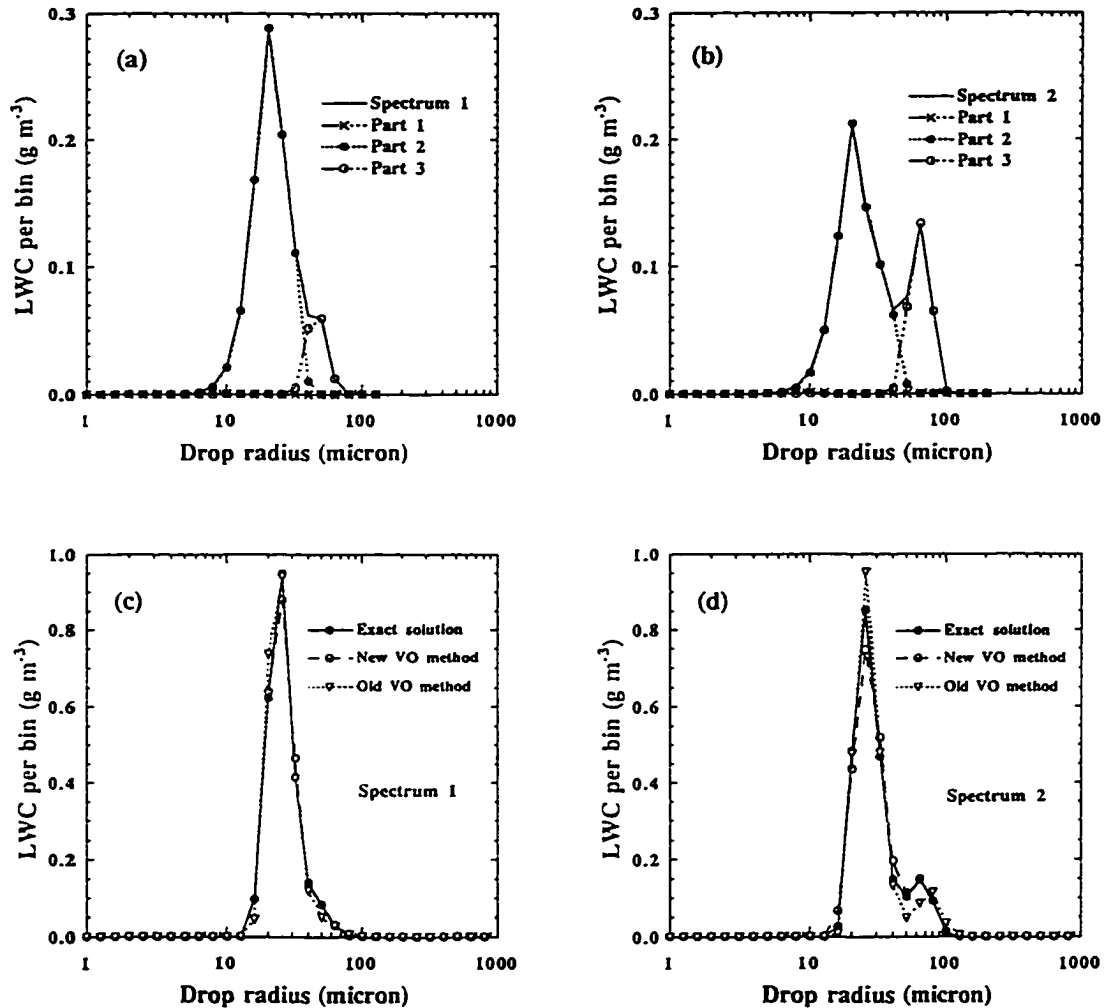


Figure 3.5. Two typical spectra produced by coalescence model and the results from Lagrangian parcel model tests. (a) and (b) show the LWC spectra and their decompositions into three parts for spectrum I (long large-drop tail) and spectrum II (bimode distribution), respectively. (c) and (d) show the averaged solution and errors from Lagrangian parcel model tests at 500 time steps for spectrum I and spectrum II, respectively. In this set of experiments, the vertical velocity is 1 m/s and the time step is 1.0 second.

increased accuracy in this size range is especially important for drizzle and rain prediction in precipitating clouds.

The tests of the method so far used a rather limited set of spectra. In the second set of experiments, we used a much wider variety of spectra obtained under a broad range of dynamic conditions typical for stratocumulus clouds. These spectra were produced by a three-dimensional LES model initialized with data set obtained by Nicholls during the field experiment conducted in the Northern Atlantic (Nicholls, 1984). The case study based on this data set is described in Kogan *et. al.* (1995) and showed reasonably good agreement between the LES model predicted microphysics and observations. The model simulation provided us with more than 15,000 spectra which comprised the data set with LWC in the range of 0.1-0.5 g/m<sup>3</sup> and drop concentrations in the range of 30-90 cm<sup>-3</sup>. The whole data set was divided into four groups based on the radar reflectivity parameter  $Z = \sum_i N_i r_i^6 / \sum_i N_i$ . The latter parameter allows us to separate the data set into groups with different values of LWC in the drizzle mode size range. The classification of the spectra is summarized in Table 3.1. The average spectra and the standard deviation of the spectra in each group are shown in Figs. 3.6a, b and 3.7a, b.

Each of the 15,300 spectra was tested in the Lagrangian parcel model described in section 3.3. The vertical velocity of the air parcel was specified according to (3.9) with  $w_1=0.25$  m/s,  $w_2=0.5$  m/s and  $\omega=\pi/20$  s<sup>-1</sup>. The resulting spectra of the modified VO method are then compared to the exact solutions after 600 time steps. We calculated the averaged difference (error)  $\epsilon_i$  between the solution given by the VO method  $N_i^j$  and the corresponding exact Lagrangian solution  $\tilde{N}_i^j$  as

$$\epsilon_i = \frac{1}{K} \sum_{j=1}^K |(N_i^j - \tilde{N}_i^j)| m_i \quad (3.14)$$

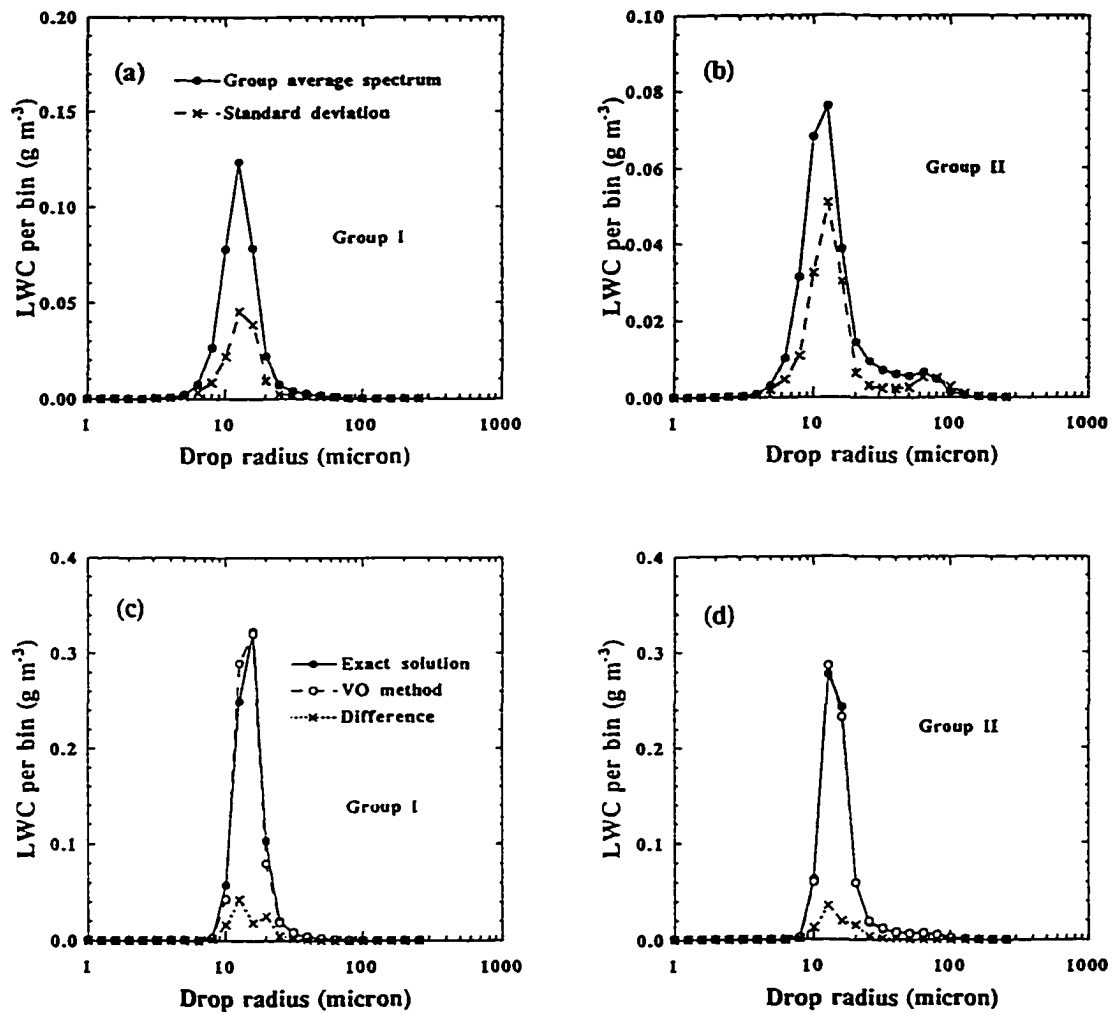


Figure 3.6. Selected spectra from 3-D LES model experiments and the results from Lagrangian parcel model tests. (a) and (b) show the group averaged spectra and their standard deviations for group I and II, respectively. (c) and (d) show the averaged solution and errors from the Lagrangian parcel model tests after 600 time steps for group I and group II, respectively. In this set of experiments, the maximum vertical velocity is 0.75 m/s and the time step is 1.0 second.

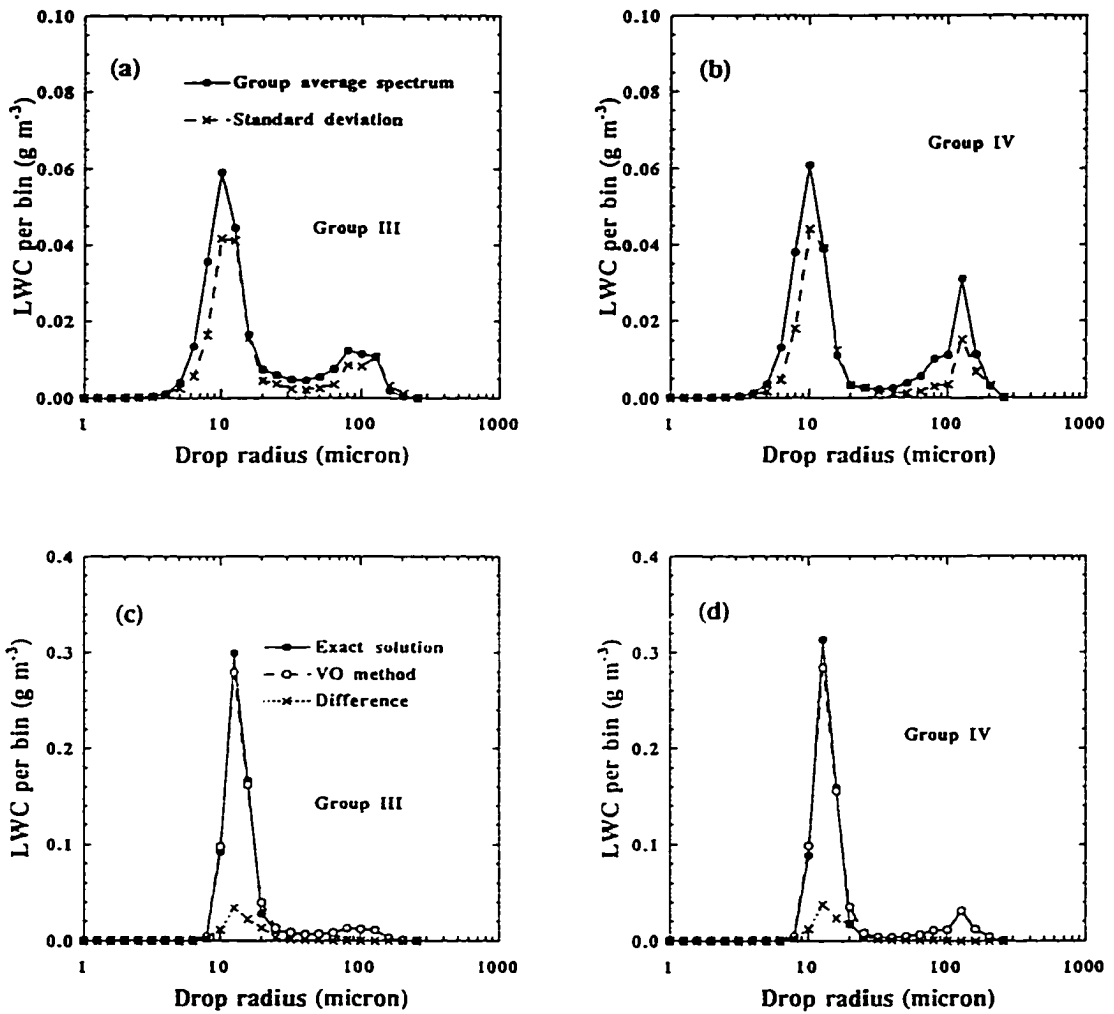


Figure 3.7. Same as in Figure 6 except for spectrum III and IV.



where  $K$  is the total number of spectra in each of the four groups,  $i$  denotes the spectrum bin size and  $j$  denotes the individual spectrum in each of the four groups described in Table 3.1.

**Table 3.1: Classification of the cloud drop spectra**

| Group   | Radar reflectivity range (cm <sup>6</sup> ) | Total number of spectra | Comment                                |
|---------|---|-------------------------|--|
| I       | 0 ~ 10 <sup>-17</sup>                       | 4,472                   | Unimodal spectra                       |
| II      | 10 <sup>-17</sup> ~ 10 <sup>-16</sup>       | 9,512                   | Long tail in the drizzle range         |
| III     | 10 <sup>-16</sup> ~ 4·10 <sup>-16</sup>     | 1,048                   | Small second peak in the drizzle range |
| IV      | > 4·10 <sup>-16</sup>                       | 268                     | Double peaks of comparable magnitude   |
| Total : |   | 15,300                  |  |

Figs 3.6c, d and 3.7c, d show the exact and the VO method solutions, as well as the error averaged over all spectra in each of the four groups. One can see that the errors are quite small and the VO method provides very satisfactory results; the improvement is especially noticeable in the drizzle size range.

Another way to evaluate the numerical diffusion of the VO method is to compare the relative dispersion of the spectrum that is defined as  $\sigma_r = \sigma / \bar{r}$ , where  $\bar{r}$  is the mean radius, and  $\sigma$  is the standard variance of the spectrum,

$$\sigma = \int_0^{\infty} (r - \bar{r})^2 n(r) dr.$$

**Table 3.2: Averaged standard deviation**

| Group | Exact Solution | VO method |
|-------|----------------|-----------|
| I     | 0.205          | 0.189     |
| II    | 0.203          | 0.206     |
| III   | 0.200          | 0.216     |
| IV    | 0.197          | 0.217     |

Table 3.2 lists the relative dispersion averaged over all spectra in each of the four groups. The results show that small numerical dispersion still exist and, in general, it increases with the broadness of the spectrum. However, even for the broadest spectra in our experiments (groups III and IV), the dispersion error is less than 10%. We would like also to note that the present tests were made using a rather coarse resolution in the drop size coordinate where drop mass doubled every second category. It is our believe that the current generation of computers makes it quite practical to use the finer resolutions of drop spectra with mass doubling every third category. The accuracy of the VO method in this case can be increased even further.

### 3.6 Conclusions

A variational optimization method for condensation/evaporation calculations in an Eulerian drop-size framework has been proposed and tested against the exact

solution given by the Lagrangian air parcel model. The variational method not only conserves the integral parameters of the spectrum, such as drop number, mean radius, mass, and the effective radius, but also provides accurate calculation of the spectrum itself. The accuracy of the variational method is comparable to or even better than the accuracy of the Egan and Mahoney (1972) scheme. The variational method has, however, an important advantage compared to the latter method. It requires specification of only one variable in each bin size, while the EM scheme needs retaining of the three moments of the spectrum, thus tripling the memory requirements in the model. For multidimensional models this presents a serious limitation and makes the application of EM method impractical.

The estimate of CPU time showed that the VO method by itself is about 3.1 times slower than the KO method. However, one has to bear in mind that (1) the remapping in a full multi-dimensional model needs to be done only once during the dynamical time step, and (2) the cost of the remapping is only a small fraction compared to the computational cost of other processes, such as the advection of microphysical variables, etc. Tests with the CIMMS LES model in a 64x64x60 integration domain showed that the old VO scheme for non-precipitating clouds (Liu et al. 1995) increased the total CPU time by 1.1%, while the present version of the VO scheme for precipitating clouds increased the total CPU time by 4.5%. Evidently this CPU time expense is justified given the significant increase in accuracy.

We would like to note that the errors associated with condensational remapping are most significant in the size range of 1 to 200 micron which is typical for drops in stratiform clouds. The application of the VO method for this type of clouds is strongly recommended. In the convective clouds where the drop size range is much wider and the drop spectra sometimes exhibit very complex multimodal

shapes, the performance of the VO method has not been thoroughly tested. However, we do expect a good performance of the VO method in convective cloud models as well for two reasons. First, for large cloud drops ( $r \geq 200 \mu\text{m}$ ) the growth by condensation is very small ( $\Delta r \ll r$ ), therefore, the condensational remapping is rather insensitive to a particular scheme. In addition, for drops larger than 100-200 microns, the condensational growth is much smaller than the coalescence growth, consequently, the errors of the condensational remapping are also smaller than the errors associated with the coagulation calculations. It is our experience that for drops large than 100 microns, the use of a simpler method, such as the Kovetz and Olund's (1969) method, is quite warranted.

## **Chapter**

# **4**

## **A study of aerosol effects on cloud microphysics and radiative properties through "ship track" simulations**

### **4.1 Introduction**

Ship tracks can be formed in well-mixed, as well as in decoupled boundary layers. Material released in a well-mixed boundary layer can be easily advected throughout the boundary layer in a relatively short period of time, whereas its transport may be limited by the stable transition layer in the decoupled case. Other parameters, such as surface heat and moisture flux, solar radiation, buoyancy

associated with the ship effluent and the stability of the transition layer, can also significantly affect the ship track formation and its duration. The diffusion in the well-mixed boundary layer has been studied extensively by many researchers following the pioneering work by Deardorff and Willis (1975). A summarized review can be found in Lamb (1982). The diffusion in the decoupled BL has been studied less and the results are usually case dependent. A series of 3-D LES experiments in a decoupled BL will be described in the present paper.

Another topic that will be investigated in the present paper is the effect of ship tracks on cloud LWC and drizzle formation. Aircraft observations give conflicting evidence on the effect of ship track on LWC. Ferek et al. (1997) show LWC increases in some cases while decreases in the others. Measurements off the coast of southern California on July 10, 1987 by King et al. (1995) show LWC inside the ship track increases by about 20-60%, while measurements on June 8, 1994 in the same area during MAST experiment (Johnson et al. 1995) show that LWC inside the ship track decreases by about 40%. The present paper presents results from a modeling study investigating the effects of boundary layer decoupling and ambient aerosol concentration on ship track formation. We consider modification of the decoupled boundary layer due to changes in surface heat flux, a slight heating of the ship track due to fuel burning, changes in solar heating, and slight variation in the initial temperature profile. We also look at the effects of the ship tracks on the infrequently observed drizzle suppression and compare the liquid water content inside and outside the ship track. The evaluation of the early dispersion rate of the aerosol particles in the well mixed boundary layer and the decoupled boundary layer is given in section 4.2. Section 4.3 presents the microphysical character of the ship track based on observation and our model simulation. Section 4.4 gives our conclusions.

## 4.2 Effects of the boundary layer structure on the ship track formation

In this section we evaluate the rate of early dispersion of a passive scalar from a surface source in two different stratocumulus layer conditions: one well-mixed to the surface and the other decoupled from the surface by a sub-cloud stable layer. The passive scalar represents transport of CCN particles without including the microphysical effects on cloud evolution. Therefore, in these simulations we use the bulk microphysical mode of the CIMMS LES model to evaluate the rate of early dispersion of ship effluent from a surface source under various boundary conditions. The ship track was emulated by predicting the evolution of the passive scalar field. The governing equation for the passive scalar,  $c$ , is

$$\frac{\partial \bar{c}}{\partial t} = -\frac{\partial}{\partial x_j} (\bar{c} \bar{u}_j + \tau_{jc}) - w_s \frac{\partial \bar{c}}{\partial z} \quad (4.1)$$

The model simulations are made on a domain of 40x40x40 grid points for the well-mixed case, and 40x40x50 grid points for the decoupled case. The grid sizes in both cases are  $\Delta x = \Delta y = 100$  m, and  $\Delta z = 20$  m. The simulations were initialized using observations made by the U.K. Meteorological Research Flight C-130 airplane on June 8th, 1994 (case A334, sounding P1) and on June 29th, 1994 (case A348) during MAST experiment. Figs. 4.1 and 4.2 show the measured profiles of the liquid water potential temperature and total water content during these flights (solid line), as well as idealized profiles used for model initialization (dotted line and dashed line). As evident from Figs. 4.1 and 4.2, the boundary layer is well-mixed in the A334 case and is decoupled in the A348 case. In the decoupled case (A348), the boundary layer is divided into two parts separated by a stable transition layer near 0.4 km. The dotted and the dashed lines in Fig. 4.2 are used to initialize two simulations

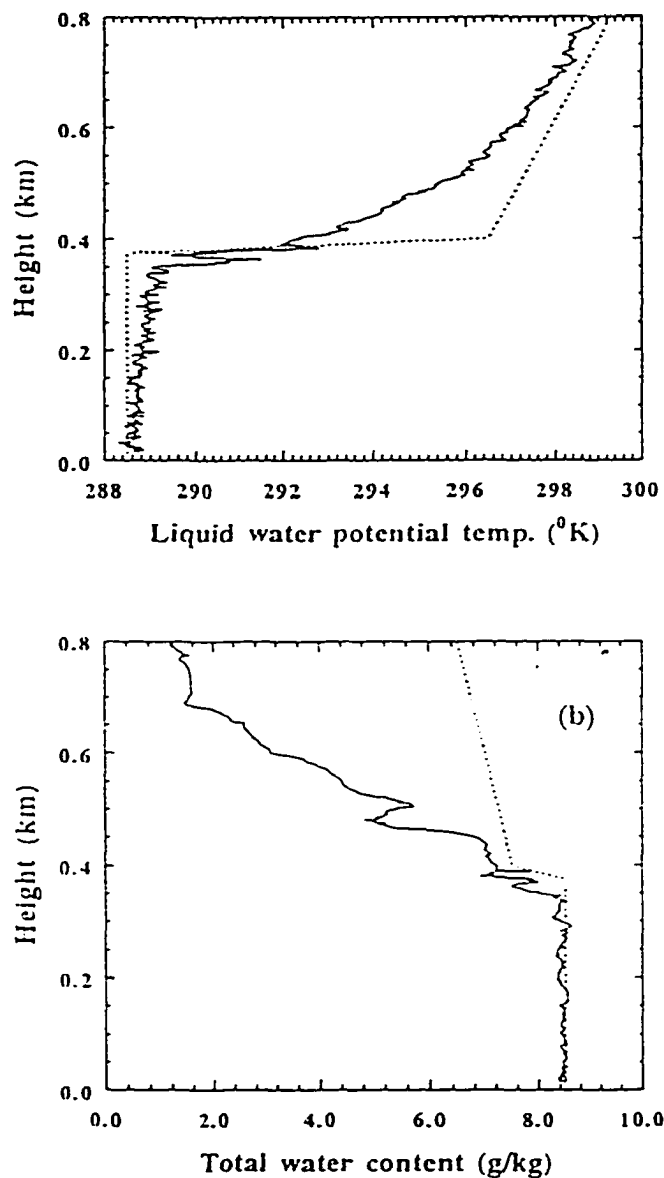


Figure 4.1. Vertical profiles of liquid water potential temperature (upper panel) and total water mixing ratio (lower panel) for the ship track experiment A334. Solid line shows observational soundings obtained on June 8, 1994 during MAST experiment, while dotted line represents smoothed profile used in model initialization.



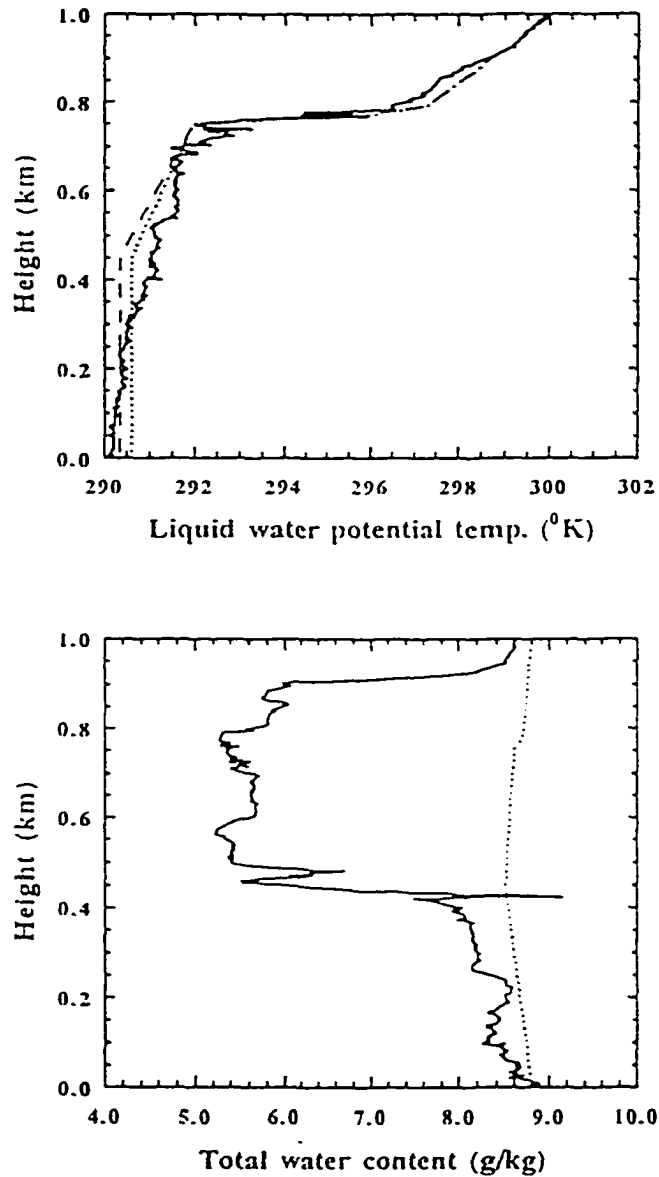


Figure 4.2. Vertical profiles of liquid water potential temperature (upper panel) and total water mixing ratio (lower panel) for the ship track experiment A348. Solid line shows observational soundings obtained on June 29, 1994 during MAST experiment, dotted line represent profile used in initialization of simulations A348, A348B and A348N and the dashed line in simulation A348B1 .

that differ in the strength of the stable transition layer. The results from these simulations are described in section 3f. The water vapor mixing ratio outside the cloud layer is computed from the measured dew point temperature. The latter can not be measured reliably inside the cloud, where it is assumed to be equal to the absolute temperature. The total water mixing ratio in A348 is slightly modified in the model initialization so that LWC in the cloud layer best matches observations after 2 hours of the model spin-up time. The observed geostrophic wind is  $13.0 \text{ ms}^{-1}$  for A334 and  $11.5 \text{ ms}^{-1}$  for A348. The model y-direction is chosen along the geostrophic wind. The surface heat flux is fixed at  $12.0 \text{ Wm}^{-2}$  in A334 and  $10.0 \text{ Wm}^{-2}$  in A348. The large scale divergence, *div*, is fixed at  $2.5 \times 10^{-6} \text{ s}^{-1}$  in both cases. The turbulence is initialized by random perturbations of the horizontal velocities with magnitude  $0.1 \text{ ms}^{-1}$ . After initialization, the model is run for two hours in order for the turbulence to fully develop. The ship track is emulated by predicting the evolution of the passive scalar field. At 7200 s we inject the "ship effluent" along a rectangular column parallel to the y-axis and positioned at  $x=0.5, 0.6, 0.7 \text{ km}$  and  $z=50, 70, 90 \text{ m}$ . The injected passive scalar has a density of 500 dimensionless units, which could be thought of as  $500 \text{ aerosol particles cm}^{-3}$ . Since the governing equation (8) for the passive scalar is linear, one can apply linear operators to the passive scalar field to scale it to the observed aerosol concentrations.

#### a) Well-mixed versus decoupled boundary layer

A well-mixed buoyancy driven boundary layer, normally associated with strong turbulence and relatively large updrafts, can quickly transport material vertically as well as horizontally. The decoupled boundary layer, however, has a stable transition layer which suppresses the vertical motion and limits the amount of material substance reaching the cloud. Figs. 4.3 and 4.4 show time evolution of the

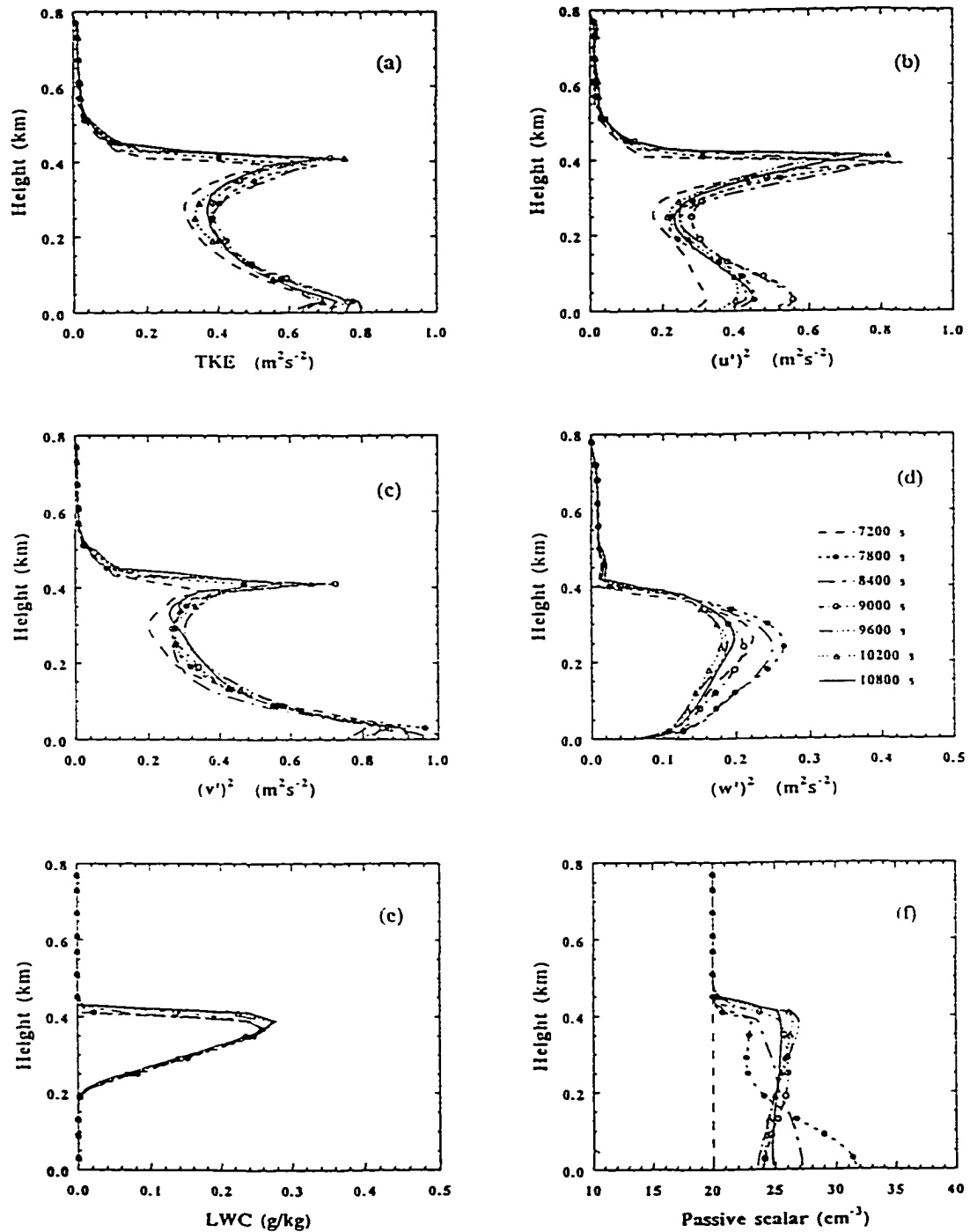


Figure 4.3. Time evolution of horizontally averaged parameters (TKE,  $(u')^2$ ,  $(v')^2$ ,  $(w')^2$ , LWC and passive scalar) in simulation A334. The passive scalar is injected at 7200 second. The model results are shown at 7200 s, 7800 s, 8400 s, 9000 s, 9600 s, 10200 s and 10800 s (see panel d for line notations).

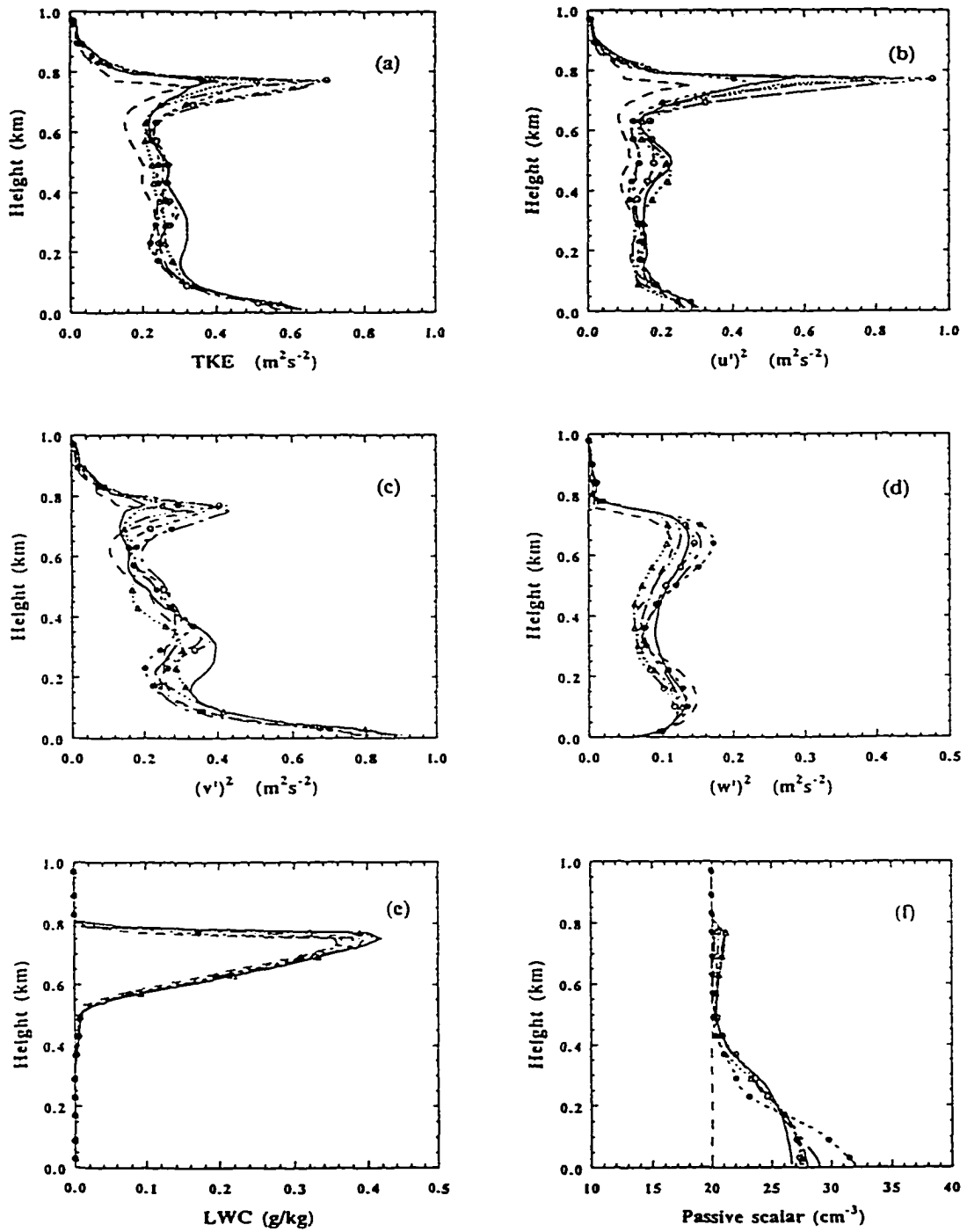


Figure 4.4. Same as in Figure 4.3 except for simulation A348.

horizontally averaged parameters for A334 and A348, respectively. The location of the cloud layer is evident from the LWC profile. The distinction between the well-mixed and the decoupled boundary layer is clearly demonstrated by the vertical velocity variance profile. The  $(w')^2$  profiles clearly show only one maximum for the well-mixed boundary layer compared to two maxima separated by a minimum in the stable transition layer for the decoupled boundary layer. The total turbulent kinetic energy (TKE) profiles are quite different from the  $(w')^2$  profiles in both cases due to the dominance of the horizontal components which tends to be maximized at the top and bottom of the boundary layer. TKE in A348 remains roughly constant in the mixed layer except near the surface and cloud top, whereas the TKE in A334 shows a strong local minimum in the middle of the mixed layer. In the well mixed case, plumes reach the cloud top and spread horizontally, thus generating local maxima of  $(u')^2$  and  $(v')^2$ . Near the surface, the vertical shear of the horizontal velocity is very large. Shearing turbulence near the surface transports significant amount of momentum, thus increasing the variance of the horizontal velocity, especially  $(v')^2$  component. In A348, the boundary layer generates stronger horizontal TKE in the transition region where updrafts from the lower layer and downdrafts from the upper layers bump into each other. The large  $(u')^2$  near cloud top is due to the horizontal spreading of the plumes which penetrate through the stable transition layer and reach cloud top. Both  $(w')^2$  and total TKE in A334 are almost twice as large as in A348 except near the surface and the top of the cloud. Strong TKE and  $(w')^2$  maintains well-mixed boundary layer in A334.

The passive scalar is well-mixed in the boundary layer and transported into the cloud layer in less than 30 minutes in A334, whereas it is mostly confined to the lower half of the boundary layer just under the transition layer in A348 (Fig. 4.4f). The upward transport is dominated by the large eddies (plumes) with very small

contribution from subgrid eddy fluxes. Due to the suppression of large eddies in the transition layer in A348, the vertical advection of the passive scalar is small.

Figs. 4.5a and b show the horizontal cross sections at  $z=0.66$  km 2.5 hours into simulation in A348. Several strong plumes are evident in the simulation domain. The most intense plumes penetrate through the transition layer and transport both water vapor (not shown) and passive scalar into the cloud layer. The localized maxima in the passive scalar field (Fig. 4.5b) correlate well with the location of convective updrafts. A vertical cross section along the "ship track" ( $x=1.2$  km) shows two strong updrafts near  $y=1.0$  km and  $y=3.0$  km (Fig. 4.6a) which are able to penetrate through the weak stable transition layer and transport some amounts of the passive scalar into the cloud layer (Fig. 4.6b).

The fine scale structure of the ship track is evident in Figs. 4.3f and 4.9d which is controlled to a large degree by the buoyant updrafts and downdrafts. This effect has been clearly explained in Lamb (1982) who states that: "material released by a surface source can only ascend or move horizontally. Particles released into the base of an updraft begin their ascent immediately while those emitted into a downdraft move approximately horizontally until eventually they too are swept into updrafts and are carried upward. On the average, the lifetimes of the updraft circulations are long enough that particles that begin to ascend immediately after release are still rising when those that have lingered for a while in the surface layer begin their ascent. Consequently, after a sufficiently large travel time that a majority of particles have entered updrafts, the location of maximum particle concentration lifts off the ground and rises toward the inversion base."

As expected, the passive scalar is rather easily advected throughout the boundary layer in the case of a well-mixed boundary layer. In the decoupled case, the

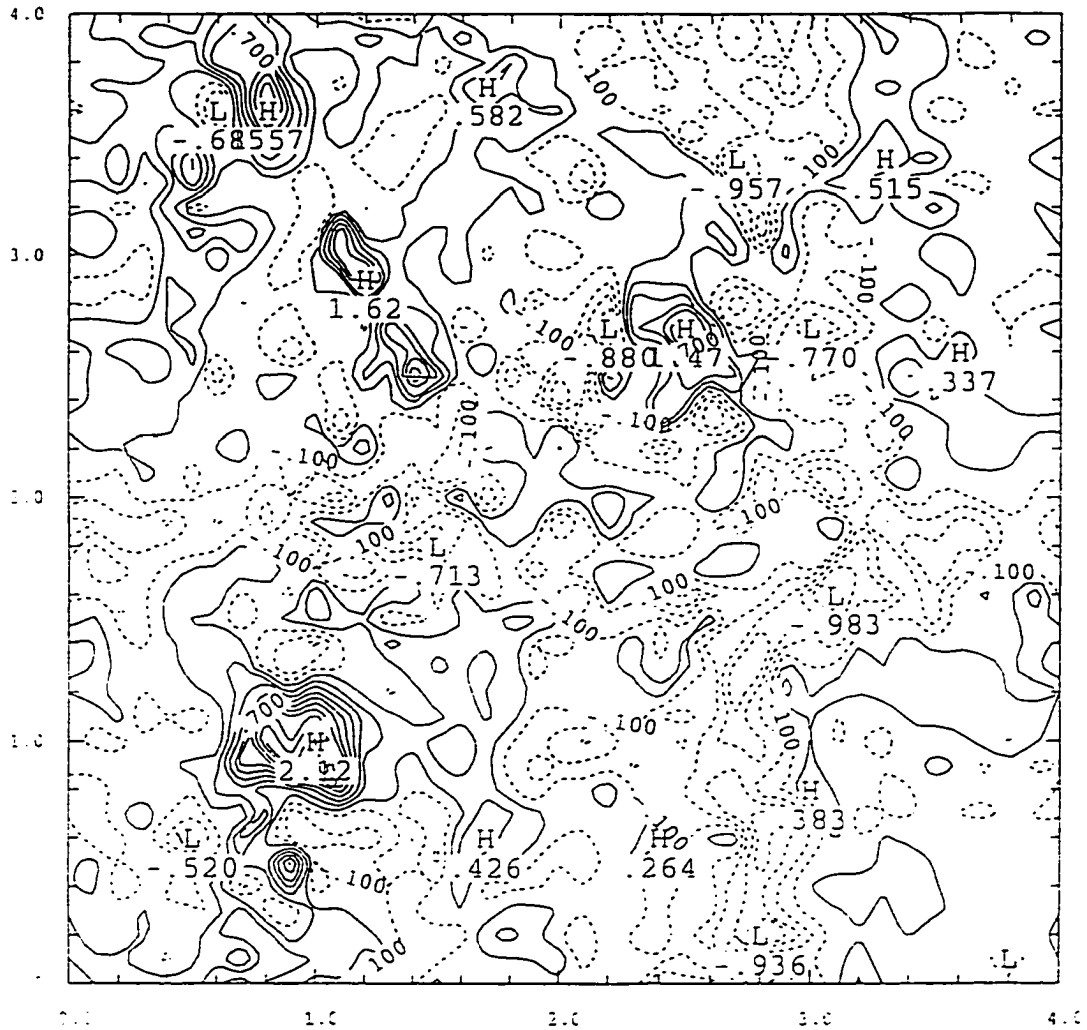


Figure 4.5. Horizontal cross sections ( $z=0.66$  km) of (a) vertical velocity and (b) passive scalar field for simulation A348 at 30 minutes after injection. Several strong plumes can be seen in the simulation domain, those located inside the ship track carry ship effluent into the cloud layer.

A348

SCLR

Z= 0.66

9000.

**b**

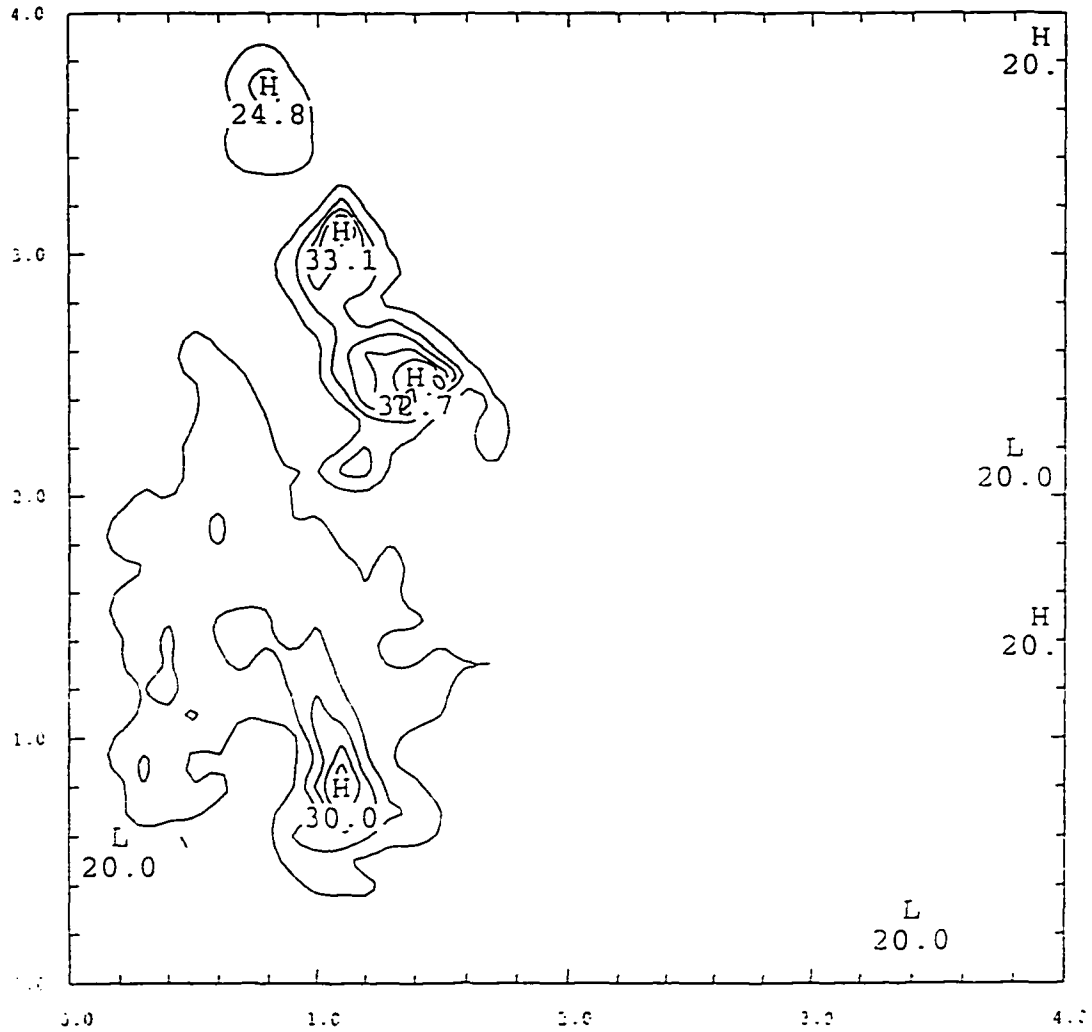


Figure 4.5. (continue)



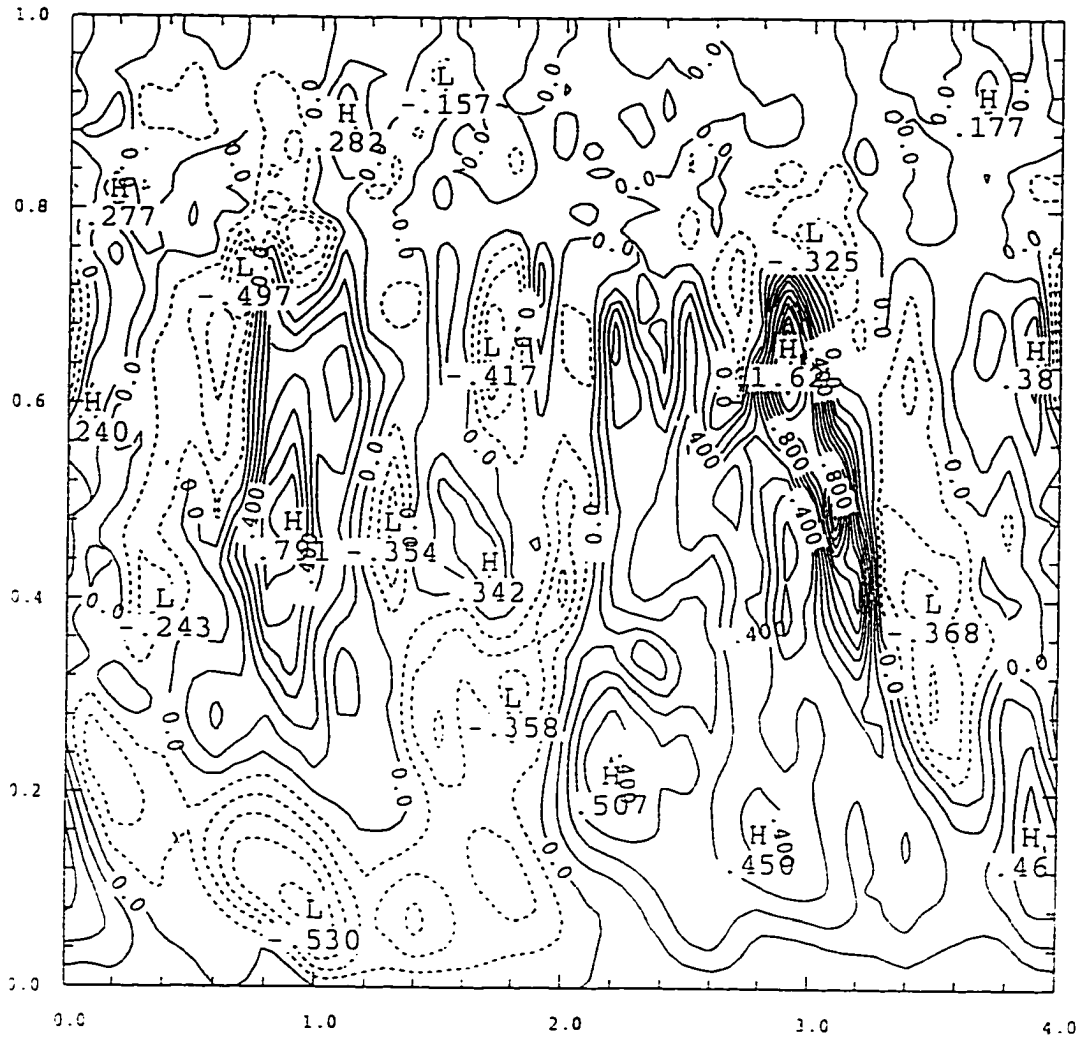


Figure 4.6. Vertical cross sections along the ship track ( $x=1.2$  km) for simulation A348: (a) vertical velocity field, (b) passive scalar field at 30 minutes after injection.

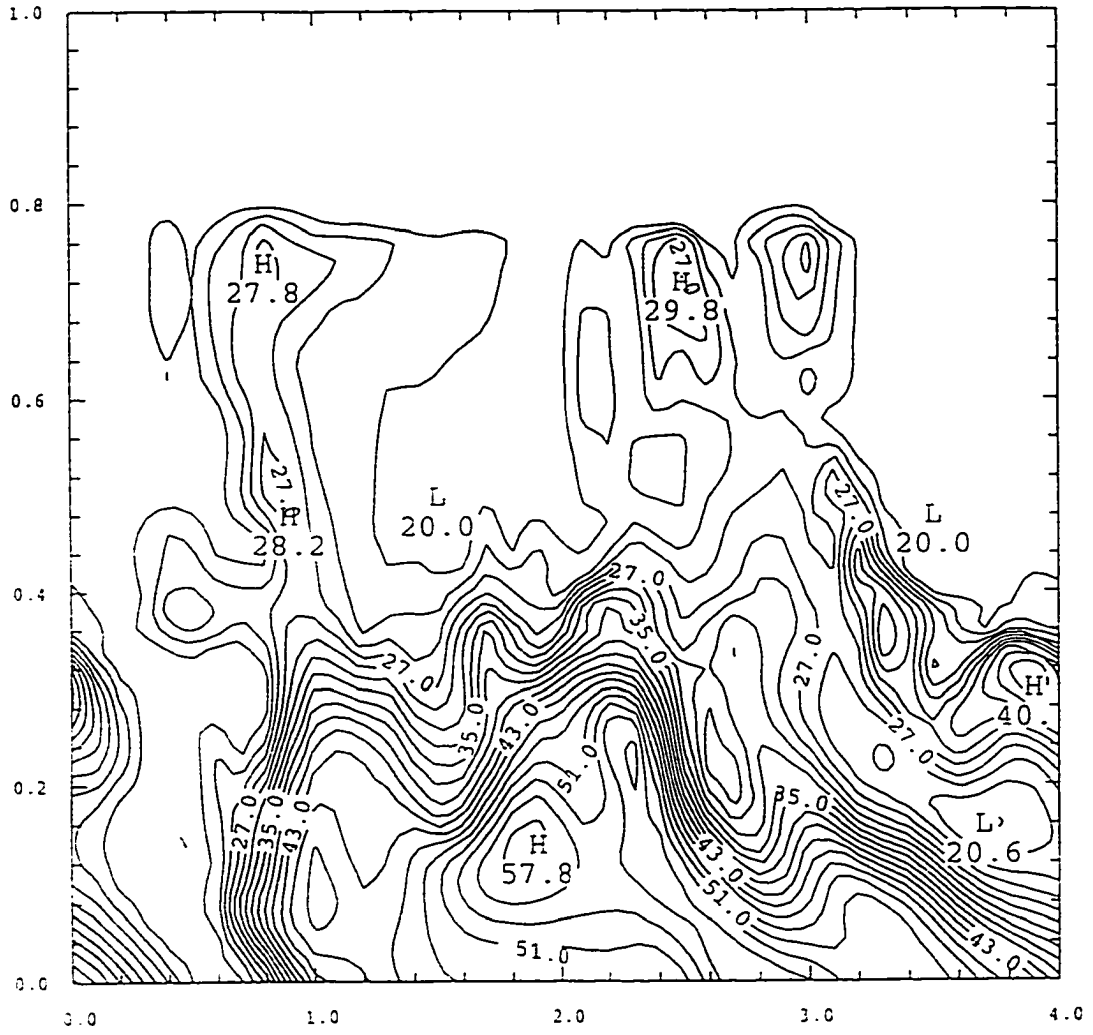


Figure 4.6. (continue)

transport of the admixture through the stable transition layer depends on many external parameters, such as the sea-surface heat and moisture fluxes, cloud top radiative cooling or warming, the stability of the transition layer, etc. For instance, in A348 simulation, the surface heat flux is fixed, therefore heat is continuously added to the lower half of the boundary layer, causing the temperature to increase with time. The stable transition layer will be eventually disrupted. As the simulation proceeds forward, more plumes will form due to the decreased stability of the inversion layer. However, if the surface temperature instead of the heat flux is kept constant, the results will be different. The stable transition layer may or may not disrupt depending on the relation between the surface potential temperature and the mean potential temperature below and above the transition layer. If the surface potential temperature is larger than the potential temperature in the upper half of the boundary layer, the situation will be similar to that of the constant heat flux. On the other hand, If the surface potential temperature is larger than that in the lower half of the boundary layer, but smaller than that in the upper half, the boundary layer may reach a quasi-steady state of vanishing surface heat flux, but still maintain a somewhat weakened stable transition layer. Some other effects of the boundary layer parameters are discussed in the subsections below.

#### b) Effects of buoyancy

According to Lamb (1982), buoyancy has two basic effects on the released material in convective boundary layer: 1) a slight upward displacement of the effective release point --- this is probably due mostly to the momentum of the emissions; 2) a slight increase of the effective vertical velocity. The magnitude of the upward displacement (effective vertical velocity increase) is directly proportional to the momentum flux (buoyancy flux). The simulation of A334 (Fig. 4.3) shows that

the passive scalar becomes well mixed in less than 30 minutes. The additional heat (buoyancy) in this case may slightly accelerate the vertical advection of the passive scalar and the ship track may form earlier. However, the effects of buoyancy are more significant in the decoupled boundary layer. Fig. 4.7 shows the time evolution of the horizontally averaged boundary layer parameters from a simulation of A348 with buoyancy ( $\Delta T=0.1$  °C) added to the ship track (hereafter denoted as A348B). The temperature increment of  $\Delta T=0.1$  °C is chosen based on the estimate of the heat energy added to the atmosphere by the ship engine Hanjin Barcelona (Innis et al., 1996). The comparison between Fig. 4.7 and Fig. 4.2 shows no significant differences between the vertical velocity variance  $(w')^2$ , TKE and LWC profiles in these two cases. However, the profile of the passive scalar demonstrates a significant increase of the released material in the cloud layer. Fig. 4.8a shows the vertical cross section of the vertical velocity averaged over the y-direction. A strong updraft line ( $x=1.0$  km) developed at the ship track location and a significant amount of the passive scalar has been transported into the cloud layer at 30 minutes (Fig. 4.8b). The large passive scalar transport is mainly due to the large eddies, which are particularly strong during the first 20 minutes. The stable transition layer inhibits the momentum mixing throughout the entire boundary layer depth. The ship track is, thus, slightly shifted in the upper half of the boundary layer compared to the lower half as a result of the differences in the horizontal velocities between these two layers.

c) Effects of solar radiation on boundary layer decoupling and ship track formation

Solar radiation plays an important role in the formation and maintenance of the boundary layer decoupling. Fig. 4.9 shows the time evolution of the horizontally

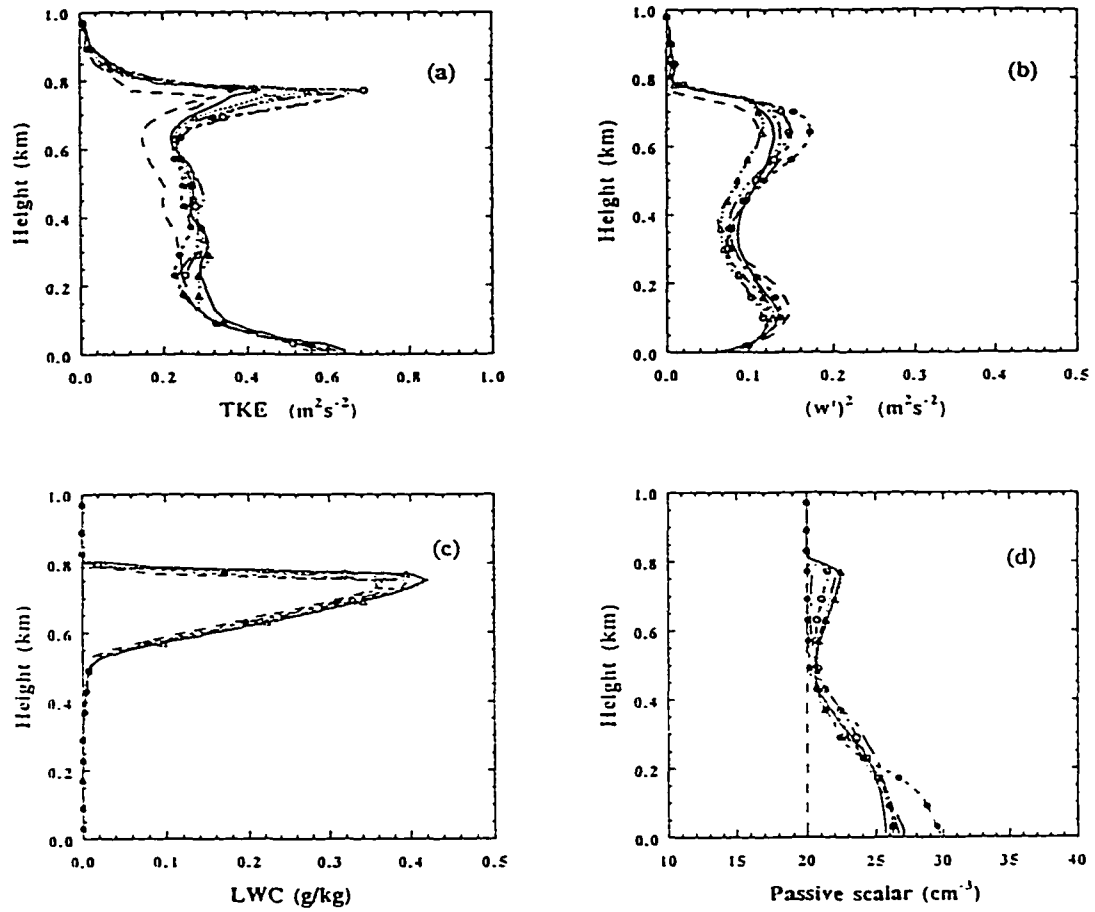


Figure 4.7. Time evolution of horizontally averaged parameters (TKE,  $(w')^2$ , LWC and passive scalar) in simulation A348B. The model results are shown at 7200 s, 7800 s, 8400 s, 9000 s, 9600 s, 10200 s and 10800 s (see Fig. 4.3d for line notation).

A348B

WVEL

Y= 0.00

9000.

a

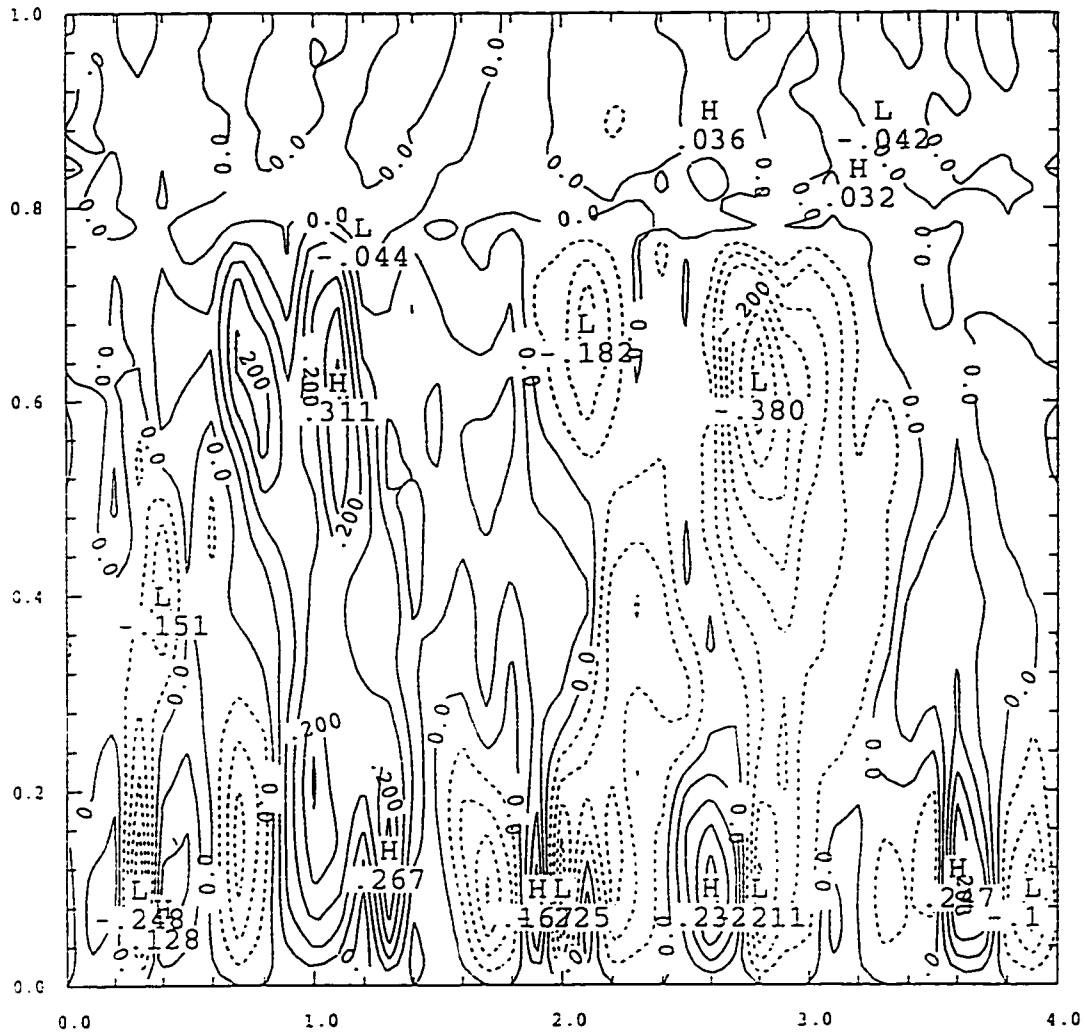


Figure 4.8. Vertical cross section for (a) vertical velocity field, (b) passive scalar field Averaged over y-direction at 30 minutes after injection in simulation A348B.

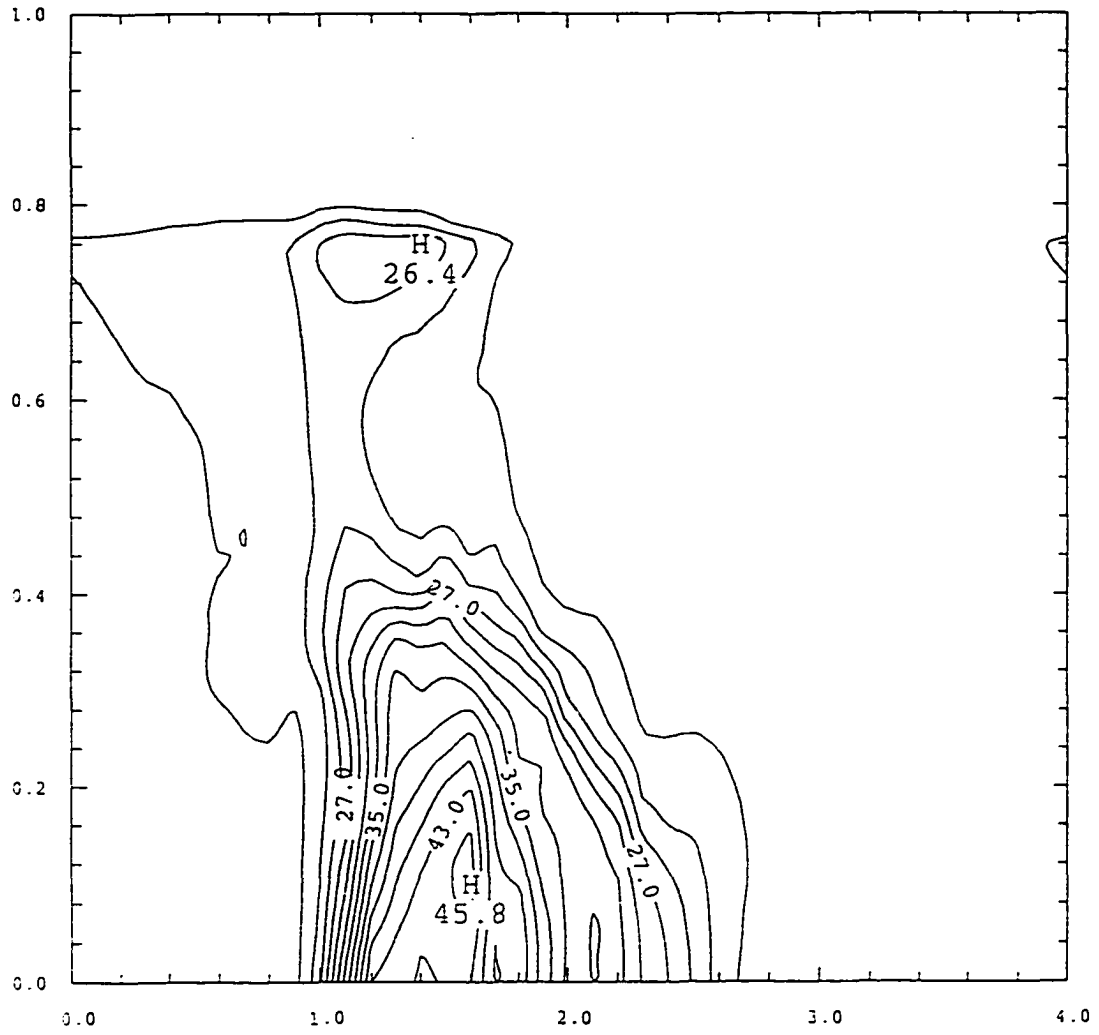


Figure 4.8. (continue)

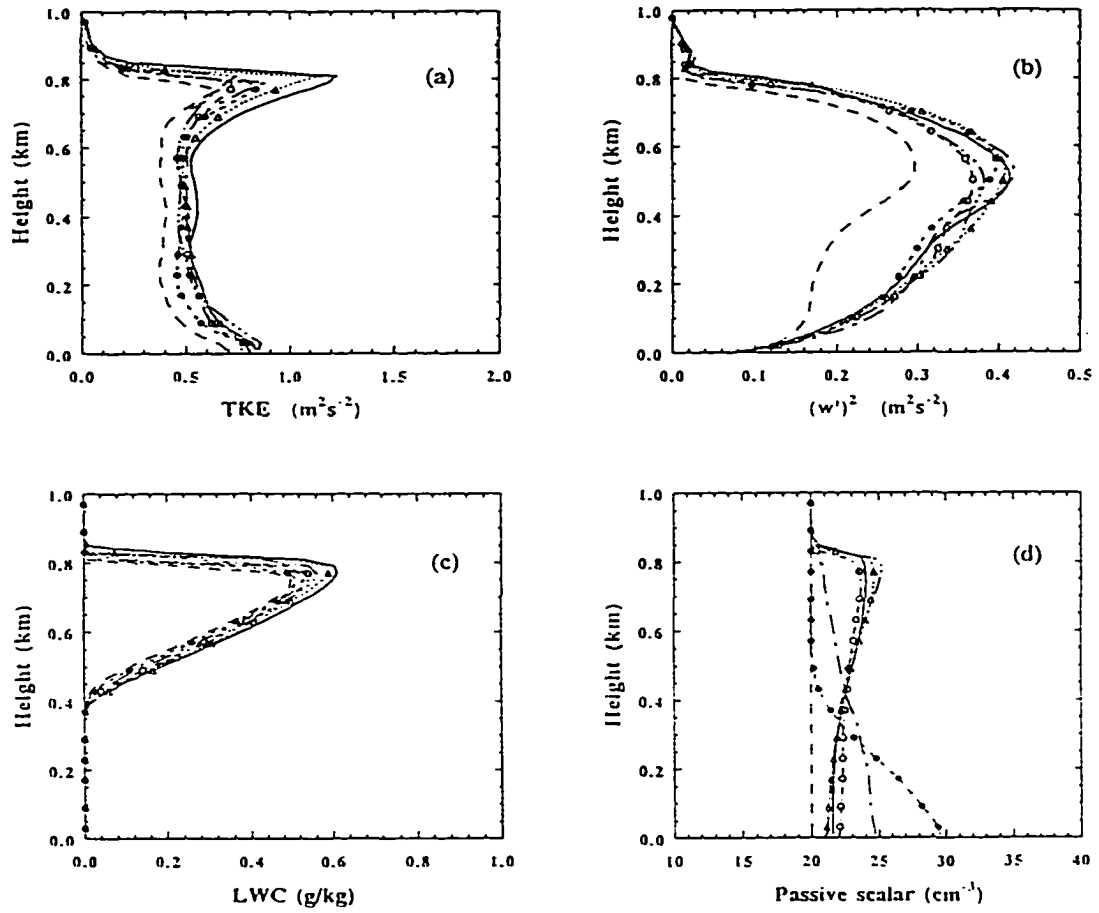


Figure 4.9. Same as in Figure 4.7 except for simulation A348N.



averaged boundary layer parameters for the simulation of the decoupled case A348, but with solar radiation turned off (hereafter denoted as A348N). In the absence of solar heating, the boundary layer becomes well mixed as demonstrated by a single maximum in the  $(w')^2$  profile. The long wave radiative cooling near the cloud top increases the instability of the boundary layer and results in the development of a strong convection. The vertical advection of the passive scalar, as demonstrated by the Fig. 4.9d, is similar to the well-mixed case A334. Diurnal variation of solar radiation and consequent changes in the boundary layer stability may be, thus, an important factor in the ship track formation. We hypothesize that ship track formation, all other conditions equal, may be facilitated during the morning and evening hours when the effects of solar heating are minimal.

#### d) Effects of the stability of the transition layer

In order to study the effects of the stability of the transition layer, we conducted a separate experiment in which the temperature in the lower half of the boundary layer was reduced by  $0.25\text{ }^{\circ}\text{C}$  (Fig. 4.2, dashed line), thus, increasing the stability of the transition layer. Other initial conditions were the same as in A348B simulation. Fig. 4.10 shows the time evolution of the horizontally averaged parameters for this case (denoted as A348B1). By comparing with Fig. 4.4, we see no significant difference in the  $(w')^2$  and LWC profiles. However, the vertical transport of momentum and the passive scalar is significantly reduced, as only the most intense plumes can now penetrate the stable transition layer and reach the cloud top.

A summary plot for the simulations of the decoupled boundary layer cases is given in Fig. 4.11, which shows the total amount of the passive scalar accumulated above the 500 m level. The amount of the material advected into the cloud layer in the decoupled case depends on such boundary layer parameters as surface heat flux,

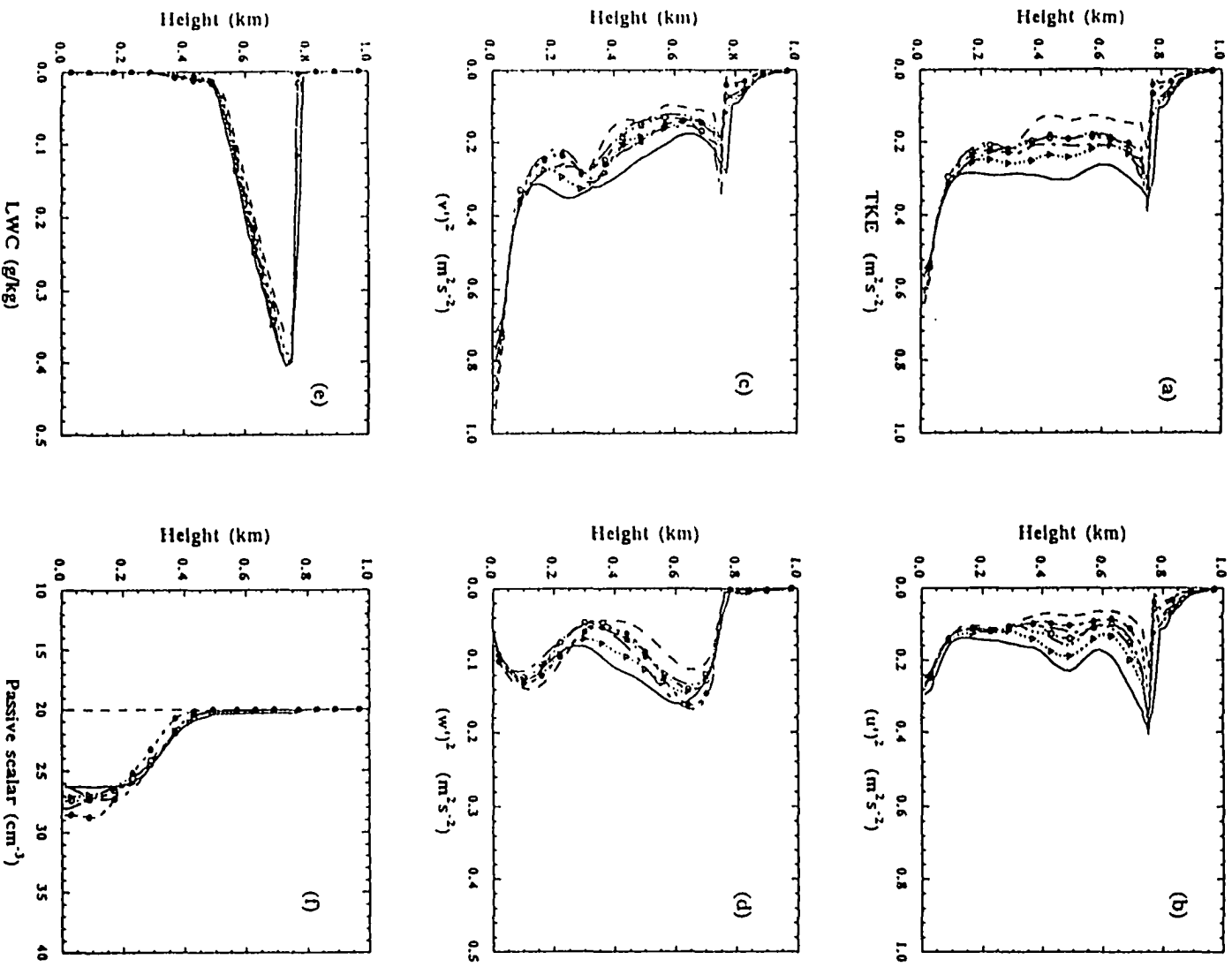


Figure 4.10. Same as in Figure 4.3 except for simulation A348B1.

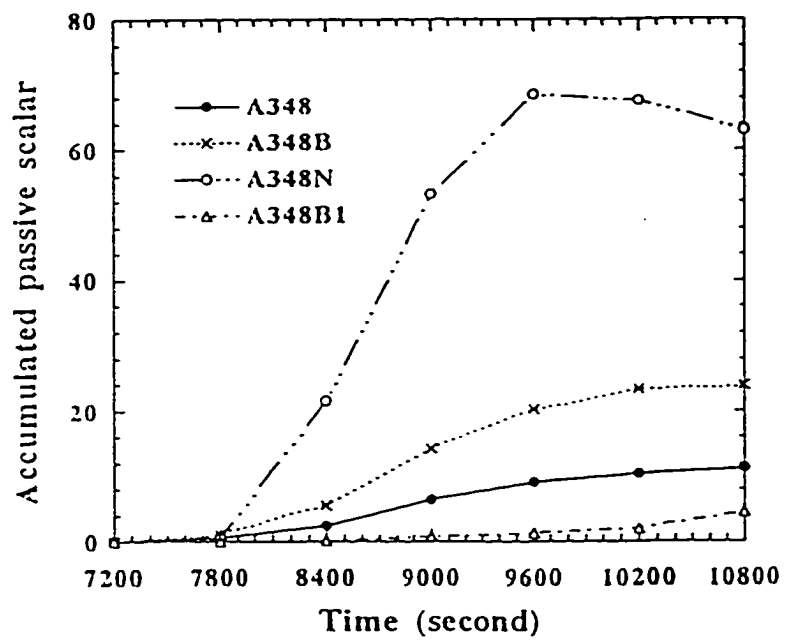


Figure 4.11. Total amount of the passive scalar accumulated above 0.5 km for the simulations A348, A348B, A348N and A348B1.

relative stability of the transition layer, and the intensity of solar radiation which, in turn, depends on the time of the day. From Fig. 4.11 we see that even a mildly stable transition layer can significantly reduce the vertical advection of the passive scalar. A relatively small  $0.1\text{ }^{\circ}\text{C}$  temperature addition to the ship track doubles the amount of material reaching the cloud layer in our A348 simulation. Diurnal variations of the solar radiation may significantly affect the boundary layer stability and thus the possibility of the ship track formation in the decoupled boundary layer.

### **4.3 Microphysical properties of the ship track**

The microphysical effects related to ship tracks have been investigated in a series of 2-D simulations using the explicit microphysical version of the CIMMS LES model. The integration domain is  $10\text{ km} \times 0.8\text{ km}$ , with grid sizes  $\Delta x=100\text{ m}$  and  $\Delta z=20\text{ m}$  used in all simulations. The simulations were initialized using the sounding taken during A334 flight. The ship track probed during this flight was produced by the ship Hyundai Duke which is clearly seen on the satellite image in Fig. 4.12. The ship track manifest itself as a bright line of clouds going from southwest to northeast corners of the satellite image. The ship trail is more concentrated and the cloud is brighter during the first hour after release, however, it is more diluted and zigzagged after that. The meandering of the ship trail after one hour shows that mesoscale circulations play an important role in the ship track later development.

In order to evaluate the effects related to the 2-D dynamical framework, we first perform a 2-D control run (denoted as A334-2D) in which all parameters are the same as those in the 3-D A334 case. Fig. 4.13 shows the time evolution of the horizontally averaged parameters for the case A334-2D. The TKE and its three components are significantly larger in 2-D compared to their counterparts in 3-D (Fig. 4.3). The

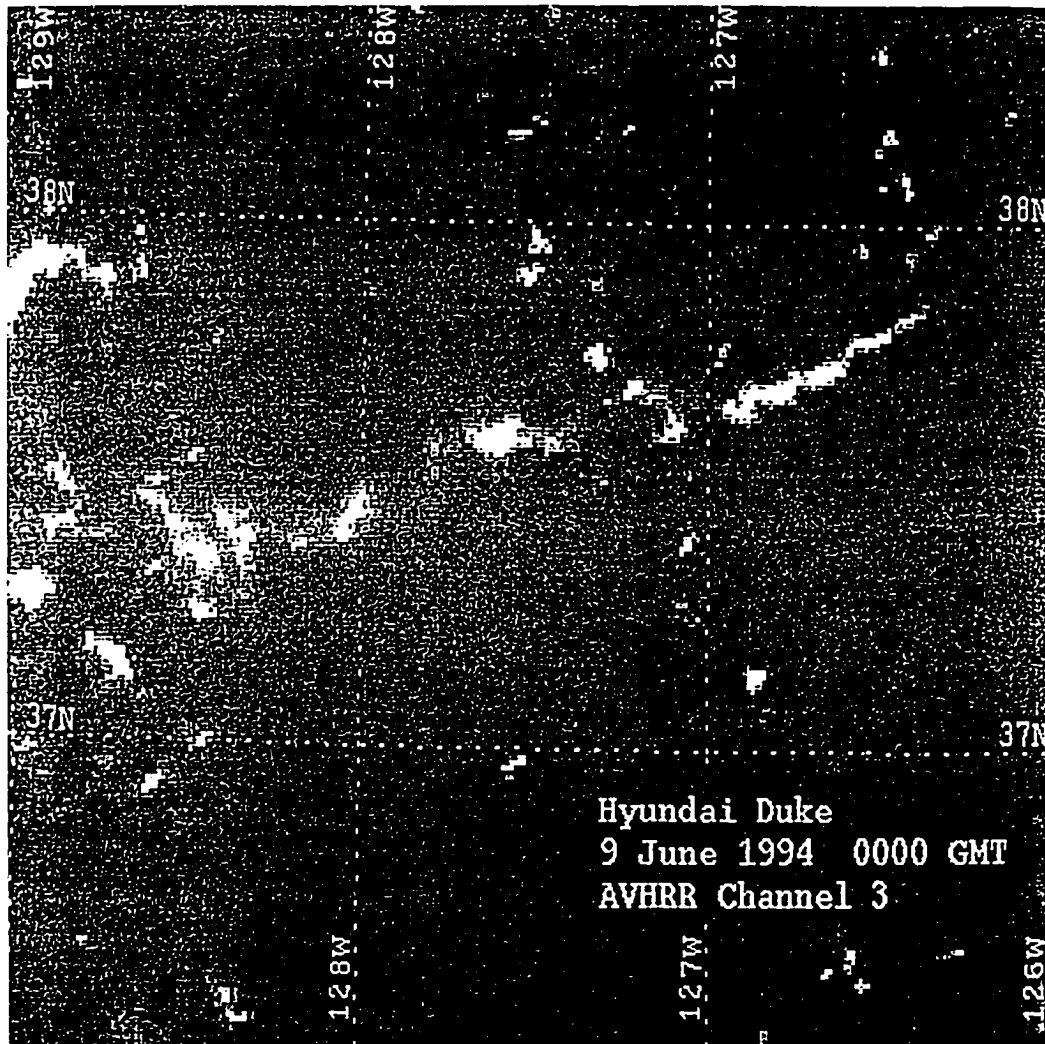


Figure 4.12. Satellite image at 0000 UTC on June 9, 1994. The ship track, which is produced by the ship Hyundai Duke, manifest itself as a bright line of clouds going from southwest to northeast corners of the satellite image.

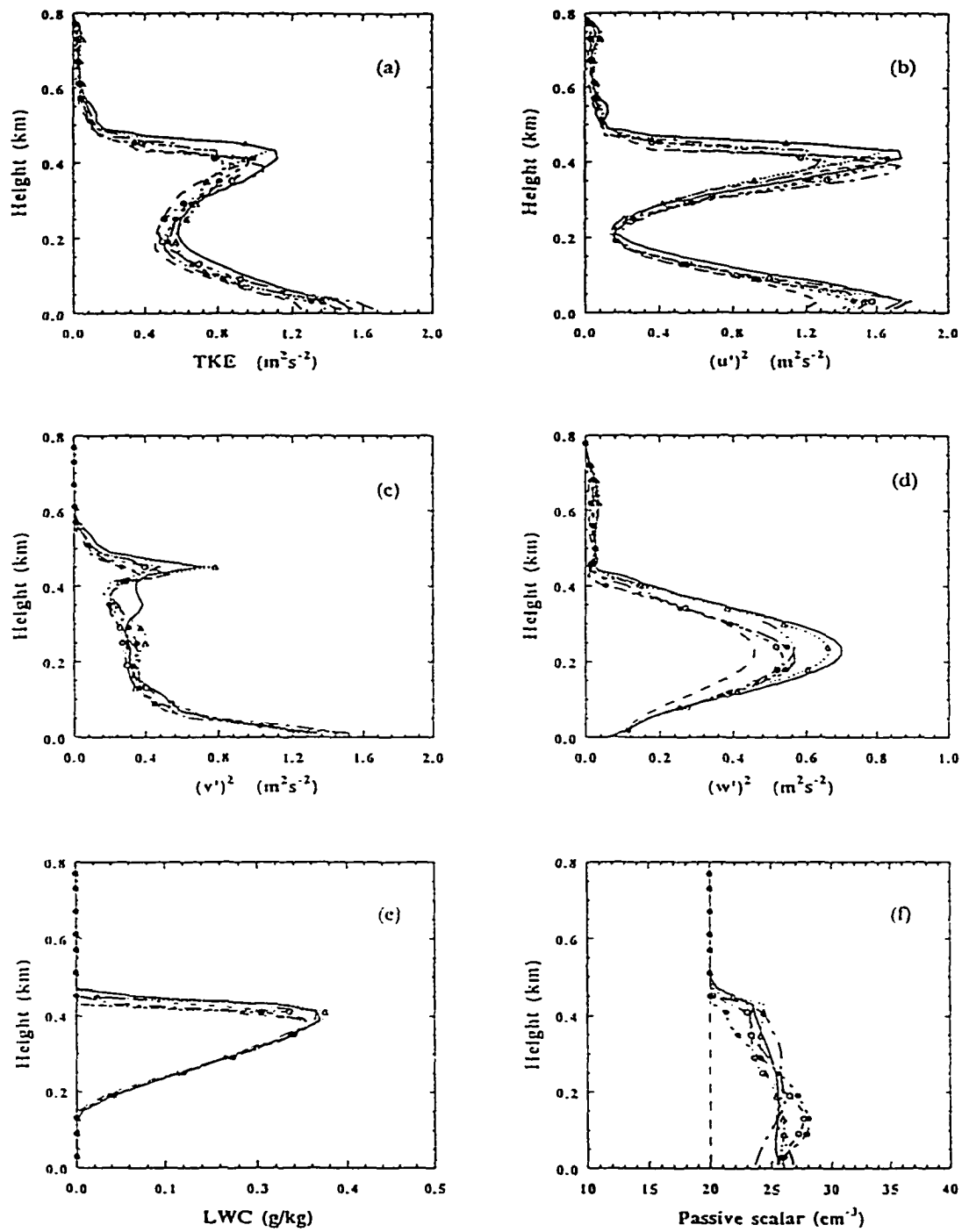


Figure 4.13. Same as in Figure 4.3 except for simulation A334-2D.

LWC is slightly increased due to the slightly higher cloud top. The passive scalar is not so well mixed in the 2-D case as it is in the 3-D simulation. The ship track width, which is defined here as the width between positions at which the released material falls to one-tenth of the peak value (Pasquill and Smith, 1983), is narrower in A334-2D simulation than is that in 3-D. Fig. 4.14 shows ship track width of model results and the estimates from satellite image. The ship-relative wind is  $V=13.0$  m/s in this case, and the observations are estimate as the ship track width at a distance  $d=V*t$  ( $t$  is time) down track of the ship. There is a good agreement between the observations and the 3-D results. The 3-D ship track width shows significant increase in the first 10 minutes which is most likely caused by the spreading of the ship effluent in the sinking branch of the large eddy circulations near the surface. Although there are noticeable quantitative differences between the 2-D and 3-D simulations, we expect that the qualitative conclusions from the 2-D simulations to be similar to those drawn from the much more expensive 3-D simulations. We would like to emphasize that the performed simulations were not intended to be case studies and, therefore, no special efforts have been made to exactly match the observations. The primary goals were to understand the physical mechanisms affecting the ship track formation, specifically, we will discuss the effects of drizzle suppression and the effects of the ship track on drop spectrum, LWC and radiative properties of the cloud layer.

a) Effect of background aerosol concentration

We will describe two simulations (A334P and A334C) made in environments that differ in the ambient CCN concentration. The initial aerosol spectrum of the background cloud in the case A334P was taken according to the A334 observation and had a total CCN concentration of  $161.7 \text{ cm}^{-3}$ . The instantaneously injected aerosol which emulated the ship plume is assumed to have a spectrum similar to that

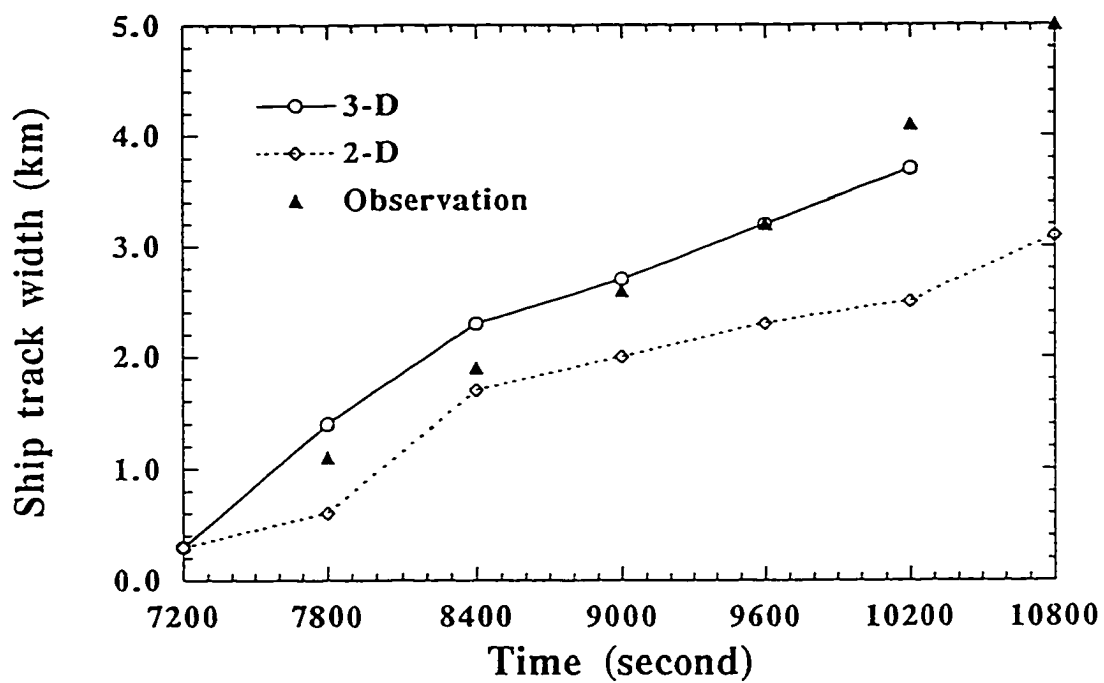


Figure 4.14. Time evolution of the ship track width in A334. Triangles show the estimate from satellite image, solid line with circles shows the estimate from 3-D (A334) simulation, dotted line with diamonds shows the estimate from 2-D (A334-2D) simulation.



of the background aerosol, but with an enhanced concentration of  $30,000 \text{ cm}^{-3}$ . The aerosol was injected along the horizontal rectangular cylinder located at  $x=0.3, 0.4, 0.5 \text{ km}$  and  $z=50, 70, 90 \text{ m}$ . Fig. 4.15 (lower panel) shows the cloud drop concentration isolines and the vertically averaged parameters of the cloud layer (upper panel) one hour after injection. Similar to the liquid water path (LWP) (defined as an integration of  $q_l$  along a vertical column), we also define the drizzle path (DP) as an integration of drizzle water along a vertical column. Following Gerber (1994) we define drizzle as liquid water in drops with radius  $> 20 \mu\text{m}$ . It is evident that a large number of CCN are activated in the ship track region ( $x \approx 3.0\text{-}6.5 \text{ km}$ ). The maximum cloud drop concentration in the ship track reaches  $350 \text{ cm}^{-3}$  near cloud top. The LWP is significantly larger than the drizzle path (DP) (notice the different scale for the LWP and the DP) which means that fewer drops grow larger than  $20 \mu\text{m}$  in radius. The drizzle is very small both inside and outside the ship track in this case. The drizzle paths inside the ship track in A334P and the control run A334P-2D (where no ship aerosol has been injected) differ insignificantly, which means that ship track has little effect on drizzle suppression in this case.

Fig. 4.16 shows the cloud drop concentration, LWC, and effective radius along a horizontal line at  $z=0.31 \text{ km}$  across the ship track for A334P and the control run A334P-2D. The background cloud drop concentration is  $50\text{-}70 \text{ cm}^{-3}$ , whereas the drop concentration is around  $150\text{-}200 \text{ cm}^{-3}$  inside the ship track. The effective radius is reduced from approximately  $8.5 \mu\text{m}$  to  $6.0 \mu\text{m}$ . LWC is roughly unchanged inside the ship track compared to that of the control run (Fig. 4.16b).

For the clean air experiment (A334C) we specify the ambient CCN spectrum similar to A334P, but with reduced total CCN concentration of about  $32 \text{ cm}^{-3}$ . The ship aerosol is injected in the same way as in the previous run. Fig. 4.17 shows the

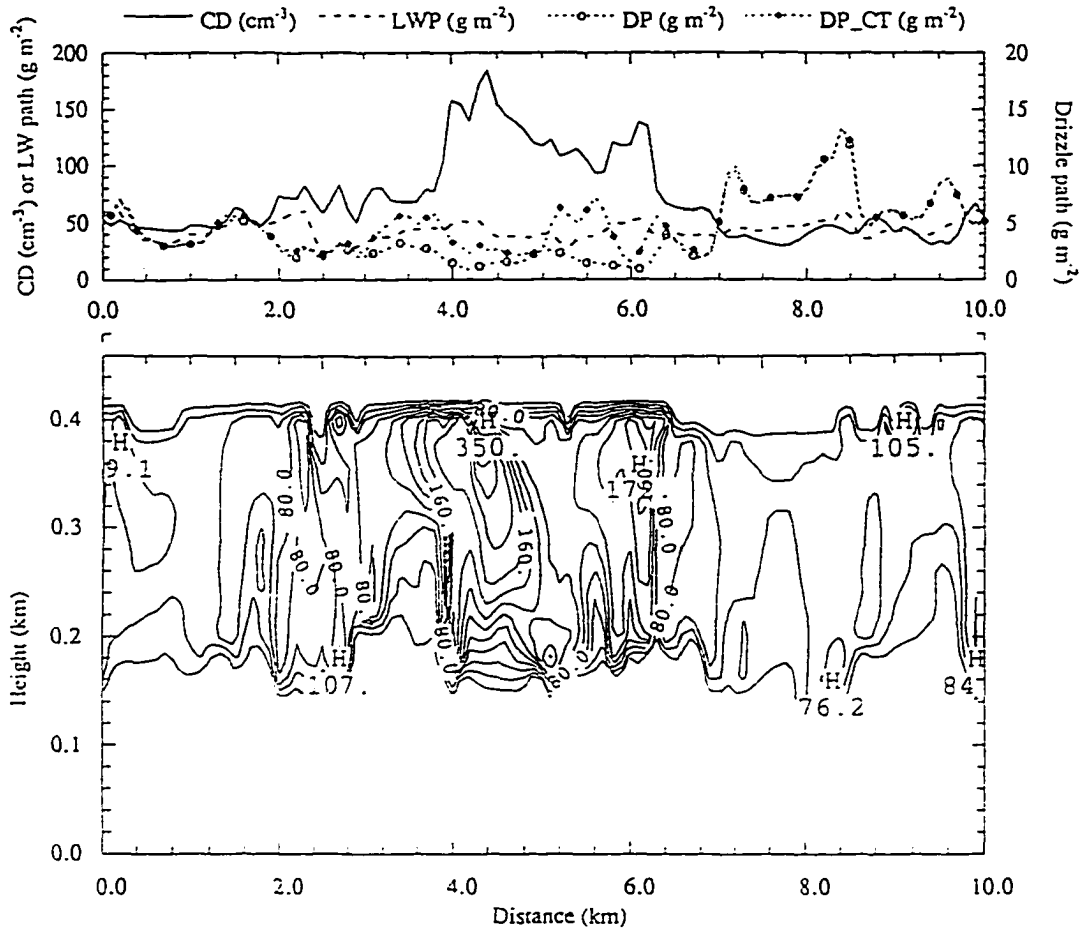


Figure 4.15. Cloud drop concentration field (lower panel) and vertical averaged parameters (upper panel) of the cloud layer in simulation A334P at 1.0 hour after injection. In the upper panel: solid line denotes the column averaged cloud drop concentration, dashed line denotes the liquid water path (LWP), dotted line with circles represents drizzle path (DP), and the dotted line with diamonds represents the drizzle path in the control run (DP\_CT).

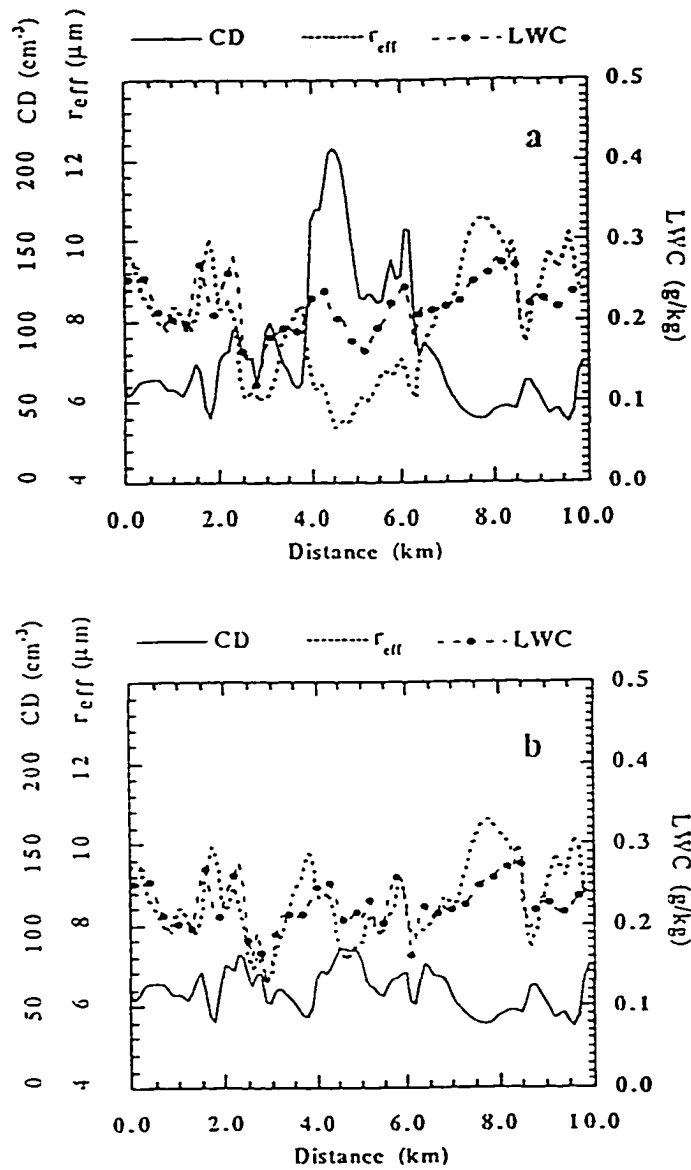


Figure 4.16. Cloud drop concentration, LWC and effective radius along the horizontal line  $z=0.31$  km in simulation A334P (panel a) and its associated control run (panel b) at 9000 s (30 minutes after injection).

A334C                      CNCD                      Y= 0.00                      10800.

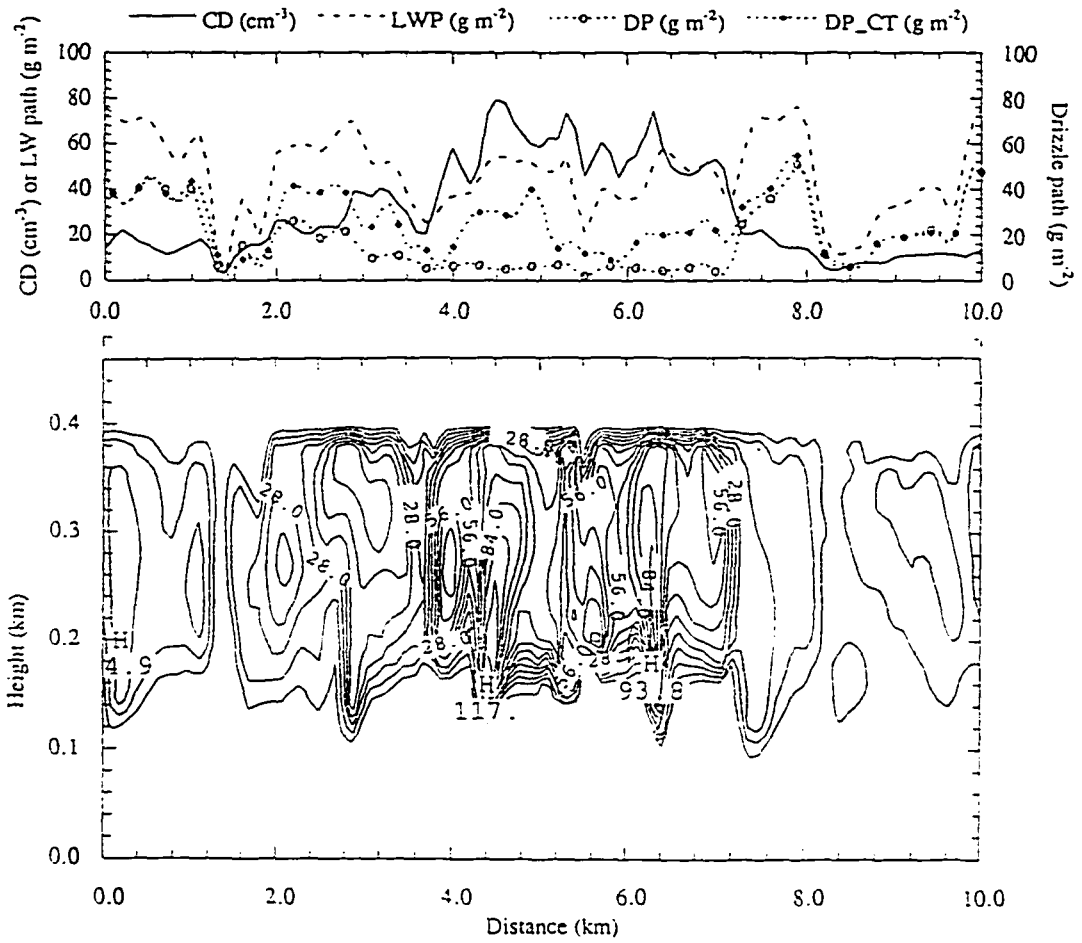


Figure 4.17. Same as in Figure 4.15 except for simulation A334C.

cloud drop concentration (lower panel) and some vertically averaged parameters of the cloud layer (upper panel) one hour after the ship aerosols have been injected. The ship track at this time is spread over the domain from about  $x \approx 2.0$  km to  $x \approx 7.2$  km. The comparison of the drizzle path between A334C and its control run (Fig. 4.17, upper panel) clearly shows that the drizzle was suppressed inside the ship track.

Ship track significantly affects cloud microstructure and radiative parameters. Figure 4.18 shows cloud drop spectrum for the simulation A334C in the domain 6.0–10 km which covers the transition region from the ship track cloud to the "uncontaminated" background cloud. The ship track roughly covers the region from 6.0 to 7.2 km in this plot. The ship track drop spectra are relatively narrow and are composed mostly of small drops, whereas the drop spectra outside the ship track clearly show bimodal distributions. Even though the LWP is high inside the ship track, the DP is significantly lower compared to the background cloud. The albedo which is estimated here as  $\tau/(\tau+6.7)$  (where  $\tau$  is the cloud optical depth) clearly shows a substantial increase inside the ship track.

#### b) Effect of ship track on LWC and drizzle suppression

Aircraft observations show conflicting evidence on the effect of ship track on LWC. Ferek et al. (1997) show LWC increases in some cases while decreases in the others. The LWC inside the ship track increases by as much as 90% in the Star Livorno case (June 29, 1994), whereas it is decreased by as much as 25% in the Moku Pahu case (June 12, 1994). Measurements off the coast of southern California on July 10, 1987 by King et al. (1995) show LWC inside the ship track increases by about 20-60%, while measurements on June 8, 1994 in the same area during MAST experiment (Johnson et al. 1995) show that LWC inside the ship track decreases by about 40%.

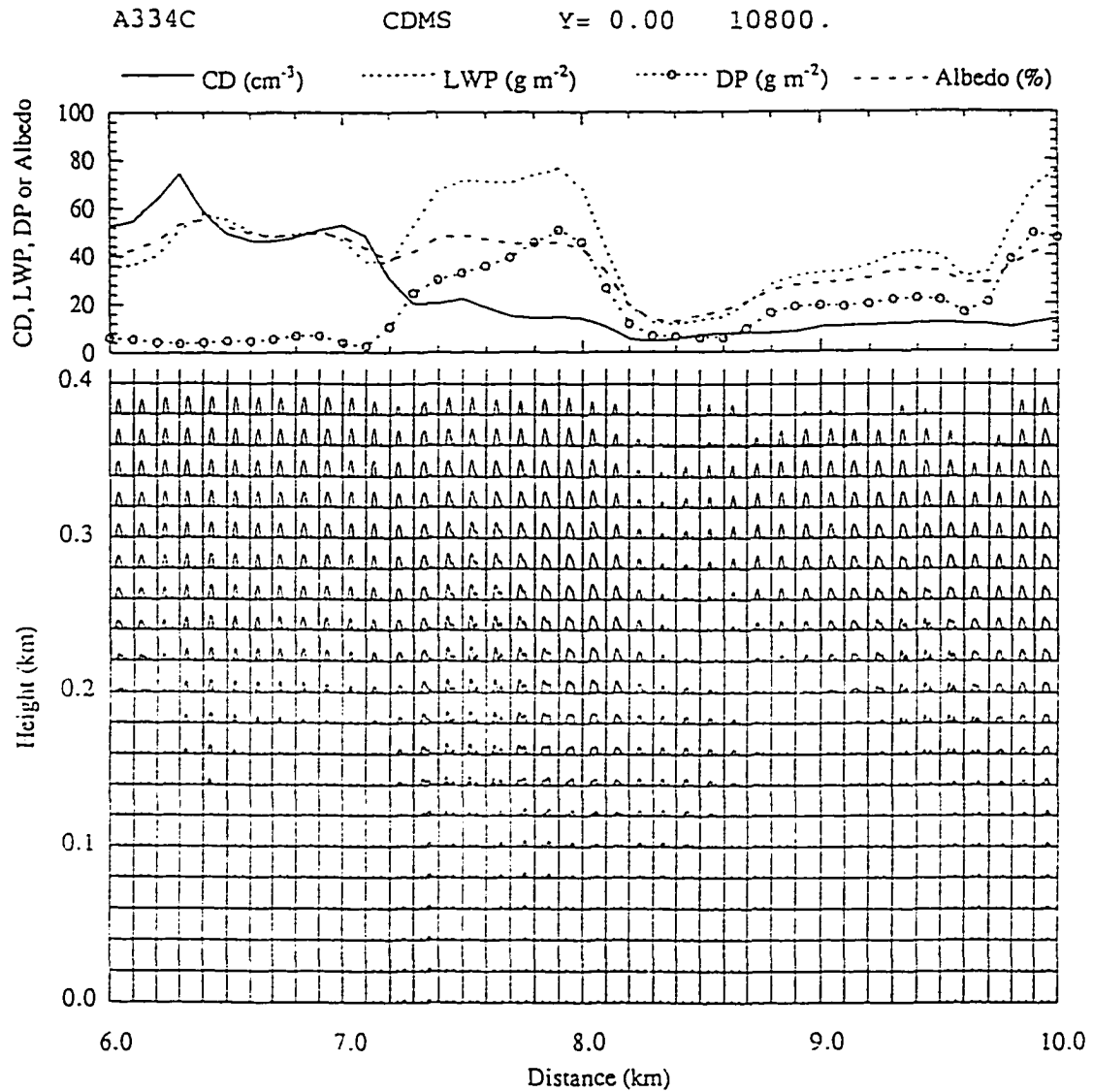


Figure 4.18. Cloud drop spectrum (lower panel) and vertical averaged parameters of the cloud layer in the region 6.0-10 km in simulation A334C. In the upper panel: solid line denotes the column averaged cloud drop concentration, dotted line denotes the liquid water path (LWP), dotted line with circles represents the drizzle path (DP), and the dashed line represents albedo.

In order to better understand the ship track effect on LWC, we show in Fig. 4.19 the cloud drop concentration, LWC, and effective radius along a horizontal line at  $z=0.31$  km for the A334C simulation and for the control run A334C-2D. The background cloud drop concentration is around  $20 \text{ cm}^{-3}$ , while the cloud drop concentration in the ship track is around  $70 \text{ cm}^{-3}$ . The effective radius is also affected and is significantly reduced inside the ship track from roughly  $13 \mu\text{m}$  to  $8 \mu\text{m}$ . The LWC at the  $z=0.31$  km level is slightly lower in the ship track than in the surroundings. This is the result of rather developed drizzle in background clouds outside the ship track. The drizzle in the background clouds results in the redistribution of LWC inside the cloud layer, namely, the higher LWC from the upper level precipitates downward outside the ship track.

The effect of ambient aerosol concentration on the LWC inside ship track is also demonstrated in Fig. 4.15, which shows that LWC is roughly unchanged inside the ship track compared to the LWC outside the ship track. In this simulation, the cloud drop concentration is relatively high outside the ship track and no significant drizzle is produced inside or outside the ship track. Therefore no redistribution of the LWC occurs in this case.

The above examples show mainly the effect of microphysical environment on LWC inside the ship track. In the clear air mass the background clouds easily produce drizzle, and redistribute LWC resulting in non-adiabatic LWC profiles. In more polluted ship tracks the drizzle formulation, however, is suppressed and LWC mostly shows adiabatic increase with height.

The LWC inside the ship track may also be affected by the heat and moisture injected into the cloud layer by the ship engine exhaust. Figure 4.20 shows the cloud drop concentration, total LWC and 2D-C LWC (drizzle) from A348P along a line

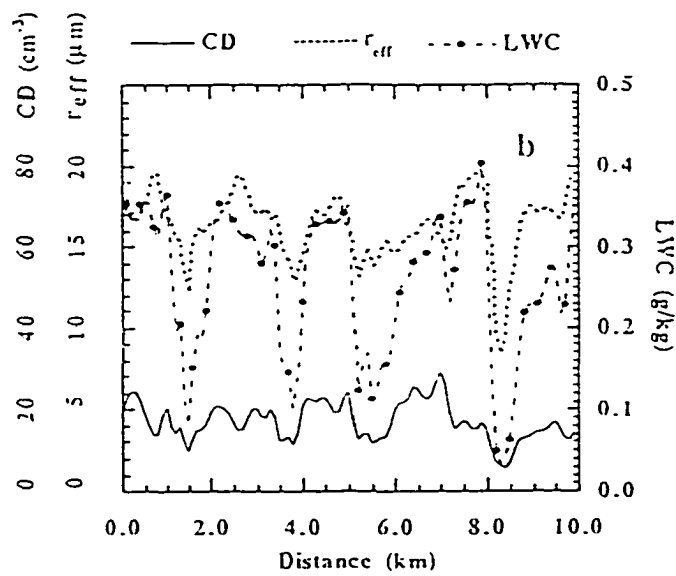
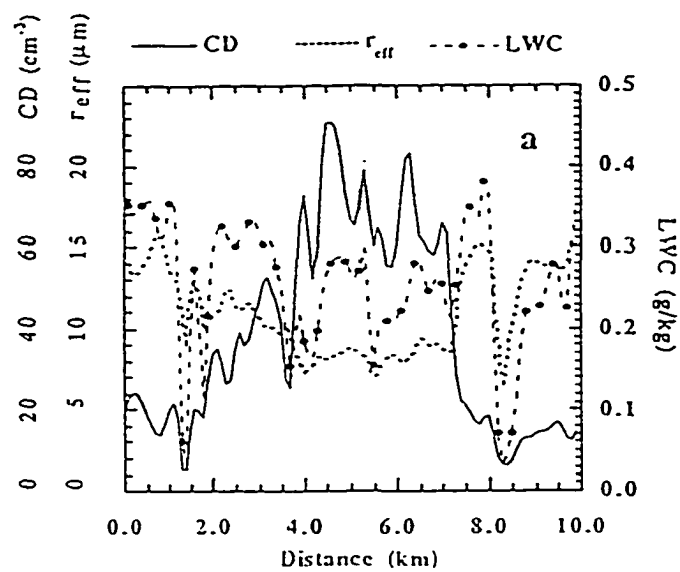


Figure 4.19. Same as in Figure 16 except for simulation A334C.



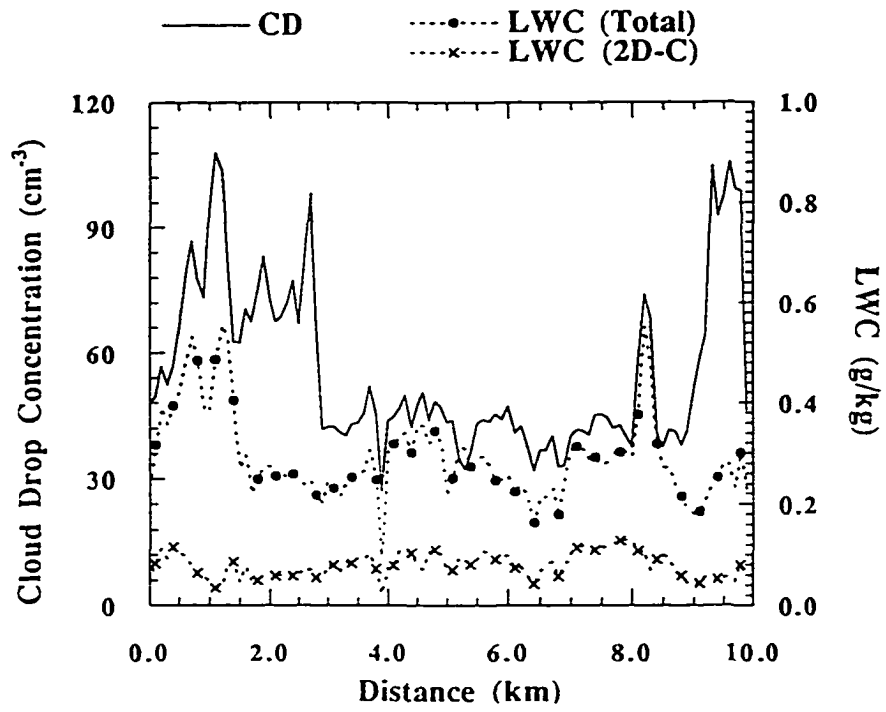


Figure 4.20. Cloud drop concentration, total LWC and 2D-C LWC along the line ( $z=0.68$  km) in simulation A348P at 1 hour after injection.

across the ship track at  $z=0.68$  km (see also Fig 4.9a, b). The line crosses a strong plume, located near  $x=1.0$  km, which transports a significant amount of water vapor and material into the cloud layer. The plot clearly shows the LWC increase inside the ship track. The drizzle was not suppressed due to the high LWC. The boundary layer is not so well mixed in this decoupled case and the air near the sea surface has more moisture compared to the upper level air, therefore, plumes carry more water vapor into the cloud layer causing the LWC increase. This result is clearly due to the increased buoyancy of the ship track and boundary layer decoupling which causes the accumulation of moisture near the surface.

We also find that ship track persistence depends on the microphysical properties of the background aerosol. In the clean case, the ship track lasts much longer than in the polluted environment. Figure 4.21 shows the vertically averaged concentrations of cloud drops (CD) and the sum of CCN and cloud drops (CCN+CD), as well as the vertical integration of  $w^2$  (KE-w), in the simulations of A334C (upper panel) and A334P (lower panel). Low CCN count outside the ship track in simulation A334C is favorable for strong coalescence and drizzle generation. Coalescence (and drizzle that reaches the ground) removes CCN from the boundary layer and helps maintain even lower CCN count. In regions of high CCN concentrations, the removal of aerosols by coalescence and drizzle is inhibited, which helps maintain high CCN concentrations. As a result, the contrast between microphysical properties inside and outside the ship track is increasing in the A334C simulation, whereas it is decreasing in the A334P simulation due to the diffusion of the ship effluent which is not counter balanced by the CCN coalescence removal as in the A334C case. It is worth noting that the drizzle effect has significantly reduced the vertical component of the kinetic energy (hence vertical advection) outside the ship track in the A334C simulation. The high CCN activation rate inside the ship track

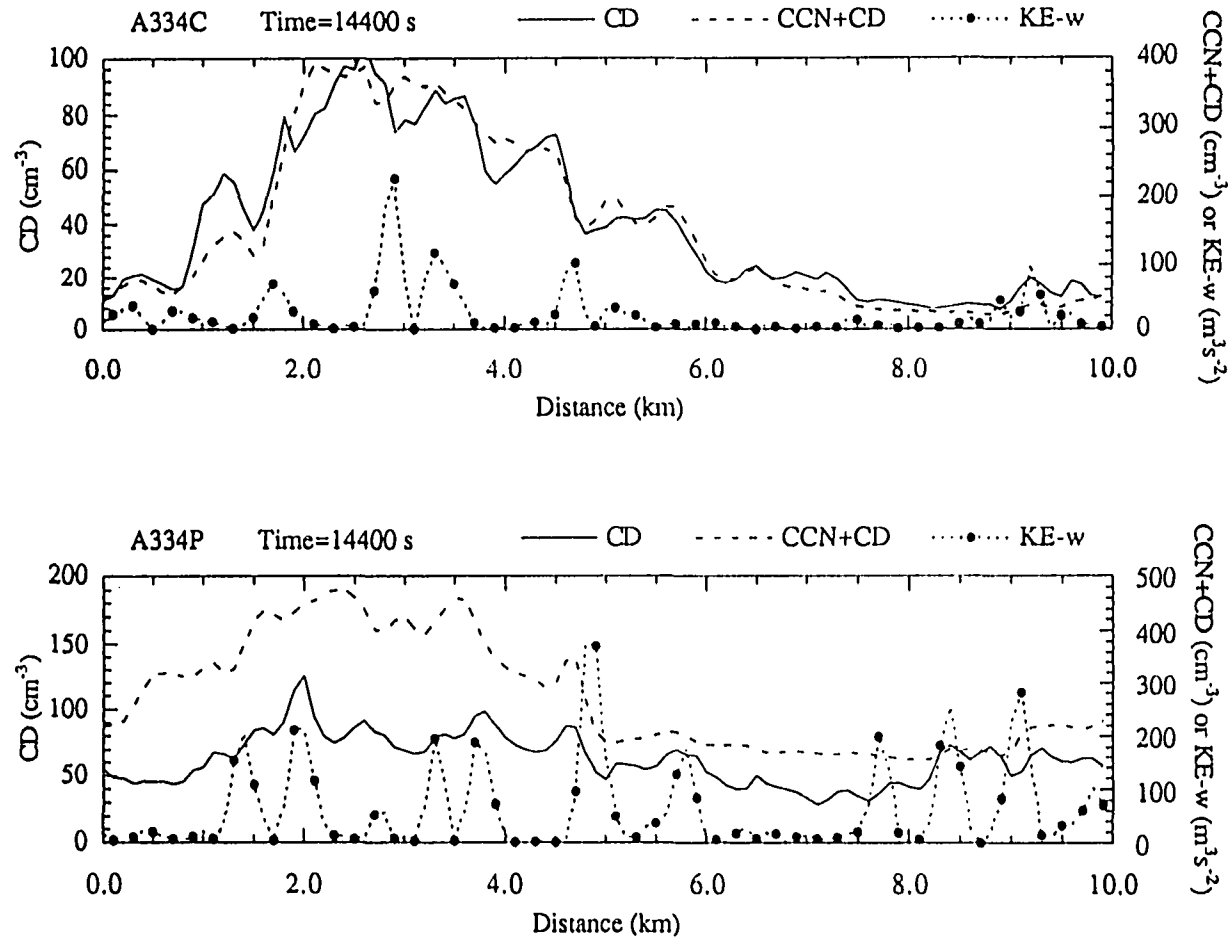


Figure 4.21. Vertically averaged concentrations of cloud drops (CD) and the sum of CCN and cloud drops (CCN+CD), as well as the vertical integration of  $w^2$  (KE-w), in the boundary layer from the simulations of A334C (upper panel) and A334P (lower panel).

(compared to Fig. 4.17) in A334C is probably due to the compensation effect, i.e. the increase of the vertical heat and moisture fluxes inside the ship track due to their decrease outside the ship track.

#### **4.4 Conclusions**

The LES model coupled with explicit microphysics has been applied for studying the ship track formation under various boundary layer macro and microphysical conditions. We have carried out experiments simulating ship track formation and the associated microphysical effects of the ship track produced by the ship Hyundai Duke on June 8, 1994 in the well mixed boundary layer and by the ship Hanjin Barcelona on June 29, 1994 in the decoupled boundary layer during Monterey Area Ship Track (MAST) experiment. We also simulated the effects of heat injected by the ship engine exhaust on the transport of ship effluents into the cloud layer. In addition, we made simulations in clean and relatively polluted air using the explicit microphysical version of the model. From our simulation results, we draw the following conclusions:

a) Ship effluents are very easily advected into the cloud layer in the well mixed convective boundary layer, whereas their transport may be suppressed by the stable transition layer in the decoupled case. With the help of buoyancy and possibly initial momentum of the ship effluents, however, the most intensive convective plumes in the decoupled boundary layer may penetrate the stable transition layer and transport significant amounts of the ship effluents into the cloud layer to form a ship track.

b) Changing the following parameters will increase the possibility of the ship track formation in the decoupled boundary layer

- adding more heat to the ship effluent

- decreasing the stability of the stable transition layer below cloud deck
- increasing the surface heat flux
- decreasing the amount of solar radiation

Increasing the surface heat flux and decreasing the amount of solar radiation will gradually decrease the stability of the stable transition layer.

c) Ship track may last longer in a clean marine boundary layer than in a polluted environment.

d) Our simulation results support the assumption of drizzle suppression in the clean environment.

e) LWC inside the ship track may be lower or higher than the LWC outside the ship track depending on the specific characteristics of the boundary layer, such as the mixed layer height, stability of the boundary layer, as well as the ambient CCN concentration.

## Chapter

# 5

## Study of aerosol processing in stratocumulus clouds

In simulating stratocumulus clouds, the aerosol budgets become important in the longer term, as the cloud drops evaporate and the solutes are recycled into aerosols that can serve again as CCN. The heterogeneous chemical reactions, which add nonvolatile solute to each cloud droplet, strongly depends on the salt content and pH of the droplet (Lowe et al. 1996). Since the aerosols have a significant influence on cloud microphysics and cloud radiative properties, it is necessary that aerosol processes be simulated with adequate accuracy. However, current cloud models do not track the evolution of soluble aerosols, at least not after they turn into droplets. This limitation is removed in the new version of the CIMMS LES model which

includes a two parameter spectrum depending on both the drop mass and the solute mass. Such formulation is now computationally feasible and is needed for an accurate treatment of the aerosol recycling process. The aerosol processing due to nucleation scavenging, cloud droplet collision-coalescence and drizzle removal processes will be studied through a series of experiments using the newly developed two parameter cloud drop spectrum model.

### 5.1 Two parameter cloud drop spectrum model

For the aerosol processing study, the microphysical formulation has been significantly modified by introducing a two-dimensional Drop and Salt Size Distribution (DSSD) function,  $f(m,n)$ , which allows to follow the salt (CCN) particle transformations as they are processed by cloud drops. The function  $f(m,n)$  represents drop mass distribution such that  $f(m,n)dmdn$  is the number of particles per unit volume of air in the drop mass range from  $m$  to  $m+dm$  and the salt mass range from  $n$  to  $n+dn$ . Let  $f_{ij}$  denote the DSSD function in the discrete form with the indices  $i$  and  $j$  referring to the drop and the CCN mass categories, respectively. The governing equation for the two parameter drop spectrum is (Houze, 1993):

$$\frac{\partial f_{ij}}{\partial t} + \frac{\partial}{\partial x_k}(u_k f_{ij}) = R_{ij} + D_{ij} + C_{ij} + S_{ij} + \frac{\partial}{\partial x_k}(K_m \frac{\partial f_{ij}}{\partial x_k}) \quad (5.1)$$

The changes in the concentration  $f_{ij}$  are the result of nucleation ( $R_{ij}$ ), vapor diffusion ( $D_{ij}$ ), collection ( $C_{ij}$ ), sedimentation ( $S_{ij}$ ) and turbulent diffusion.

For the collection term ( $C_{ij}$ ), I assume that the collection kernel depends only on the cloud drop mass, and the nuclei are coalesced whenever two parent drops coalesce. The cloud droplet mass  $m$  and the nuclear mass  $n$  of the newly formed drop

are determined by adding the  $m$ 's and  $n$ 's of the coalescing drops, respectively. Therefore, the stochastic collection equation can be written as,

$$C_{ij} = \frac{1}{2} \int_0^{m_i} \int_0^{n_j} W(m_i - m', m') f(m_i - m', n_j - n') f(m', n') dn' dm' - \int_0^{\infty} \int_0^{\infty} W(m_i, m') f(m_i, n_j) f(m', n') dn' dm' \quad (5.2)$$

where  $W(m, m')$  is the collection kernel defined in Kogan (1991).

In addition to drop particle spectra, I also predict aerosol particle spectra,  $g(x, y, z, n, t)$ , as described in section 2.2. The governing equation is the same as equation (2.8) except that the nucleation term and evaporation term become  $\sum_i R_{ij}$  and  $\sum_i E_{ij}$ , respectively.

## 5.2 Coalescence calculations and the model accuracy tests

In this section, I will briefly describe the computational method for the solution of stochastic collection equation for the 2-D drop spectrum (Eq. 5.2).

The stochastic collection equation has two terms: the first term represents the drop number increase due to the coalescence between all pairs of drops whose mass summed to  $m(i)$ , while the second term represents the drop number decrease due to coalescence of the drops with mass  $m(i)$  with all other drops.

The first term in Eq. 5.2 gives the gain in the number of drops with drop mass  $m(i)$  and salt mass  $n(j)$ . It is calculated as a sum of binary collections between drops: one with drop mass  $m(k)$  and salt mass  $n(l)$  and another with drop mass  $m(i)-m(k)$  and salt mass  $n(j)-n(l)$ . Drop concentrations for the first drop with drop mass  $m(k)$



and salt mass  $n(l)$  are known, while drop concentrations for the second drop with drop mass  $m(i)-m(k)$  and salt mass  $n(j)-n(l)$  need to be interpolated as its mass coordinates are not necessary located at the resolved grid. The interpolation uses a six point Lagrangian interpolation formula in drop mass coordinate (Berry and Reinhardt, 1974) and a linear interpolation in salt mass coordinate. The total gain at grid  $i, j$  may be computed by integrating over all the  $k$ 's and  $l$ 's for  $k < i$  and  $l < j$ .

The second term in Eq. 6.2 gives the loss at drops with drop mass  $m(i)$  and salt mass  $n(j)$  and can be rewritten as:

$$\int_0^{\infty} \int_0^{\infty} W(m_i, m') f(m_i, n_j) f(m', n') dn' dm' =$$

$$f(m_i, n_j) \int_0^{\infty} W(m_i, m') \left[ \int_0^{\infty} f(m', n') dn' \right] dm' = f(m_i, n_j) \int_0^{\infty} W(m_i, m') f^*(m') dm'$$

where  $f^*(m') = \int_0^{\infty} f(m', n') dn'$ . We can compute  $f^*(m')$  first (i.e., the sum over all the LWC along the aerosol size bins); the remaining computation is then similar to the 1-D drop spectrum model.

In the following, I like to show that the coalescence computations in a 2-D drop spectrum model is as accurate as those in a 1-D spectrum model. The tests are based on Lagrangian air parcel model as described in Chapter 4, but this time I assume that there is no condensation/evaporation, and only drop collision takes place in the air parcel.

Fig. 5.1 shows the initial 2-D drop spectrum. The spectrum has LWC 0.4 g/kg and cloud drop concentration 200 cm<sup>-3</sup>, and is obtained by assuming a Gamma distribution function in drop size coordinate and an exponential distribution function

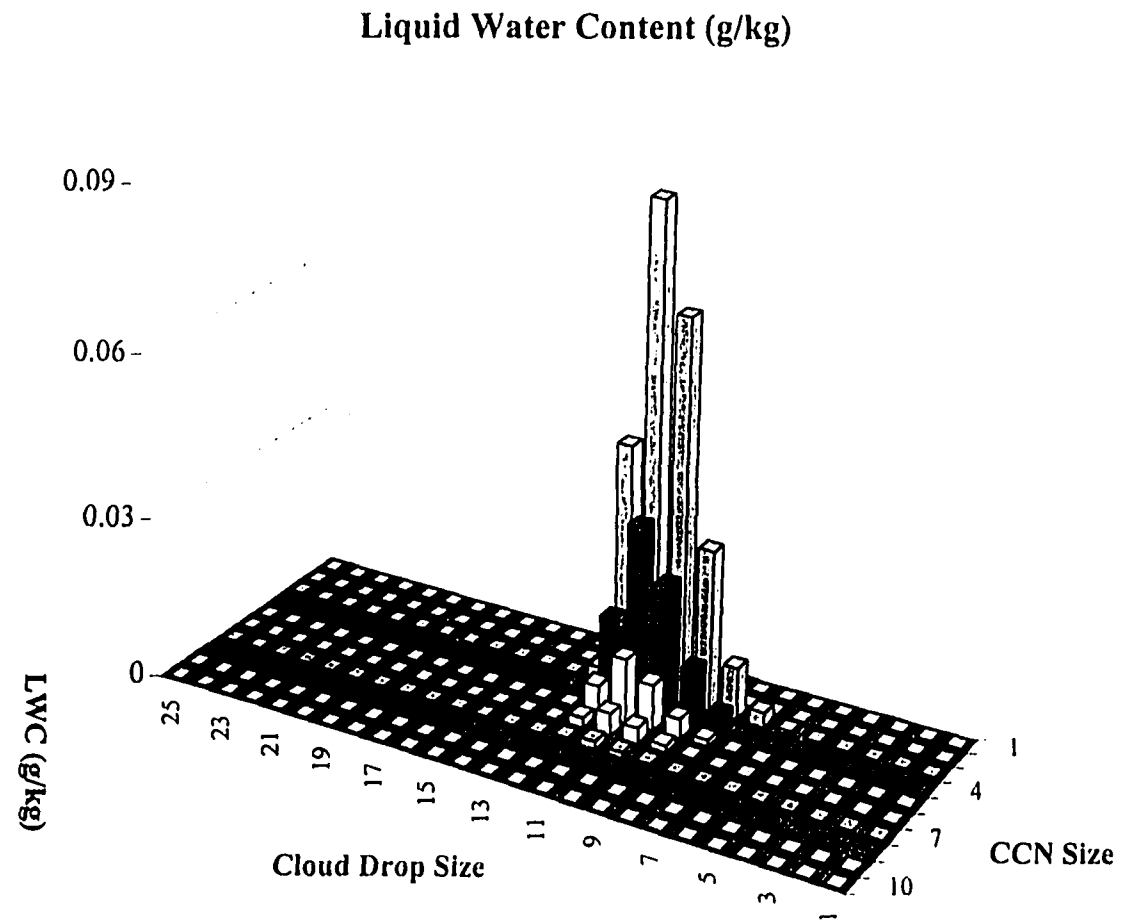


Figure 5.1. Initial 2-D LWC spectrum with liquid water content 0.4 g/kg and drop concentration 200 cm<sup>-3</sup>.

in CCN size coordinate. The model is run for two hours with time step of 1 second. Fig. 5.2 shows the 2-D drop spectrum at the end of the two hour simulation. Generally speaking, there is a net loss for small size particles and a net gain for large size particles. The spectrum shifts toward drops with large drop size and large CCN size.

Fig. 5.3a shows the evolution of LWC and salt mass inside the air parcel. The results show that the conservation of mass is excellent in both 2-D and 1-D drop spectrum model. After the two hour simulation, the LWC increases by 0.45% in 2-D drop spectrum model and by 0.55% in 1-D drop spectrum model. The salt volume increases by 0.07% in the 2-D spectrum model.

Fig. 5.3b shows the drop number change due to drop coalescence. A very good agreement between 2-D and 1-D drop spectrum models is obtained. The good agreement is due to the fact that salt mass does not influence the drop coalescence here. For a more detailed comparison, I also plotted the drop concentration spectrum and LWC spectrum and compare them with those of the 1-D drop spectrum model (Figs. 5.3c and 3d). Again, a very good agreement is obtained for the drop spectrum and LWC spectrum after 7200 time integration steps.

### **5.3 3-D simulation experiment of aerosol processing**

I show the simulation results based on the sounding taken during the flight A334 in the MAST field experiment. Cloud drop spectrum is represented by 25 bins in the size range from 1 to 256 micron, and 10 bins for CCN in the size range from 0.01 to 5.12 micron. The total number of prognostic equations in the model is 266, which includes 5 equations for the thermodynamical variables, one for the TKE, 10 for aerosol, and  $250=25 \times 10$  for cloud drop spectra. The simulation was made in a

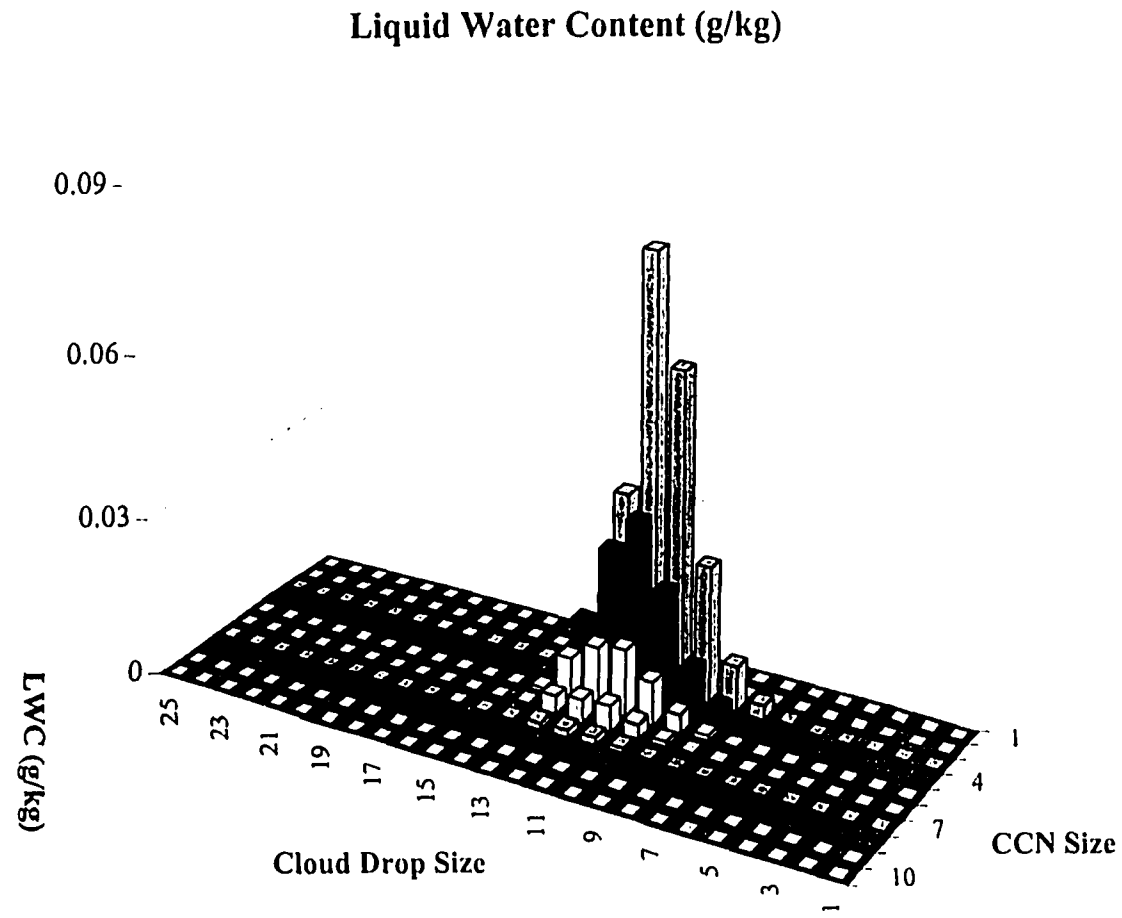


Figure 5.2. 2-D cloud drop spectrum after 2 hours coalescence simulation. Time step is 1 second.

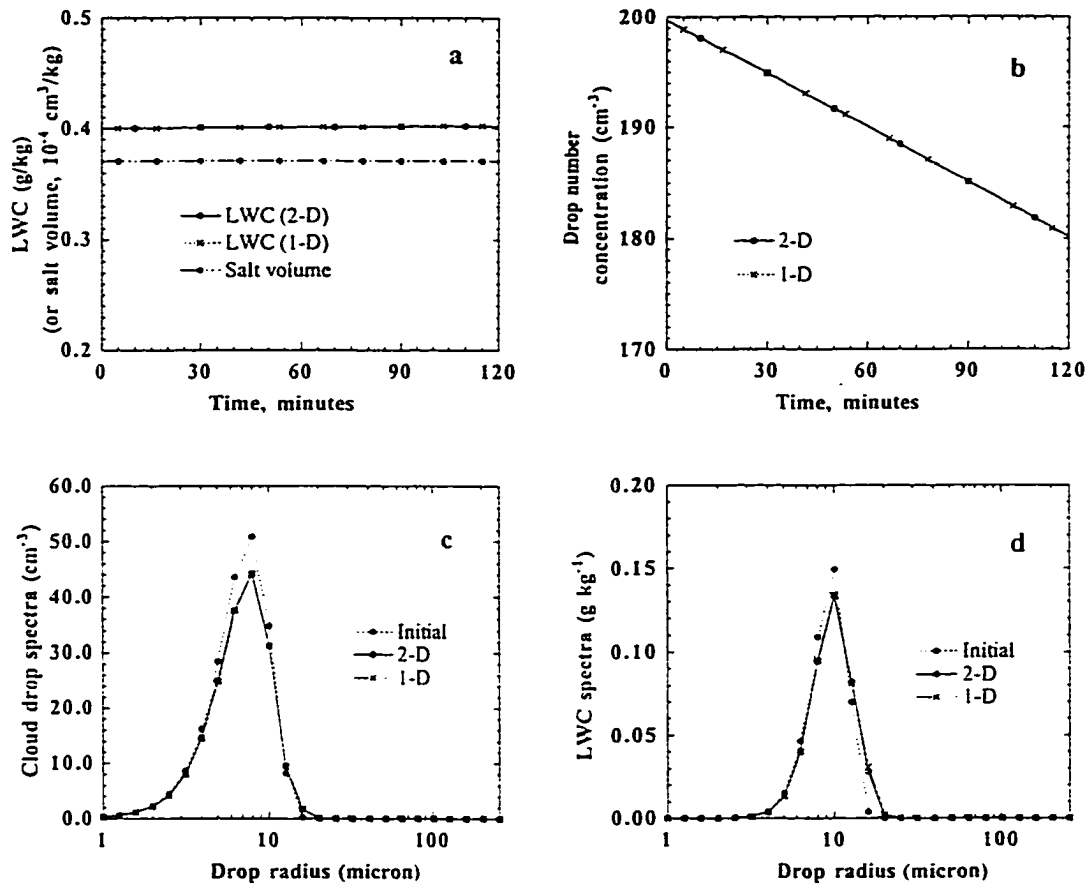


Figure 5.3. Time evolution of (a) LWC and salt mass, and (b) cloud drop concentration inside the air parcel for 2-D and 1-D cloud drop spectrum model. The size distribution of (c) drop concentration spectrum and (d) LWC spectrum at 2 hours are also plotted for 2-D and 1-D drop spectrum model.

domain using 32x32x40 grid points with grid sizes  $dx=dy=100\text{m}$ ,  $dz=20\text{m}$ . The aerosol spectrum is specified as  $N_{\text{CCN}}=CS^k$  with total number of CCN equal to  $700\text{ cm}^{-3}$  at 1.39% supersaturation. The model code has been parallelized and run on the CIMMS Hitachi 16 processors supercomputer. The model was first run in the bulk microphysics mode for 1.5 hours until the turbulence was fully developed. The simulation then continued for half an hour in the detailed microphysics mode with coalescence turned off. Coalescence started at 2 hours and the simulation continued for another 6 hours.

Fig. 5.4 shows the horizontally averaged vertical profiles of (a) liquid water potential temperature, (b) total water content, (c) liquid water content and (d) vertical velocity variance. Although there is a slight cooling and moistening in the lower part of the boundary layer (Fig. 5.4a, b) due to drizzle evaporation, the boundary layer is still rather well mixed. Drizzle has a significantly effect on the vertical velocity variance (Fig. 5.4d). Patches of drizzle tend to accumulate in the updraft region and the evaporation of the drizzle significantly reduces the buoyancy. The boundary layer circulation is primarily driven by strong radiation cooling at the cloud top, this can be seen from the maximum of the vertical velocity variance which is located at roughly two thirds of the mixed layer height (see also Moeng, 1986).

Fig.5.5 shows the CCN number loss due to coalescence and drizzle removal. Note that the drop number reduction due to drizzle is multiplied by 1000. It is clear that coalescence is responsible for nearly all of the CCN reduction. The rate of CCN number loss is approximately constant in time, as the LWC and drop concentration in the cloud layer do not change significantly throughout the simulation. Fig. 5.6 shows the activated CCN spectra at 5 and 8 hours into simulation. The reduction in large size CCNs at 8 hours is compensated by an increase in activation of small size CCN.

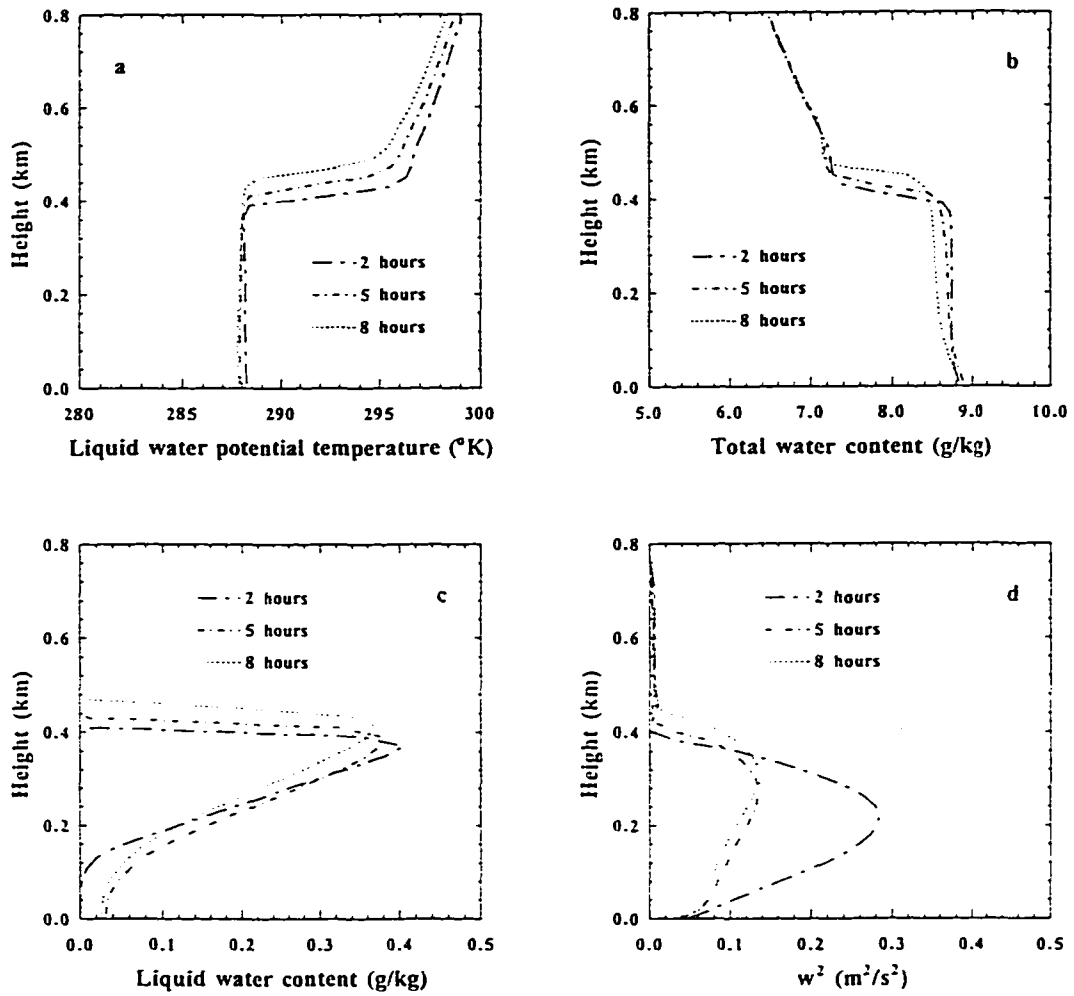


Figure 5.4. The horizontally averaged vertical profiles of (a) liquid water potential temperature, (b) total water content, (c) liquid water content and (d) vertical velocity variance at 2, 5 and 8 hours.

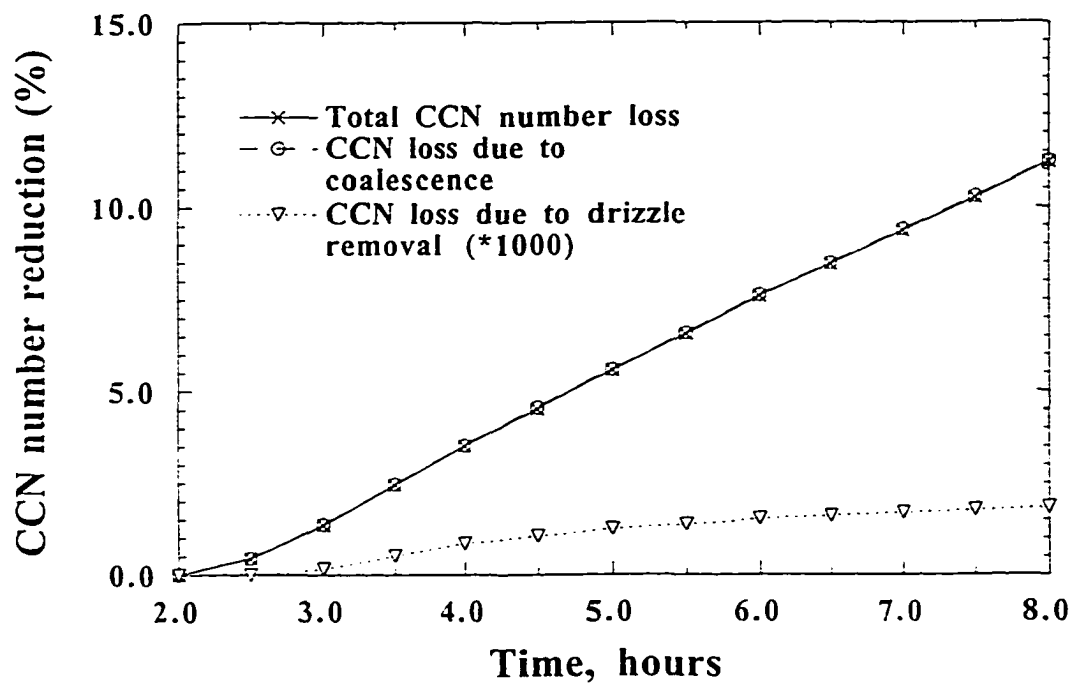


Figure 5.5. Time evolution of the CCN number loss due to coalescence (dashed line with circles), drizzle removal (dotted line with triangles, multiplied by 1000), and coalescence plus drizzle removal (total CCN loss) (solid line with crosses).



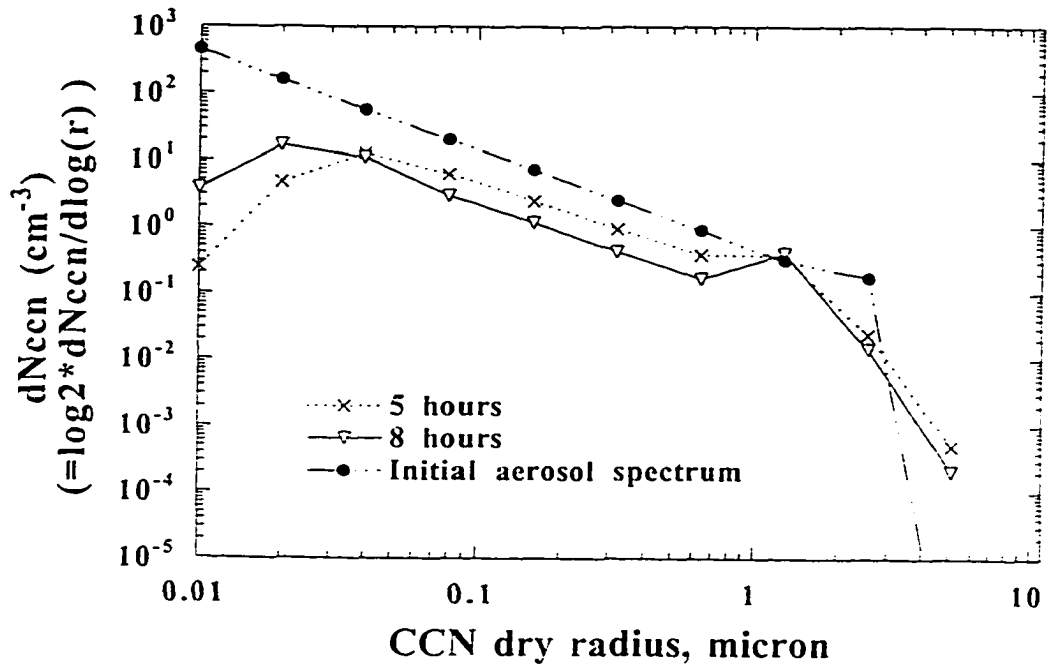


Figure 5.6. Activated CCN spectra averaged over the whole cloud at 5 hours (dotted line with crosses) and 8 hours (solid line with triangles) into simulation. Initial aerosol spectrum is also plotted (dash-dotted line with close circles)

The maximum supersaturation (not shown), which determines the activated CCN size, has also slightly increased from 5 to 8 hours.

If we assume that the rate of CCN number reduction due to coalescence remains constant and no other sinks/sources of CCN are present, then the CCN number concentration will be reduced in half in about 24 hours (the reduction of the CCN concentration is 11.3% for 6 hours of coalescence). For conditions selected in our simulation, the polluted air mass with the total aerosol concentration of  $700 \text{ cm}^{-3}$  will be transformed to a clean marine boundary layer air mass within about two days (CCN number will be reduced by 90%).

Although drizzle reduces the CCN number concentration rather insignificantly (Fig. 5.5), it removes roughly two thirds of the total salt mass (Fig. 5.7). Most of the salt mass loss from the boundary layer occurs mainly during the first three hours, after the 5th hour the loss is small and the salt mass content in the cloud and in the interstitial aerosol remains nearly constant. The salt loss is dominated by the removal of large size CCN particles. Even in terms of the CCN number, the larger CCNs are removed in greater numbers than the small size CCNs (Fig. 5.8). In terms of mass, the difference will amount to several orders of magnitude.

A statistics of the two parameter drop spectrum at various cloud levels is given by Fig. 5.9 and Fig. 5.10 which show the cross-sections of the DSSD along the CCN size and drop size coordinate. More precisely, Fig. 5.9 shows the liquid water distribution integrated over all drop bins as a function of CCN size, while Fig. 5.10 shows the same distribution (horizontally averaged and integrated over all CCN bins) as a function of drop size. Near cloud base ( $z=0.10 \text{ km}$ , Fig. 5.9b), the liquid water is more or less evenly distributed over all activated CCN categories. However, at higher levels the maximum of the LWC falls into the aerosol category which has the

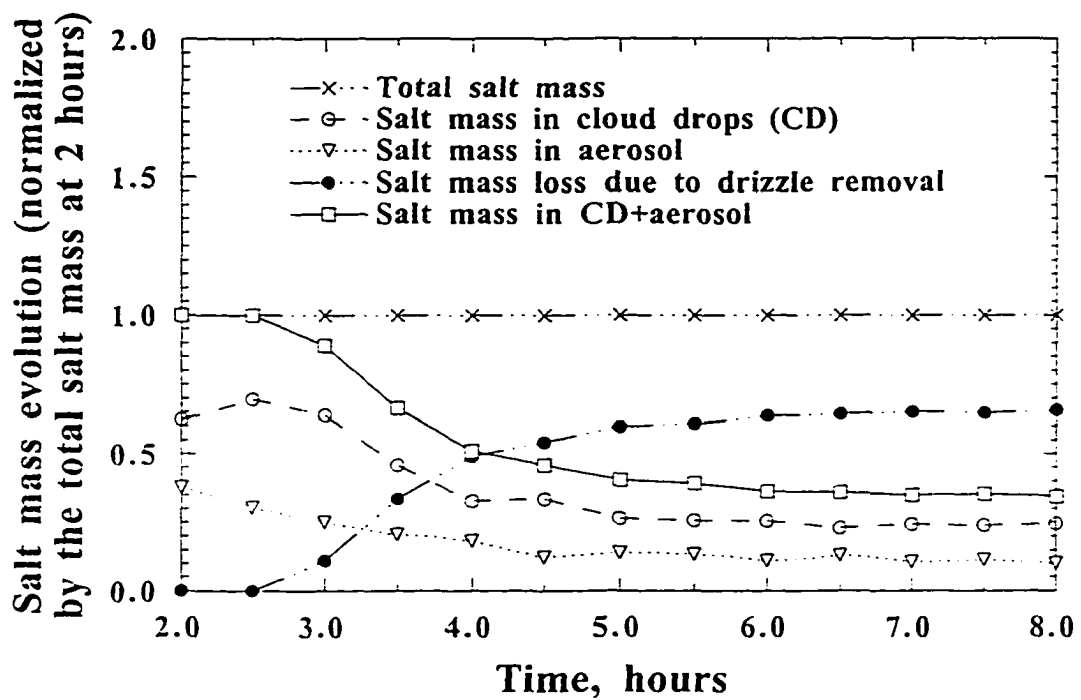


Figure 5.7. Evolution of the salt mass content in cloud drops (dashed line with open circles), aerosol particles (dotted line with triangles), drizzle particles fallout (dash-dotted line with close circles), cloud drops and aerosol particles (solid line with boxes) and total salt mass (dash-dotted line with crosses). The salt mass has been normalized with respect to the initial total salt mass in the domain.

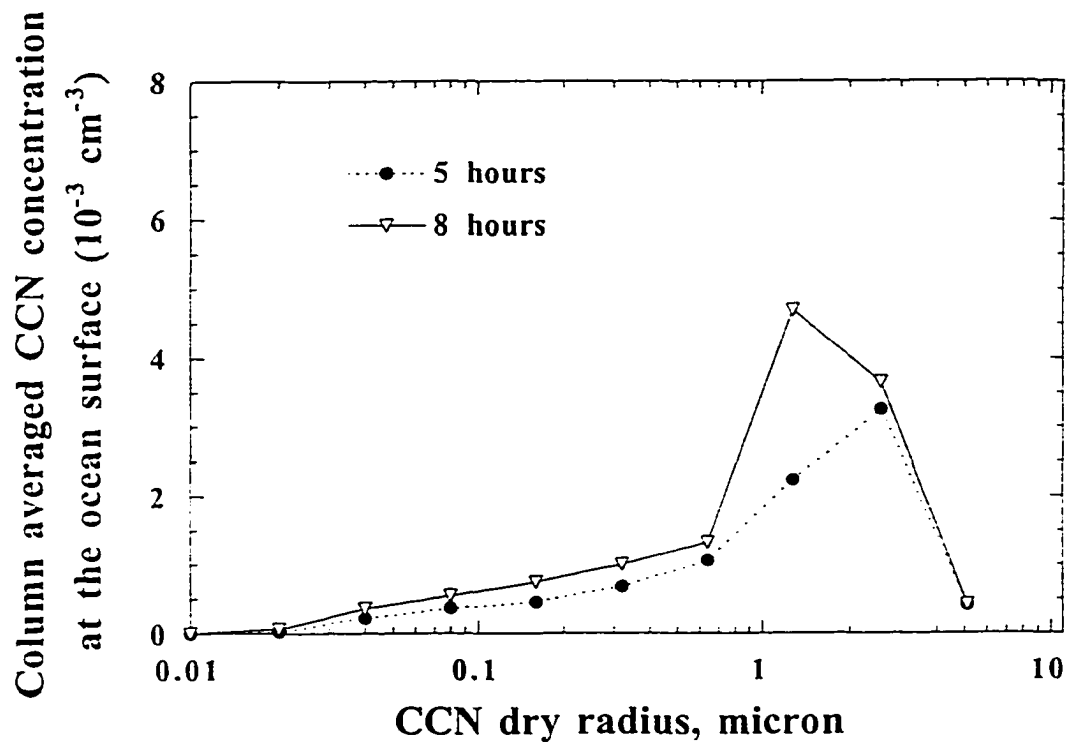


Figure 5.8. Accumulated (column averaged) CCN concentration spectrum at the ocean surface at 5 and 8 hours.

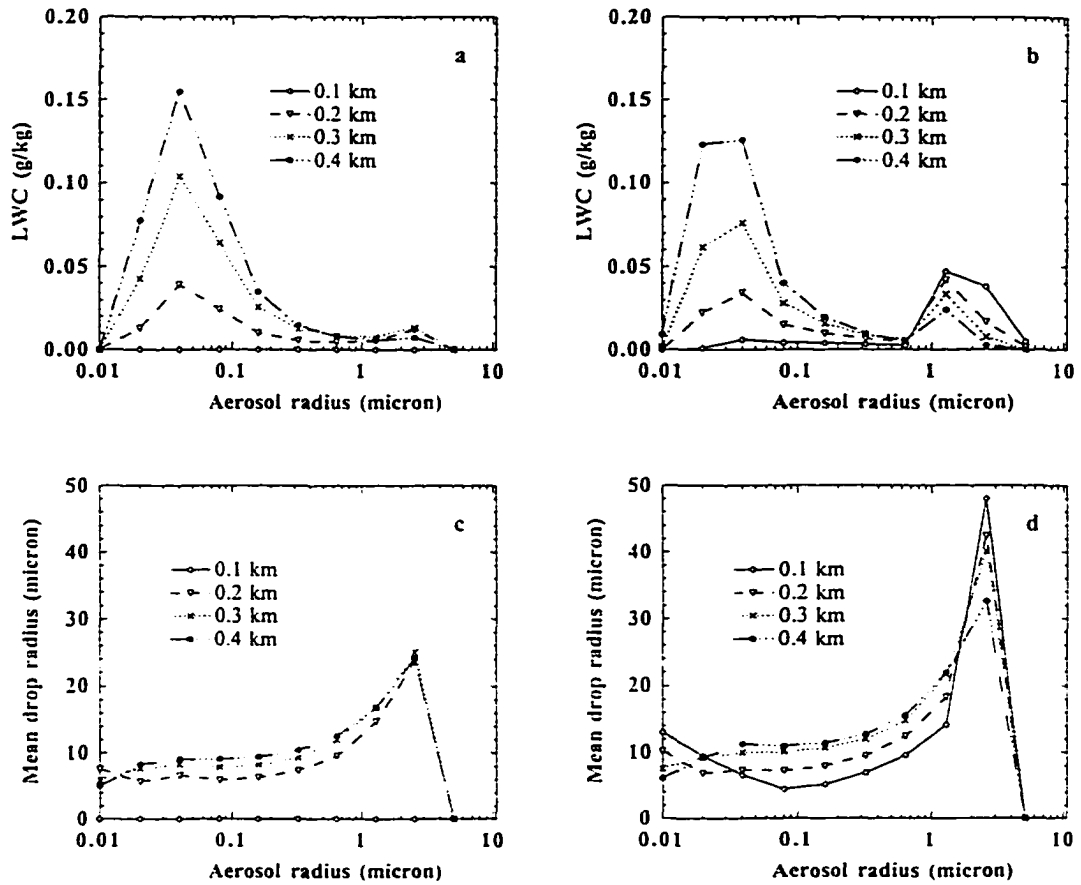


Figure 5.9. Horizontally averaged LWC distribution as functions of CCN size (integrated over all cloud drop bins) at 2 hours (a) and 8 hours (b). (c) and (d) show the horizontally averaged mean drop radius as a function of CCN size at 2 hours and 8 hours, respectively.

maximum number of activated CCN particles (solid line with triangles in Fig. 5.6). The mean drop radius at the same cloud level (Figs. 5.9c, d) slightly depends on the CCN category which shows that cloud drops become rather quickly diluted and the effect of the salt on the drop growth is insignificant, except of very large drops. The large peak in the smallest CCN size (Fig. 5.9 d) may be caused by high growth rate (these CCN are activated at relatively high supersaturations) and small sample of statistics (very small number of CCN particles,  $0.01 \text{ cm}^{-3}$ ). The LWC spectra (Fig. 5.10b) show that there are more large drizzle drops in the lower part of the cloud compared to upper cloud levels. Large drops formed at upper level of the cloud collect small drops as they fall and grow even bigger.

Fig. 5.11 shows the particle distributions for activated CCNs and interstitial aerosols at 5 hours. For small size particles, only part of aerosol particles is activated by nucleation and the rest becomes interstitial aerosols. The percentage of activated aerosol particles varies from 0 to 100% depending on the aerosol category. For example, at bin 3 (aerosol size of  $0.04 \mu\text{m}$  and the corresponding critical supersaturation of 0.2%) only about 40% of aerosols are activated. The partial activation is due to the large scatter in vertical velocities and, hence, the large scatter in supersaturations at the cloud base. As a result, some number of large aerosol particles will remain unactivated at certain locations and exist as interstitial aerosols. For example, particles in bin 4 (aerosol size of  $0.08 \mu\text{m}$  corresponding to critical supersaturation of 0.06%) have not been completely activated and most likely have been brought into the cloud layer by relatively weak updrafts or by entrainment from the cloud top.

The effects of coagulation on the aerosol spectra after 6 hour are summarized in Figs. 5.12, 5.14 and 5.15. Fig. 5.12 shows the average aerosol spectra in the

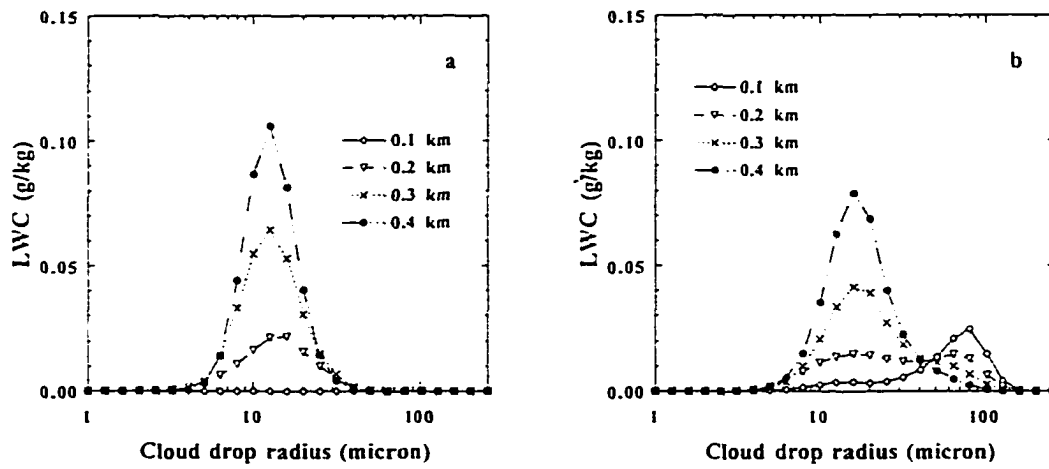


Figure 5.10. Horizontally averaged LWC distribution as functions of cloud drop size (integrated over all CCN bins) at 2 hours and 8 hours, respectively.

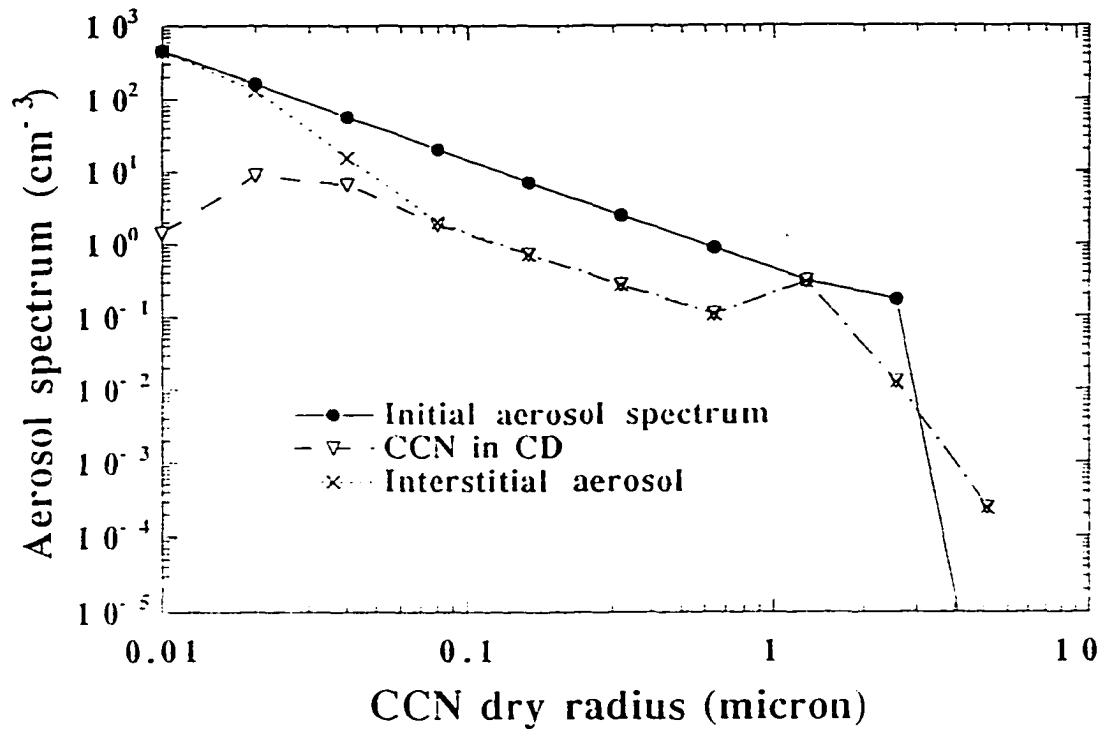


Figure 5.11. Activated CCNs and interstitial aerosol distributions at 5 hours into simulation.



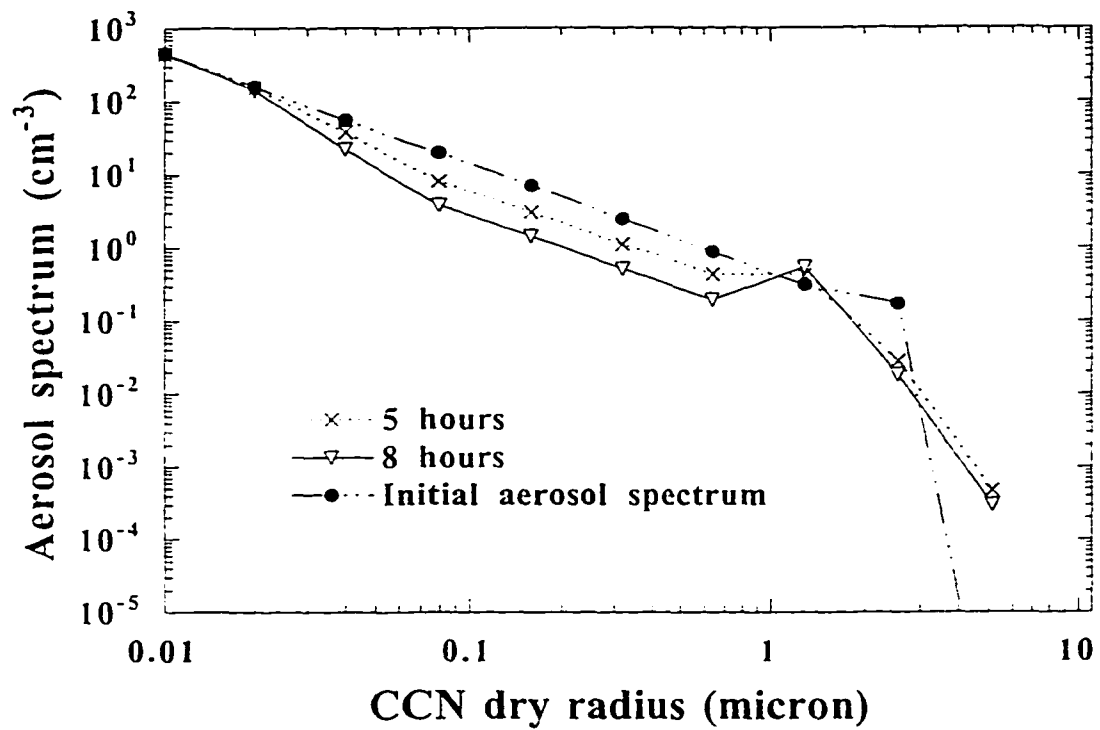


Figure 5.12. The average aerosol spectra in the boundary layer at 5 and 8 hours if the cloud were completely evaporated.

boundary layer at 5 and 8 hours if the cloud were completely evaporated. The physical processes responsible for the spectra changes are coalescence and drizzle removal. Coalescence decreases the number of small and middle size CCN particles and produces the large size CCN particles. On the other hand, drizzle precipitation removes mainly large size CCNs. The combination of the two processes reduces both the small and the large size CCNs, resulting in a local CCN maximum at about 1.2  $\mu\text{m}$  radius.

The mass removal from the fine CCN particles (from 0.05  $\mu\text{m}$  to 0.5  $\mu\text{m}$  in radius) has an important effect on the atmospheric visibility. Fig. 5.13 shows the scattering coefficient of a single particle per unit volume as a function of the particle diameter for spheres with a refractive index of 1.50 for the light with wavelength 0.55  $\mu\text{m}$  (green light). The portion of the total extinction due to particle scattering,  $b_{\text{sp}}$ , can be obtained by integrating the product of the curve in Fig. 5.13 and the particle volume size distribution. For relatively polluted air, the extinction coefficient,  $b_{\text{ext}}$ , can be approximated by (Hidy, 1994)

$$b_{\text{ext}} \cong \text{constant} \times \text{mass concentration of fine particles}$$

The visual range (visibility) is defined as:

$$\text{VR} = 3.9/b_{\text{ext}}$$

Fig. 5.14 shows the visibility increase due to the coalescence removal of fine size particles. The salt mass concentration of the fine size particles is also plotted. The visual range increases by a factor of 4.6 within six hours due to cloud processing.

Fig. 5.15 compares the CCN activation spectra before and after the cloud processing. The effect of cloud processing on the CCN activation is significant. For

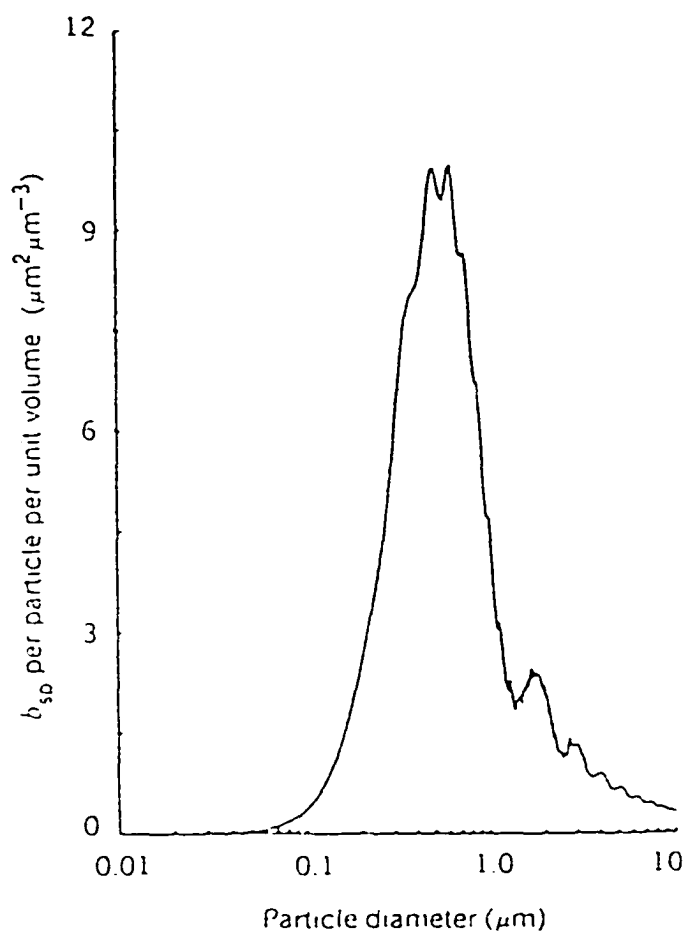


Figure 5.13. Scattering coefficient of a single particle per unit volume as a function of the particle diameter for spheres with a refractive index of 1.5 and light of wavelength  $0.55 \mu\text{m}$  (from Waggoner and Charlson, 1976).

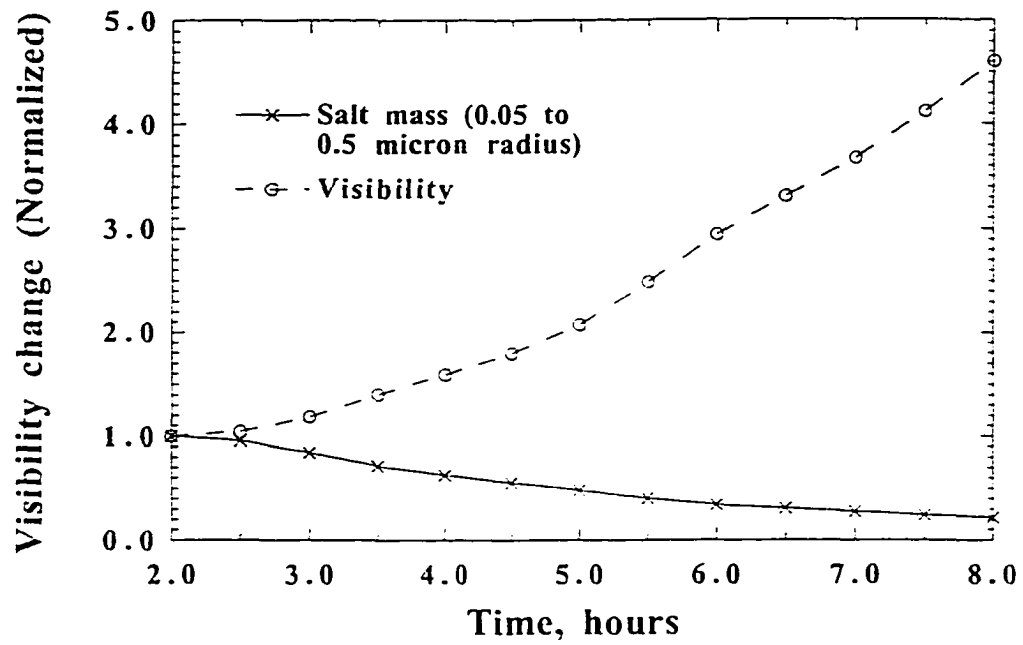


Figure 5.14. Visibility increase due to cloud processing of aerosols as a function of time.

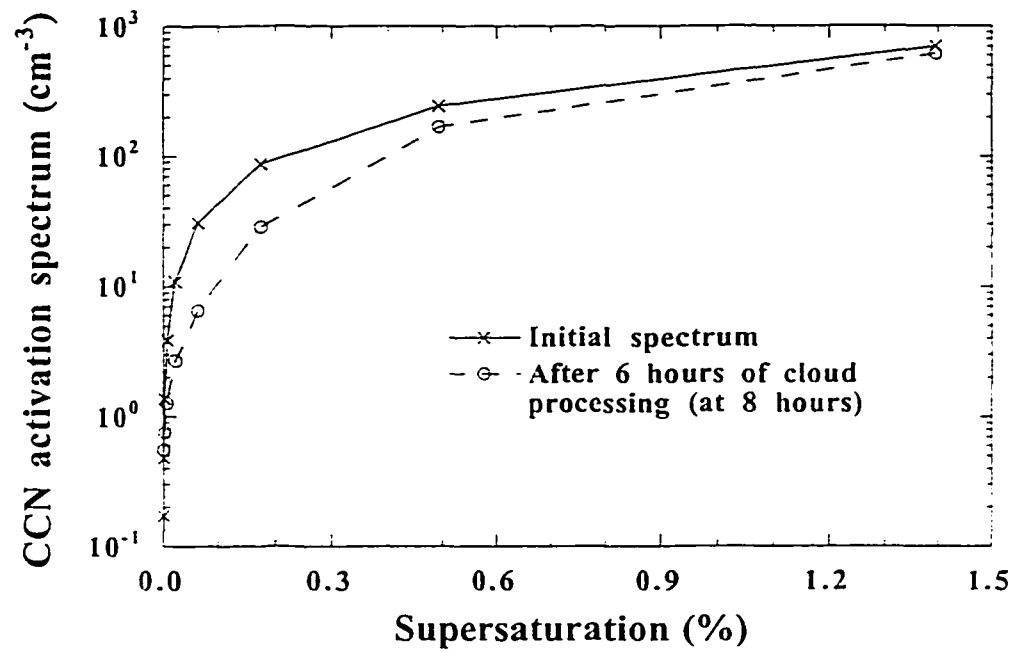


Figure 5.15. Effects of cloud processing on the total number of activated CCN as a function of supersaturation.

example, at supersaturation 0.2%, the number of activated CCN has been reduced roughly by 50% (from 100 to 50  $\text{cm}^{-3}$ ). In order to activate the same number of CCN, the supersaturation must increase by 0.1%, (i.e., from 0.2% to 0.3%). The reduction of the CCN activation rate at a given supersaturation will significantly influence the cloud microstructure, drizzle formation and the cloud radiative properties as discussed in Chapter 1.

## 5.4 Conclusions

I presented results from a simulation of aerosol spectra transformation in a polluted air mass moving over an ocean boundary layer. The aerosol spectra have been transformed due to physical processing of aerosols by cloud particles. In particular, the processes of nucleation scavenging, drop coalescence, and removal by drizzle fallout have been considered. The study was based on a new version of the CIMMS LES model that is capable of tracking the aerosol salt content inside the cloud drops.

The 3-D simulation of the cloud processing effects in a stratocumulus cloud-topped boundary layer have demonstrated the changes in the salt distribution inside cloud drops and in the interstitial aerosol. Based on my simulation results, I conclude:

a) Continental (polluted) air in the simulated case can be modified to marine air within approximately 2 days by reducing the aerosol number concentration by about 90%. This reduction occurs only due to the combined effects of nucleation scavenging, drop coalescence and drizzle fallout. The effects of other scavenging processes can also be important but has not been considered in the present study.

b) Drizzle precipitation removes negligible number of CCN particles, but substantially reduces the aerosol mass.

c) Coalescence can significantly remove the mass concentration of the fine size particles (from 0.05  $\mu\text{m}$  to 0.5  $\mu\text{m}$  in radius), where particles contribute the most to the visibility reductions. The visual range is increased by a factor of 4.3 during six hours of simulation.

d) Large CCN particles created by drop coalescence in addition to the existing large CCN particles are efficiently removed by drizzle fallout. The coalescence process mostly affects the medium size CCN particles (from 0.08 to 0.8 micron) and results in a net reduction of the number of CCN particles which would activate at a given supersaturation. For example, at supersaturation 0.2%, the number of CCN activated is reduced roughly by 50% (from 100 to 50  $\text{cm}^{-3}$ ).

## Chapter

# 6

## Summary and conclusions

My research consists of three parts discussed in detail in Chapter 3, 4 and 5. My major objective was to study the aerosol-cloud interactions using the CIMMS LES model. In the old version of the CIMMS LES model, the cloud drop spectrum was artificially broadened in the condensation procedure. To limit the artificial broadening, I have developed a variational optimization method which has been implemented in the CIMMS LES model. The improved CIMMS LES model was then used to study the aerosol effects on cloud microstructure and cloud radiative properties through ship track simulation. In order to study the cloud processing of aerosols, an enhanced version of the CIMMS LES model that includes a two parameter cloud drop spectrum has been developed. The model is used to simulate the mass transformation in a polluted air mass moving over an ocean boundary layer.



Chapter 3 discusses in detail the improvement of the condensation procedure in the CIMMS LES model using variational optimization method. The method is tested against the exact solution using more than 15,000 spectra selected from experiments based on CIMMS LES model with explicit microphysics. The results show that the variational method not only conserves the integral parameters of the spectrum, such as drop number, mean radius, liquid water content and the effective radius, but also provides very accurate calculation of the spectrum itself. The accuracy of the variational method is comparable to or even better than the accuracy of the Egan and Mahoney (1972) scheme. The variational method has, however, an important advantage compared to the latter method. It requires specification of only one variable in each bin size, while the EM scheme needs retaining of the three moments of the spectrum, thus tripling the memory requirements in the model. For multidimensional models this presents a serious limitation and makes the application of EM method impractical.

We would like to note that the errors associated with condensational remapping are most significant in the size range of 1 to 200 micron which is typical for drops in stratiform clouds. The application of the VO method for this type of clouds is strongly recommended. In the convective clouds where the drop size range is much wider and the drop spectra sometimes exhibit very complex multimodal shapes, the performance of the VO method has not been thoroughly tested. However, we do expect a good performance of the VO method in convective cloud models as well for two reasons. First, for large cloud drops ( $r \geq 200 \mu\text{m}$ ) the growth by condensation is very small ( $\Delta r \ll r$ ), therefore, the condensational remapping is rather insensitive to a particular scheme. In addition, for drops larger than 100-200 microns, the condensational growth is much smaller than the coalescence growth, consequently, the errors of the condensational remapping are also smaller than the errors associated

with the coagulation calculations. It is our experience that for drops larger than 100 microns, the use of a simpler method, such as the Kovetz and Olund's (1969) method, is quite warranted.

The aerosol effects on cloud microphysics and cloud radiative properties has been studied through the simulation of ship track formation based on CIMMS large eddy simulation (LES) model. The CIMMS LES model includes coupled 3-D large eddy simulation dynamics, explicit microphysics and radiative processes. The CIMMS LES model has been run using both bulk and explicit microphysics to study ship track formation under various boundary layer conditions. Using a bulk thermodynamic formulation, I contrast the rates of effluent transport through a well-mixed boundary layer and through a decoupled layer. I also simulate the effects of heat injected by the ship engine exhaust on the transport of ship effluents into the cloud layer, finding a significant effect. Using an explicit microphysical model, I carry out simulations in clean and relatively polluted air. I find that a ship track forms easily in a well-mixed convective boundary layer in an environment with low cloud condensation nuclei, but its formation may be suppressed by the stable transition layer in the decoupled case. I also find that a ship track survives longer in a clean boundary layer than in a polluted environment. In the clean environment, drizzle is clearly suppressed. In the relatively polluted environment, drizzle suppression is small, particularly in the decoupled boundary layer. The drop spectra inside the ship track are relatively narrow and are composed mostly of small drops, whereas the drop spectra outside the ship track show primarily bimodal distributions. The calculated albedo shows a substantial increase inside the ship track. The liquid water content inside the ship track may, however, be lower or higher than that outside, depending on specific characteristics of the boundary layer, such as mixed layer

depth, stability of the transition layer, and the concentration of cloud condensation nuclei.

Not only are the stratocumulus cloud layers affected by the ambient aerosols, but, in turn, they can also substantially affect the ambient aerosol distributions. For the study of the aerosol processing by stratocumulus clouds, a two parameter spectrum that depends both on the drop mass and the solute mass, has been introduced in the CIMMS LES model.

The results from LES model simulation of aerosol spectra transformation in a polluted air mass moving over an ocean boundary layer have been presented. The aerosol spectra have been transformed due to physical processing of aerosols by cloud particles. The 3-D simulation of the cloud processing effects in a stratocumulus cloud-topped boundary layer have demonstrated the changes in the salt distribution inside cloud drops and in the interstitial aerosol. Based on my simulation results, I conclude:

a) Continental (polluted) air can be modified to marine air within approximately 2 days by reducing the aerosol number concentration by about 90%. This reduction occurs only due to the combined effects of nucleation scavenging, drop coalescence and drizzle fallout. The effects of other scavenging processes can also be important but has not been considered in the present study.

b) Drizzle precipitation removes negligible number of CCN particles, but substantially reduces the aerosol mass.

c) Coalescence can significantly remove the mass concentration of the fine size particles (from 0.05  $\mu\text{m}$  to 0.5  $\mu\text{m}$  in radius), where particles contribute the most to

the visibility reductions. The visual range is increased by a factor of 4.3 during six hours of simulation.

d) Large CCN particles created by drop coalescence in addition to the existing large CCN particles are efficiently removed by drizzle fallout. The coalescence process mostly affects the medium size CCN particles (from 0.08 to 0.8 micron) and results in a net reduction of the number of CCN particles which would activate at a given supersaturation. For example, at supersaturation 0.2%, the number of CCN activated is reduced roughly by 50% (from 100 to 50  $\text{cm}^{-3}$ ). The reduction of the CCN activation rate at a given supersaturation will significantly influence the cloud microstructure, drizzle formation and the cloud radiative properties as discussed in Chapter 1.

## REFERENCES

- Ackerman A., O. B. Toon, and P. V. Hobbs, 1992: Numerical modeling of stratocumulus-topped marine boundary layer. *The 11th International Conference on Clouds and Precipitation*, Aug. 17-21, 1992, Montreal, Canada.
- Ackerman, A.S., O.B. Toon, P.V. Hobbs, 1993: Dissipation of marine stratiform clouds and collapse of the marine boundary layer due to the depletion of cloud condensation nuclei by clouds. *Science*, 262, 226-229.
- Albrecht, B.A., 1989: Aerosols, cloud microphysics, and fractional cloudiness. *Science*, 245, 1227-1230.
- Baker, M.B., and R.J. Charlson, 1990: Bistability of CCN concentrations and thermodynamics in the cloud-topped boundary layer. *Nature* 345, 142-144.
- Berry, E.X., 1967: Cloud droplet growth by coalescence. *J. Atmos. Sci.*, 24, 688-701.
- Berry, E.X. and R.L. Reinhardt, 1974: An analysis of cloud drop growth by collection: Part I. Double Distributions. *J. Atmos. Sci.*, 31, 1814-1824.
- Bleck, R., 1970: A fast, approximate method for integrating the stochastic coalescence equation. *J. Geophys. Res.*, 75, 27, 5165-5171.
- Byers, H.R., 1965: *Elements of cloud physics*. University of Chicago Press, 191pp.
- Charlson, R. J. , S. E. Schwartz, J. M. Hales, R. D. Cess, J. A. Coakley, Jr., J. E. Hansen, and D. J. Hoffman, 1992: Climate forcing by anthropogenic aerosols. *Science*, 255, 423-430.
- Colella, P. and P.R. Woodward, 1984: The piecewise parabolic method (PPM) for gas-dynamic simulations. *J. Comput. Phys.*, 54, 174-201.
- Deardorff, J. W. and G. E. Willis, 1975: A parameterization of diffusion into the mixed layer. *J. Appl. Meteor.*, 14, 1451-1458.
- Deardorff, J. W., 1980: Stratocumulus-capped mixed layers derived from a three-dimensional model. *Bound. Layer Meteor.*, 18, 495-527.
- Egan, B.A. and J.R. Mahoney, 1972: Numerical modeling of advection and diffusion of urban area source pollutant. *J. Appl. Meteor.*, 11, 312-322.

- Ferek, R.J., T Garret, S. Strader, K. Nielson, G.E. Innis, J.P. Taylor, A.S. Ackerman, Y. Kogan, Q. Liu, B.A. Albrecht, D. Babb, 1996: Drizzle suppression in ship tracks. To be submitted to *J. Atmos. Sci.*.
- Flossman, A.I., 1991: The scavenging of two different types of marine aerosol particles calculated using a two-dimensional detailed cloud model. *Tellus*, **43B**, 301-321.
- Flossman, A.I., W.D. Hall, and H.R. Pruppacher, 1985: A Theoretical Study of the Wet Removal of Atmospheric Pollutants. Part I: The Redistribution of Aerosol Particles Captured through Nucleation and Impaction Scavenging by Growing Cloud Drops. *J. Atmos. Sci.*, **42**, 583-606.
- Flossman, A.I., and H.R. Pruppacher, 1988: A Theoretical Study of the Wet Removal of Atmospheric Pollutants. Part III: The Uptake, Redistribution, and Deposition of  $(\text{NH}_4)_2\text{SO}_4$  Particles by a Convective Cloud Using a Two-Dimensional Cloud Dynamics Model. *J. Atmos. Sci.*, **45**, 1857-1871.
- Gerber, H., 1995: Microphysics of marine stratocumulus clouds with two drizzle modes. Submitted to *J. Atmos. Sci.*.
- Greenfield, S.M., 1957: Rain scavenging of radioactive particulate matter from the atmosphere. *J. Meteor.*, **14**, 115-125.
- Harshvardhan, 1993: *Aerosol-cloud-climate interactions*. Edited by P. V. Hobbs. Academic Press, New York, 233 pp, 76-96.
- Hartmann, D.L., M. E. Ockert-Bell, and M.L. Michelsen, 1992: The effect of cloud type on Earth's energy balance: global analysis. *J. Climate*, **5**, 1281-1304.
- Hegg, D.A., 1983: The source of sulfate in precipitation. 1. Parameterization scheme and physical sensitivities. *J. Geophys. Res.*, **88**, 1369-1374.
- Hegg, D.A., 1990: Heterogeneous production of cloud condensation nuclei in the marine atmosphere. *Geophys. Res. Lett.*, **17**, 2126-2168.
- Hegg, D.A., L.F. Radke, and P.V. Hobbs, 1990: Particle production associated with marine clouds. *J. Geophys. Res.*, **95**, 13,917-13,926.
- Hegg, D.A., L.F. Radke, and P.V. Hobbs, 1991: Measurements of Aitken nuclei and cloud condensation nuclei in the marine atmosphere and their relation to the DMS-cloud-climate hypothesis. *J. Geophys. Res.*, **96**, 18727-18733.
- Hidy, G. M., 1994: *Atmospheric sulfur and Nitrogen oxides*. Academic Press, 447 pp.
- Hoppel, W.A., 1989: *Aerosols and Climate*, P.V. Hobbs and M.P. McCormic, Eds. A. Deepak Pub., 9-19.

- Hoppel, W.A., G.M. Frick, and R.E. Larson, 1986: Effect of non-precipitating clouds on the aerosol size distribution in the marine boundary layer. *Geophys. Res. Lett.*, **13**, 125-128.
- Houze, R. A., Jr., 1993: *Cloud dynamics*. Academic Press, New York, 573 pp.
- Hudson, J.G., 1993: Cloud condensation nuclei near marine cumulus. *J. Geophys. Res.*, **98**, 2693-2702.
- Hudson, J.G. and P.R. Frisbie, 1991: Cloud condensation nuclei near marine stratus. *J. Geophys. Res.*, **96**, No. D11, 20795-20808.
- , and P.R. Frisbie, 1991: Cloud Condensation Nuclei Near Marine Stratus. *J. Geophys. Res.*, **96**, 20795-20808
- Innis, G.E., J.W. Rottman, Y. Kogan, Q. Liu, W. Porch, and J. Kao, 1996: The effects of ship-generated boundary layer perturbations on ship tracks. To be submitted to *J. Atmos. Sci.*
- Johnson, D. W., C. S. Bretherton, I. M. Brooks, P. Durkee, S. Osborne, K. Nielson, H. A. Rand, D. P. Rogers and D. Percial, 1995: 8th June 1994 case study: Keystone Canyon and Hyundai Duke. *Monterey area ship track experiment 2nd data workshop*. London, July 25-27, 1995.
- Khairoutdinov, M. F., 1997: Ph.D thesis, The Univ. of Oklahoma, Norman, Oklahoma.
- Khairoutdinov, M. F. and Y. L. Kogan, 1996: Case study of radiation and drizzle effects in a LES model with explicit microphysics. To be submitted to *J. Atmos. Sci.*
- King, M. D., Si-Chee Tsay, and S. Platnick, 1995: In situ observations of the indirect effects of aerosols on clouds. *Aerosol Forcing of Climate*. Edited by R.J. Charlson and J. Heintzenberg. Published by John Wiley & Sons, New York.
- Kogan, Y.L., 1991: The simulation of a convective cloud in a 3-D model with explicit microphysics. Part I: Model description and sensitivity experiments. *J. Atmos. Sci.*, **48**, 1160-1189.
- Kogan, Y. L., M. P. Khairoutdinov, D. K. Lilly, Z. N. Kogan, and Q. Liu, 1995: Modeling of stratocumulus cloud layers in a large eddy simulation model with explicit microphysics. *J. Atmos. Sci.*, **52**, 2923-2940.
- Kogan, Z.N., Y. L. Kogan and D. K. Lilly, 1996: Study of the anthropogenic sulfate aerosols indirect effect in marine stratocumulus clouds. *Proceedings of*

- the 12th International Conference on Clouds and Precipitation, Volume 2.*  
19-23 August 1996, Zurich, Switzerland.
- Kornfeld, P., 1970: Numerical solution for condensation of atmospheric vapor on soluble and insoluble nuclei. *J. Atmos. Sci.*, **27**, 256-264.
- Kovetz, A., and B. Olund, 1969: The effect of coalescence and condensation on rain formation in a cloud of finite vertical extent. *J. Atmos. Sci.*, **26**, 1060-1065.
- Kreidenweis, S.M., G. Feingold, B. Stevens and W. R. Cotton, 1996: Cloud processing of aerosol in the stratocumulus-capped marine boundary layer. *Proceedings of the 12th International Conference on Clouds and Precipitation, Volume 2.* 19-23 August 1996, Zurich, Switzerland.
- Lamb, R. G., 1982: Diffusion in the convective boundary layer. *Atmospheric Turbulence and Air Pollution Modeling*. Edited by F. T. M. Nieuwstadt and H. van Dop. Published by Kluwer Boston Inc., Hingham, MA.
- Lewis, J.M., 1972: An operational upper air analysis using the variational method. *Tellus*, **24**, 514-530.
- Lilly, D.K., 1962: On the numerical simulation of buoyant convection. *Tellus*, **14**, 148-172.
- Lilly, D.K., 1967: The representation of small-scale turbulence in numerical simulation experiments. *Proceedings of the IBM Scientific Computing Symposium on Environmental Sciences*, White Plains, N.Y., 195-210.
- Lilly, D. K., 1968: Models of cloud-topped mixed layers under a strong inversion. *Q. J. R. Meteor. Soc.*, **94**, 292-309.
- Liu, Q.-F., Y. L. Kogan, and D. K. Lilly, 1995: Reducing the numerical dispersion of the cloud droplet spectrum in condensation calculations. *Preprints of the Conference on Cloud Physics*, 15-20 January 1995, Dallas, TX.
- Liu, Q.-F., Y. L. Kogan, D. K. Lilly, and M. P. Khairoutdinov, 1996: Variational optimization method for calculation of cloud drop growth in an Eulerian drop-size framework. Submitted to *J. Atmos. Sci.*
- Lowe, J. A., M.H. Smith, C.D. O'Dowd, and S.L. Clegg, 1996: The effects of sea-salt aerosol on the production of sulfate in the marine atmospheric boundary layer and its effect on stratiform clouds. *Proceedings of the 12th International Conference on Clouds and Precipitation, Volume 2.* 19-23 August 1996, Zurich, Switzerland.
- McDonald, J. E., 1964: Cloud nucleation on insoluble particles. *J. Atmos. Sci.*, **21**, 109-116.



- Minnis, P., C.H. Whitlock, T.P. Charlock, G.L. Schuster, W.L. Smith, Jr. and L. Nguyen, 1996: Cloud shortwave radiation forcing from satellite and surface data during the ARM enhanced shortwave experiment. *Proceedings of the sixth atmospheric radiation measurement (ARM) science team meeting*, March 4-7, 1996, San Antonio, Texas.
- Moeng, C.-H., 1984: A large-eddy simulation model for the study of planetary boundary layer turbulence. *J. Atmos. Sci.*, 41, 2052-2062.
- Moeng, C.-H., 1986: Large-eddy simulation of a stratus-topped boundary layer. Part I: Structure and budgets. *J. Atmos. Sci.*, 43, 2886-2900.
- Nicholls, S., 1984: The dynamics of stratocumulus: Aircraft observations and comparisons with a mixed-layer model. *Quart. J. Roy. Meteor. Soc.*, 110, 783-820.
- Ochs, H.T., and C.S. Yao, 1978: Moment conserving techniques for microphysical computations. Part I: numerical techniques. *J. Atmos. Sci.*, 35, 1947-1958.
- Pasquill, F. and F. B. Smith. 1983: *Atmospheric Diffusion*. Third edition. Published by John Wiley and Sons, New York.
- Penner, J.E., R.J. Charlson, J.M. Hales, N. Laulainen, R. Leifer, T. Novakov, J. Ogren, L.F. Radke, S.E. Schwartz, and L. Travis, 1994: Quantifying and minimizing uncertainty of climate forcing by anthropogenic aerosols. *Bull. Am. Meteorol. Soc.* 75, 375-400.
- Porch W. M., C. J. Kao, T. G. Kyle, and R. G. Kelley, 1989: Ship trail/cloud dynamic effects from apollo-soyuz photograph July 16, 1975. *Preprints of the Symposium on the Role of Clouds in Atmospheric Chemistry and Global Climate*, 161-164, January 29 - February 3, 1989, Anaheim, California.
- Pruppacher, H. R., and J. D. Klett, 1978: *Microphysics of clouds and precipitation*. D.Reidel, 714pp.
- Radke, L.F., 1983: In: *precipitation scavenging, dry deposition, and resuspension* (H. R. Pruppacher, R.G. Semonia, and W.G.N. Slinn, eds.), 71-78, Elsevier Science Pub. Co.
- Radke, L. F., J. H. Lyons, P. V. Hobbs, and J. E. Coakley, 1988: In situ measurements of "ship tracks" . *Preprints for 10-th Intern. Cloud Physics Conf.*, Bad Homburg, FRG, August 15-20, 1988. pp. 121-123, (vol. 1).
- Radke, L.F. and P.V.Hobbs, 1969: Measurement of cloud condensation nuclei, light scattering coefficient, Sodium containing particles, and Aitkin nuclei in the Olympic Mountains of Washington. *J. Atmos. Sci.* 26, 281-288.

- Radke L.F. and P.V. Hobbs, 1991: Humidity and particle fields around some small cumulus clouds. *J. Atmos. Sci.*, **48**, 1190-1193.
- Randall, D. A., T.N. Carlson, and Y. Mintz, 1984: *In aerosol and their climate effects* (H.E. Gerber and A. Deepak, eds), 123-132. A. Deepak Publishing, Hampton, Virginia.
- Ritchie, A.A., 1975: A variational optimizing analysis approach to continuous data assimilation. Ph.D dissertation, Univ. of Oklahoma, Norman, OK, 98 pp.
- Sasaki, Y.K., 1958: An objective analysis based on the variational method. *J. Meteor. Soc. Japan*, **36**, 77-88.
- Saxena, V.K., J.N. Burford, and J.L. Kassner, Jr, 1970: Operation of a thermal diffusion chamber for measurements on cloud condensation nuclei. *J. Atmos. Sci.* **27**, 73-80.
- Slingo, A. , 1989: A GCM parameterization for the shortwave radiative properties of water clouds. *J. Atmos. Sci.*, **46**, 1419-1427.
- and H.M. Schrecker, 1982: On the shortwave properties of stratiform water clouds., *Quart. J. R. Met. Soc.*, **108**, 407-426.
- Slinn, W.G.N. and J. M. Hales, 1971: A reevaluation of the role of thermophoresis as a mechanism of in- and below-cloud scavenging. *J. Atmos. Sci.*, **28**, 1465-1471.
- Smolarkiewicz, P. K., and W.W. Grabowski, 1990: The multi-dimensional positive definite advection transport algorithm: Nonoscillatory option. *J. Comput. Phys.*, **86**, 355-375.
- Stephens, J.J., 1970: Variational initialization with the balance equation. *J. Appl. Meteor.*, **9**, 732-739.
- Taylor, J. P. and A. McHaffe, 1994: Measurements of cloud susceptibility, *J. Atmos. Sci.*, **51**, 1298-1306.
- Tremback, C. J., J. Powell, W. R. Cotton, and R. A. Pielke, 1987: The forward-in-time upstream advection scheme: Extension to higher orders. *Mon. Wea. Rev.*, **115**, 540-555.
- Twomey, S., 1972: The effect of cloud scattering on the absorption of solar radiation by atmospheric dust. *J. Atmos. Sci.*, **29**, 1156-1159.
- Twomey, S., 1974: Pollution and the planetary albedo. *Atmos. Environ.* **8**, 1251-1256.
- Twomey, S., 1991: Aerosols, clouds and radiation. *Atmos. Environ.* **25A**, 2435-2442.

- Tzivion, S., G. Feingold and Z. Levin, 1987: An efficient numerical solution to the stochastic collection equation. *J. Atmos. Sci.*, **44**, 3139-3149.
- Wallace, J. M., and P. V. Hobbs, 1977: *Atmospheric Science, an introductory survey*. Academic Press, 467pp.
- Waggoner, A.P., and R.J. Charlson, 1976: Measurements of aerosol optical parameters. In *Fine particle, aerosol generation, measurements, sampling, and analysis*. Edited by B.Y.H. Liu, Academic Press, 837 pp.
- Warner, J., 1969: The microstructure of cumulus cloud: Part II. The effect on droplet size distribution of the cloud nucleus spectrum and updraft velocity. *J. Atmos. Sci.*, **26**, 1272-1282.
- Wyant, M. C., C.S. Bretherton, H.A. Rand, and D.E. Stevens, 1997: Numerical simulation and a conceptual model of the stratocumulus to trade cumulus transition. *J. Atmos. Sci.*, **54**, 168-192.
- Young, K.C., 1974: A numerical simulation of wintertime, orographic precipitation: Part I. Description of model microphysics and numerical techniques. *J. Atmos. Sci.*, **31**, 1735-1748.

## APPENDIX

# A

## Adjustment of negative values

As noted in Liu *et. al.* (1995), the VO method may produce some small negative values in cloud drop concentration which are normally associated with very sharp narrow spectra. We adjust these small negative values in the following way. Let us denote the summation of negative  $N_i$  as  $C^-$  and positive  $N_i$  as  $C^+$  ( $C = C^- + C^+$ ). After setting the negative  $N_i$  to be zero, the new  $N_i^{new}$  can be calculated as  $N_i^{new} = N_i(1 + \frac{C^-}{C^+})$ . By doing this, we still have  $\sum_{i=1}^K N_i^{new} = C$ , but LWC is no longer conserved. Our tests show that the LWC error is very small in most cases, exceptions are associated with very narrow spectra occupying only 2-3 bins. Fig. 8 shows the percentage of the negative value occurrence in the CIMMS LES model during the two dynamic time steps which produce 142,985 calls to the VO method

subroutine. The calls which produced negative values were counted whenever  $\left| \frac{C^-}{C} \right| > \delta$  or  $\left| \frac{Q^-}{Q} \right| > \delta$ . ( $Q^-$  and  $Q$  being the total negative LWC and total LWC, respectively). The percentage of the calls which produce negative values are plotted in Fig. A.1 as a function of  $\delta$ . Of the 142,985 calls, there were no cases with negative values for  $\delta=0.09$ , and only 9 cases for  $\delta=0.05$ . All the 9 cases show that the spectra were at the early stage of activation in which CCNs were just activated and have not grown large enough and the drops concentrated in the first two or three bins. As  $\delta$  decreases, the percentage of the negative values increases. Even for  $\delta=10^{-5}$  (0.001%), the occurrence of the negatives values is less than 1%. In fact, if the negative value is large, we use the KO method (which broadens the spectra) for one time step. At the next time step, the VO method is automatically selected, and the error again will be checked. If the error exceeds our criteria, the KO method will be used. This procedure can be repeated until all errors meet our criteria.

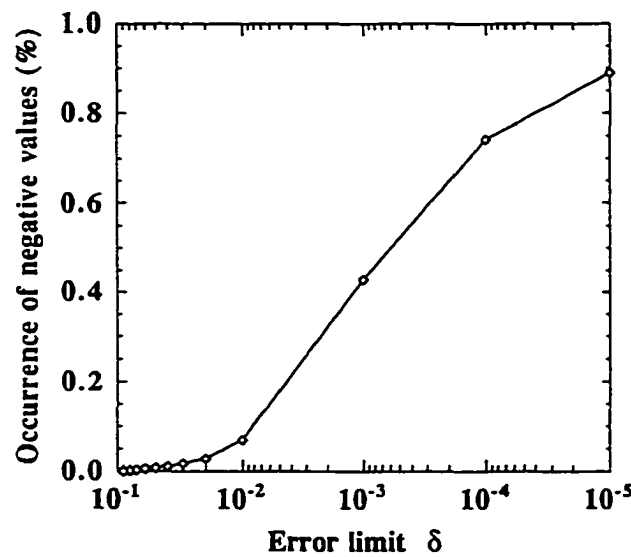


Figure A.1. Percentage occurrence of the negative values in CIMMS LES model as a function of the error limit.

## APPENDIX

# B

## Description of the decomposition procedure

This appendix describes how the mass distribution function  $f(x)$  is decomposed into 3 sub-spectra prior to condensation calculations (Figure 4).

a) Find the maximum (B) of the spectrum, and the smallest  $x_a$  (A) and the largest  $x_c$  (C) bins that have liquid water content exceeding the minimum threshold ( $10^{-3}$  g/m<sup>3</sup>).

b) Find the drop bins ( $x_k$  and  $x_l$ ) at which the differences between  $f(x)$  and their corresponding values on lines AB and BC is at their maximum.

c) Fit Gamma functions  $G^{(1)}$  ( $G^{(2)}$ ) that pass through the points  $x_{k+1/2}$  ( $x_{l-1/2}$ ) and have the same slopes as  $f(x)$  at these points. The Gamma function is defined here as a two-parameter function:

$$G(x) = c_1 x^2 \exp(-c_2 x)$$

where  $c_1$  and  $c_2$  are constants and can be calculated as,

$$c_2 = \frac{2}{x_{k+1/2}} - \frac{f'(x_{k+1/2})}{f(x_{k+1/2})}, \quad c_1 = \frac{f(x_{k+1/2})}{x_{k+1/2}^2} \exp(c_2 x_{k+1/2}) \quad \text{for } G^{(1)},$$

and 
$$c_2 = \frac{2}{x_{l-1/2}} - \frac{f'(x_{l-1/2})}{f(x_{l-1/2})}, \quad c_1 = \frac{f(x_{l-1/2})}{x_{l-1/2}^2} \exp(c_2 x_{l-1/2}) \quad \text{for } G^{(2)}.$$

(d) decompose the spectrum into three parts:

$$\text{Part 1.} \quad \begin{cases} \hat{N}_i^{(1)} = \max(0., \hat{N}_i^{(1)} - \Gamma_i^{(1)}) & x_i \leq x_k \\ \hat{N}_i^{(1)} = 0. & x_i > x_k \end{cases}$$

$$\text{Part 2.} \quad \begin{cases} \hat{N}_i^{(2)} = \min(\hat{N}_i, \Gamma_i^{(1)}) & x_i \leq x_k \\ \hat{N}_i^{(2)} = \hat{N}_i & x_k < x_i < x_l \\ \hat{N}_i^{(2)} = \min(\hat{N}_i, \Gamma_i^{(2)}) & x_i \geq x_l \end{cases}$$

$$\text{Part 3.} \quad \begin{cases} \hat{N}_i^{(3)} = 0. & x_i < x_l \\ \hat{N}_i^{(3)} = \max(0., \hat{N}_i - \Gamma_i^{(2)}) & x_i \geq x_l \end{cases}$$

where  $\hat{N}_i$  is the drop concentration in bin  $i$  and  $\Gamma_i$  ( $= G_i/m_i$ ) is the drop concentration for the fitted Gamma function.

e) Use the VO method for each part separately, then sum the outputs together.